Investigation of Bainitic Phase Transformation and Phase Evolution during Tempering of High Strength Medium Carbon Steels

by

Ehsan TOLOUEI

MANUSCRIPT-BASED THESIS PRESENTED TO ÉCOLE DE TECHNOLOGIE SUPÉRIEURE IN PARTIAL FULFILLEMENT OF THE REQUIREMENTS FOR THE DEGREE OF DOCTOR OF PHILOSOPHY
Ph.D.

MONTREAL, AUGUST 20,2026

ÉCOLE DE TECHNOLOGIE SUPÉRIEURE
UNIVERSITÉ DU QUÉBEC

BOARD OF EXAMINERS

THIS THESIS HAS BEEN EVALUATED

BY THE FOLLOWING BOARD OF EXAMINERS:

Mr. Mohammad Jahazi, Thesis Supervisor
Department of Mechanical Engineering at École de technologie supérieure

Mr. Carlos Garcia-Mateo, Thesis Co-supervisor
Department of Physical Metallurgy at National Center for Metallurgical Research

Mr. Conard Boton, Chair, Board of Examiners
Department of Construction Engineering at École de technologie supérieure

Mr. Vincent Demers, Member of the jury
Department of Mechanical Engineering at École de technologie supérieure

Mr. Ricardo Emilio Sierra Aristizabal, External Examiner
Materials Engineering Department at Antioquia University

Mr. Behzad Avishan, External Examiner
Department of Mechanical Engineering at Baskent University

THIS THESIS WAS PRENSENTED AND DEFENDED

IN THE PRESENCE OF A BOARD OF EXAMINERS AND PUBLIC

ON JULY 9,2026

AT ÉCOLE DE TECHNOLOGIE SUPÉRIEURE

ACKNOWLEDGMENT

I would like to express my heartfelt appreciation to my advisor, Prof. Mohammad Jahazi, whose insightful guidance, steady encouragement, and belief in my potential shaped my doctoral journey. His expertise, professionalism, and approachable nature created a supportive environment where I thrived both intellectually and personally. His mentorship not only influenced this research but also served as a model for my future path.

I am equally grateful to my co-supervisor, Prof. Carlos Garcia-Mateo, for his thoughtful feedback, constructive criticism, and consistent support. His input was instrumental in refining my experimental approach and deepening my understanding. I also thank my examination committee, Prof. Vincent Demers for their valuable feedback and suggestions during the DGA 1033 oral defense.

I gratefully acknowledge the Natural Sciences and Engineering Research Council (NSERC) of Canada for funding this work through the Collaborative Research and Development Grant (CRDPJ 536444). This support was pivotal to advancing the study.

My thanks to Sorel, the industry partner, for their collaboration and assistance in the experimental phase. Their provision of materials and technical input was vital, and I particularly thank Mr. Jean-Benoit Morin for his guidance and contributions.

I would also like to acknowledge the CM2P group at ÉTS. Their collaboration, discussions, and friendship created a motivating research environment. Special thanks to Dr. Mohammad Saadati for his generous training on SEM, LEXT, EBSD, and analysis, and to Dr. Alireza Khodabandeh for his valuable help with dilatometry, a significant part of this research. I also thank Mr. Radu Romanica for his support with laboratory instrumentation.

On a personal note, I am deeply grateful to my parents and my sibling for their unconditional support and encouragement throughout my academic journey. Their strength and sacrifices have been my foundation.

Finally, a very special thank you to my wife, whose patience, understanding, and unwavering support sustained me through this demanding journey. Her companionship gave me the strength to persevere, and I am truly blessed to have had her by my side.

Étude de la transformation de la phase bainitique et de l'évolution des phases lors du revenu ultérieur d'aciers à moyenne teneur en carbone à haute résistance

Ehsan TOLOUEI

RÉSUMÉ

Dans cette étude, la transformation de phase bainitique dans un acier faiblement allié à teneur moyenne en carbone a été étudiée, suivie d'un traitement de revenu. L'accent a été mis sur le procédé de fabrication de gros blocs d'acier, tant du point de vue industriel que scientifique.

La transformation bainitique a été examinée à la fois en conditions de refroidissement continu et d'austempering. Pour la fabrication de petits blocs d'acier, le refroidissement continu suivi d'un double revenu a été remplacé par le procédé conventionnel d'austempérage suivi d'un seul cycle de revenu. Les résultats expérimentaux obtenus à la fois à l'échelle du laboratoire et lors d'essais industriels ont démontré le succès de cette nouvelle approche. L'austempering a été étudié dans une plage de températures allant de 380 à 450 °C, et les microstructures obtenues ont été caractérisées en termes de fractions volumiques des phases, de caractéristiques des phases individuelles, ainsi que de dureté globale et locale.

Dans le cas de la transformation bainitique sous refroidissement continu, l'effet de la taille des grains d'austénite initiale lors d'un refroidissement lent a été étudié. Dans ces conditions, une transformation en plusieurs étapes a été observée. Lors de la première étape, une bainite à la fois granulaire et en plaques s'est formée, suivie d'une seconde étape impliquant la formation de martensite accompagnée d'un auto-revenu ainsi que du revenu de la bainite. Les différences significatives de fraction volumique des phases ont été attribuées à l'austénite retenue, dont la fraction a augmenté de 10 % à 24,6 % lorsque la taille des grains d'austénite initiale passait de 100 à 300 μm.

L’influence de l’hétérogénéité thermique au cours du traitement de revenu a été étudiée dans des blocs d’acier de grande épaisseur. Les variations du temps nécessaire pour atteindre la température de revenu cible ont engendré des différences significatives tant au niveau de la microstructure que de la dureté. Par ailleurs, les résultats mettent en évidence une influence marquée du temps de revenu sur la diminution de la fraction de joints de grains à faible désorientation, ce qui suggère que ce mécanisme constitue un processus prépondérant lors du revenu dans cette classe d’aciers. De plus, les carbures ont montré une résistance notable au grossissement, même après 14 heures de revenu.

Les résultats de cette étude mettent en évidence l’influence significative de la température d’austempérage sur les transformations de phase bainitique, ainsi que l’effet de la taille des grains d’austénite initiale sur la transformation de phase lors du refroidissement continu. De plus, ils soulignent l’impact de l’hétérogénéité thermique lors du revenu de sections épaisses sur l’évolution de la microstructure.

Mots-clés: bainite granulaire, bainite en plaques, transformation de phase en plusieurs étapes, austénite retenue, joints à faible désorientation, constituant martensite–austénite

INVESTIGATION OF BAINITIC PHASE TRANSFORMATION AND PHASE EVOLUTION DURING TEMPERING OF HIGH STRENGTH MEDIUM CARBON STEELS

Ehsan TOLOUEI

ABSTRACT

In this study, the bainitic phase transformation in a medium-carbon low-alloy steel was investigated, followed by tempering. The focus was on the manufacturing process of large steel blocks from both industrial and scientific perspectives.

The bainitic phase transformation was investigated under both continuous cooling and austempering conditions. For the manufacturing of small steel blocks, continuous cooling followed by double tempering was replaced with the conventional austempering process followed by a single tempering cycle. Experimental results from both laboratory-scale studies and industrial trials demonstrated the success of this new approach. Austempering at temperatures ranging from 380 to 450 °C was investigated, and the resulting microstructures were characterized in terms of phase volume fractions, individual phase characteristics, and both overall and local hardness.

In the continuous cooling bainitic transformation, the effect of prior austenite grain size during slow cooling was investigated. Under these conditions, a multi-stage transformation was observed. In the first stage, both granular and plate-like bainite formed, followed by a second stage involving martensite formation accompanied by auto-tempering and the tempering of bainite. The significant differences in phase volume fraction were attributed to retained austenite, which increased from 10% to 24.6% as the prior austenite grain size increased from 101 to 304 μm.

The effect of temperature non-uniformity during the tempering process was investigated in large steel blocks. Variations in the time required to reach the target tempering temperature resulted in significant differences in both microstructure and hardness. Furthermore, the results indicate a pronounced influence of tempering time on the reduction of low-angle grain boundaries, suggesting that this mechanism plays a primary role during tempering in this class

of steels. Additionally, the carbides exhibited notable resistance to coarsening, even after 14 hours of tempering.

The findings of this study highlight the significant influence of austempering temperature on bainitic phase transformations, as well as the effect of prior austenite grain size on the phase transformation during continuous cooling. Additionally, the results underscore the impact of temperature non-uniformity during the tempering of thick sections on the evolution of microstructure.

Keywords: Granular bainite, Plate-like bainite, Multi-stage phase transformation, Retained austenite, Low-angle boundaries, Martensite-austenite constituent

Table of contents

Page

LIST OF TABLES

Page

LIST OF FIGURES

Page

LIST OF ABREVIATIONS

Fe	Iron
C	Carbon
Si	Silicon
V	Vanadium
Cr	Chromium
Mn	Manganese
Ni	Nickel
Mo	Molybdenum
BCT	Body-centered tetragonal
AISI	American Iron and Steel Institute
HB	Brinell Hardness
SEM	Scanning Electron Microscopy
M-A	Martensite – Austenite
BCC	Body Centered Cubic
FCC	Face Centered Cubic
PAGS	Prior austenite grain size
CCT	Continuous Cooling Transformation
TTT	Time-Temperature Transformation
RA	Retained Austenite
FE-EOMA	Field Emission – Electron Probe Micro Analysis
GB	Granular Bainite
UB	Upper Bainite
DUB	Degenerate Upper Bainite
LB	Lower Bainite
DLB	Degenerate Lower Bainite
PB	Plate-like Bainite
EBSD	Electron Backscatter Diffraction
SiC	Silicon Carbide
XRD	X-Ray Diffraction
EDS	Energy-Dispersive Spectroscopy
S	Second
HV	Vickers Hardness
DIN	Deutsches Institut für Normung
SiC	Silicon Carbide
ASTM	American Society for Testing and Materials
FEM	Finite Element Method
RCL	Relative Change in Length
QT	Quenching and Tempering
AC	Aggregated Carbide zone

EC	Elongated Carbide
HAGB	High Angle Grain Boundary
LAGB	Low Angle Grain Boundary
DRCL	Derivative Relative Change in Length

LIST OF SYMBOLS

α	$-$	Alpha
γ	$-$	Gamma
λ	$\mathring{A}$	Wave Length
θ	$^{\circ}$	Angle
ΔG	$KJ/mole$	Gibbs Free energy
V_{AM}	%	Athermal martensite volume fraction
V_{BF}	%	Bainitic ferrite volume fraction
V_{RA}	%	Retained austenite volume fraction
V_{FM}	%	Fresh martensite volume fraction
$D\gamma$	µm	Austenite grain diameter
Dc	µm	Critical grain diameter
HV	Kgf/mm^2	Vickers Hardness
hm	Nm	Maximum displacement
hp	Nm	Final indentation depth
S	N/nm	Contact stiffness
hr	nm	Indentation depth
A	nm^2	Contact area
ε	-	Constant
ρ	kg/m^3	Density
C_p	$J/kg \cdot K$	Specific heat capacity
T	K	Temperature
t	s	Time
K	$W/m \cdot K$	Thermal conductivity
$Ys\gamma$	MPa	Yield strength of austenite
Ms	°C	Martensite start temperature
Mf	°C	Martensite finish temperature
Bs	°C	Bainite start temperature
Bf	°C	Bainite finish temperature
θ	-	Cementite
$C\gamma$	wt%	Austenite carbon content
$f\gamma$	%	Austenite volume fraction
Ac1	°C	Austenite start formation
Ac3	°C	Austenite finish formation
$\Delta Lmax$	µm	Maximum length change
L_0	µm	Length of sample before phase transformation
L_{max}	µm	Length of sample after phase transformation

INTRODUCTION

In recent years, a major issue in industrial heat treatment has arisen from challenges in the manufacturing process of large steel blocks, particularly those used as plastic injection molds for automotive parts such as bumpers and dashboards. These molds are commonly produced from medium-carbon, low-alloy steels made through ingot casting, open-die forging, water bath cooling, and double tempering. The considerable thickness of such blocks (often above 1000 mm) creates steep temperature gradients between the surface and the core, resulting in significant microstructural variations such as prior austenite grain size, phase distribution, phase morphology, etc. For instance, during quenching, the outer regions often transform fully to martensite, while bainitic structures form in the interior. Additionally, due to the non-uniform strain distribution during the forging process, large grain size variations occur from the surface to the center of the block. Tempering introduces further gradients since the surface heats more rapidly than the center, causing different regions to experience distinct thermal cycles and evolve dissimilarly. These uneven transformations lead to heterogeneous microstructures which, in turn, influence final mechanical properties. Furthermore, features such as coarse carbides or retained austenite can degrade surface finish and polishability, ultimately reducing the quality of molded plastic components; therefore, the sources of such defects should be identified.

From an economic perspective, the conventional heat treatment of small mold steel is inefficient, as large blocks are quenched and double tempered before being sectioned into smaller sizes. This results in prolonged processing times, excessive energy consumption, and increased production costs due to double tempering treatment. As an alternative, austempering can be considered a new manufacturing approach for small mold components, followed by single tempering. By enabling controlled phase transformation and reducing processing steps, austempering can improve efficiency, shorten processing time, lower costs, and, for the first time, enhance overall process sustainability in medium-carbon, low-alloy steel. Considering the aforementioned challenges in the heat treatment process of this type of steels, three sub-objectives were defined in order to address existing gaps in the literature.

The first sub-objective is to investigate how variations in prior austenite grain size influence bainitic phase transformation at both the surface and core of large steel blocks. In this section, for the first time, the phase evolution during slow cooling in thick mold steel with very large prior austenite grain size is examined and the observed multi-stage phase transformation is interpreted using high-resolution dilatometry.

The second sub-objective aims to evaluate the application of an austempering heat treatment cycle to small size mold steel blocks. In current industrial practice, both small and large molds undergo continuous cooling followed by double tempering. However, most studies on austempering have focused on high-silicon steels to obtain bainitic microstructures, this work evaluates its applicability to mold steels under industrially relevant conditions to determine its effectiveness relative to the conventional quench-and-double-temper treatment. To this end, the fundamental mechanisms governing bainitic transformation in these steels need to be studied.

In the third sub-objective, the effects of non-uniformity in the tempering process are investigated. Due to the long tempering time required for large mold steels (often exceeding 30 hours), the tempering behavior of these steels differs significantly from that reported in most laboratory-scale studies. Specifically, the tempering time required to reach the target tempering temperature is examined at both the surface and the center of the steel block. Additionally, carbide evolution and retained austenite decomposition are analyzed in this section as the final step of the industrial heat treatment process.

Achieving the above three sub-objectives contributes to a better understanding of both the scientific and industrial aspects of the heat treatment process of large mold steels. Accordingly, this study is structured into six chapters, as outlined below:

CHAPTER 1 presents a comprehensive literature review on medium-carbon low-alloy steels, their heat treatment processes, the industrial challenges involved, and the metallurgical aspects of phase transformations. The chapter addresses the challenges encountered at various stages of heat treatment, with particular emphasis on the influence of block thickness on the microstructural evolution at each stage. The chapter concludes by outlining critical gaps in

current knowledge, which serve as the basis for defining and justifying the study's main and specific objectives.

CHAPTER 2 presents the experimental methodology, describing the materials and specimen preparation, including characterization of the industrial block, as well as the techniques used to investigate phase transformations, microstructural features, and mechanical properties. CHAPTER 3 examines how variations in prior austenite grain sizes affect bainitic phase transformation from a scientific perspective, with particular emphasis on the differences between the surface and core regions of large steel blocks. In addition, from an industrial perspective, this chapter evaluates the impact of these variations on the retained austenite volume fraction and the hardness of the material. Complementary tests were designed and carried out to systematically characterize the mechanisms and results of simultaneous phase transformations occurring during slow continuous cooling, with particular emphasis on bainite morphologies, martensitic transformation, and the associated auto-tempering process. The results from this chapter were published in the Journal of Materials Research and Technology.

CHAPTER 4 presents the experimental investigation of austempering on isothermal bainitic phase transformation in mold steels. The resulting microstructures were analyzed, and hardness at both micro- and nanoscale were examined and compared. The mechanisms determining the hardness of different phases, such as the carbon content of martensite and the block thickness of bainite, were investigated. The findings from this chapter were published in the Journal of Materials Chemistry and Physics in July 2025.

CHAPTER 5 presents the experimental study of bainitic tempering over short and long time, reflecting the varying times required to reach the tempering target in large steel blocks. The time-dependent effects of the tempering were systematically analyzed in terms of carbide evolution, hardness changes, retained austenite decomposition, and softening mechanisms. The findings from this chapter were published in the Journal of Materials Science and Technology in October 2025.

CHAPTER 6 presents complementary experimental work based on the results of Chapter 4. In this chapter, the effect of a slow cooling rate after isothermal bainitic phase transformation was

investigated in order to better replicate industrial-scale condition. In addition, the microstructural evolution and transformation kinetics are examined, and the results will report in a conference paper.

In conclusion, this study offers a detailed investigation of the influence of very large prior austenite grain sizes on bainitic phase transformation in large steel blocks, using advanced experimental techniques. The findings reveal how grain size variations affect the final microstructure from surface to core. Additionally, an alternative industrial approach was evaluated by replacing the conventional continuous cooling with an austempering process in smaller steel blocks. The influence of the isothermal bainitic transformation temperature on the resulting microstructure and mechanical properties was systematically investigated. Finally, the primary mechanisms responsible for softening during extended tempering cycles in mold steels were examined.

CHAPTER 1

LITERATURE REVIEW

1.1 Steel

Steel remains a fundamental material in modern society, with its significance expected to persist well into the foreseeable future. Over the past twenty years, the global steel sector has experienced profound transformations, a trend projected to continue. Asian nations, particularly China, have emerged as the leading producers of steel, contributing to a worldwide overcapacity. Conversely, steel industries in developed countries have invested heavily in process technological upgrading, advancing product innovation, and maintaining sustainability and competitiveness on the global stage (Li & Davis, 2019).

Steel is broadly defined as an alloy primarily composed of iron (Fe) and carbon (C), often supplemented with additional elements such as silicon (Si), vanadium (V), chromium (Cr), manganese (Mn), nickel (Ni), molybdenum (Mo), etc. These alloying elements significantly influence its microstructure, mechanical and physical properties, as well as corrosion resistance. Steel is one of the most important structural materials worldwide, widely used in both daily life and industry due to its easy fabrication, versatility, availability, and low cost (Islam and Rashed 2019). Beyond its use in household tools, steel is extensively employed in structural engineering, transport, industrial tools, and the manufacturing of a wide array of goods from kitchen utensils to components in aerospace industry.

Although steel can be classified based on various parameters, one of the most common methods categorizes it into four main groups: carbon steel, alloy steel, stainless steel, and tool steel. Among the various types of steel, carbon steels constitute the majority of global production, primarily due to their cost-effectiveness and sufficient mechanical strength for large-scale construction projects.

1.2 Allotropes of pure Iron

A major reason for the overwhelming dominance of steels is the vast range of microstructures, allotropes and properties that can be achieved through solid-state transformations and processing. Because of this, it is helpful to study steels by first examining the behaviour of pure iron, then iron–carbon alloys, and finally the additional complexities introduced when other alloying elements are added (Bhadeshia & Honeycombe, 2017). Figure 1-1 presents the allotropic forms of pure iron as a function of temperature and pressure, each characterized by distinct crystallographic structures and physical properties. Under atmospheric pressure, the stable phase at room temperature is the body-centered cubic (BCC) structure, known as ferrite (α). Upon heating, pure iron transforms into the face-centered cubic (FCC) phase, austenite (γ), above approximately 912 °C, and reverts to a BCC structure (δ-ferrite) close to the melting point (Bhadeshia & Honeycombe, 2017). The stability ranges of these allotropes can shift when alloying elements are added, leading to corresponding changes in phase-transformation behavior and mechanical response. These temperature-dependent solid-state transformations form the basis for microstructural development in steels, as discussed in the next section.

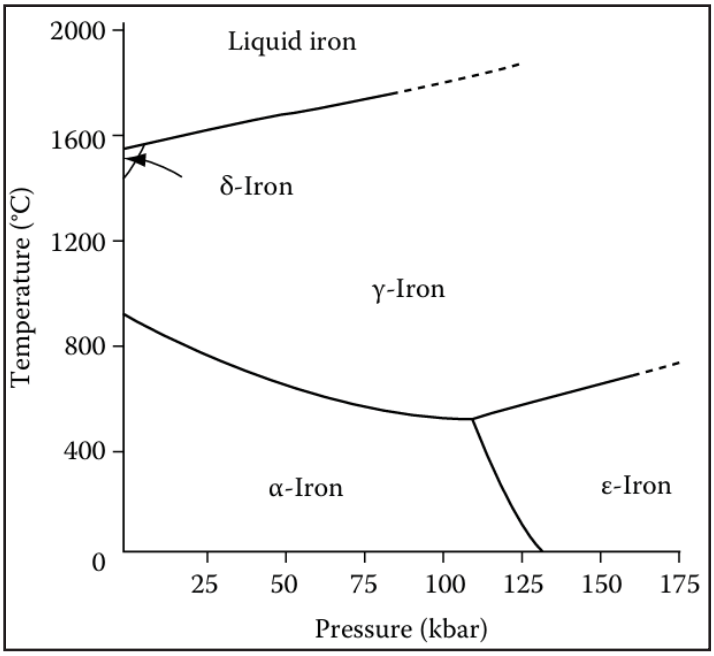

Figure 1-1 Different allotropes of iron exist under various temperature and pressure conditions

Taken from Porter & Easterling (2009, p. 8)

1.3 Phase Transformation in Steel

Steel is a ferrous alloy composed mainly of iron with carbon (C) as the principal interstitial solute. It may also contain substitutional alloying elements such as manganese (Mn), chromium (Cr), nickel (Ni), silicon (Si) and molybdenum (Mo). The microstructure of steel can be tailored through controlled phase transformations achieved by precise heating and cooling within specific temperature ranges where different solid phases are stable. The iron–carbon equilibrium phase diagram (Figure 1-2) serves as the fundamental reference for designing heat treatments, indicating the stability domains of each phase as a function of temperature and carbon content. However, in industrial practice, transformations generally occur under non-equilibrium conditions.

The remarkable microstructural variability of steels arises from diverse transformation mechanisms that govern the decomposition of austenite. These transformations proceed either via diffusion-controlled reconstruction or by diffusionless, shear-dominated lattice rearrangement (Bhadeshia & Honeycombe, 2017). In this work, attention is restricted to two

displacive products of austenite, bainite and martensite, whose morphologies, transformation kinetics, and resulting mechanical behavior are examined in the following sections.

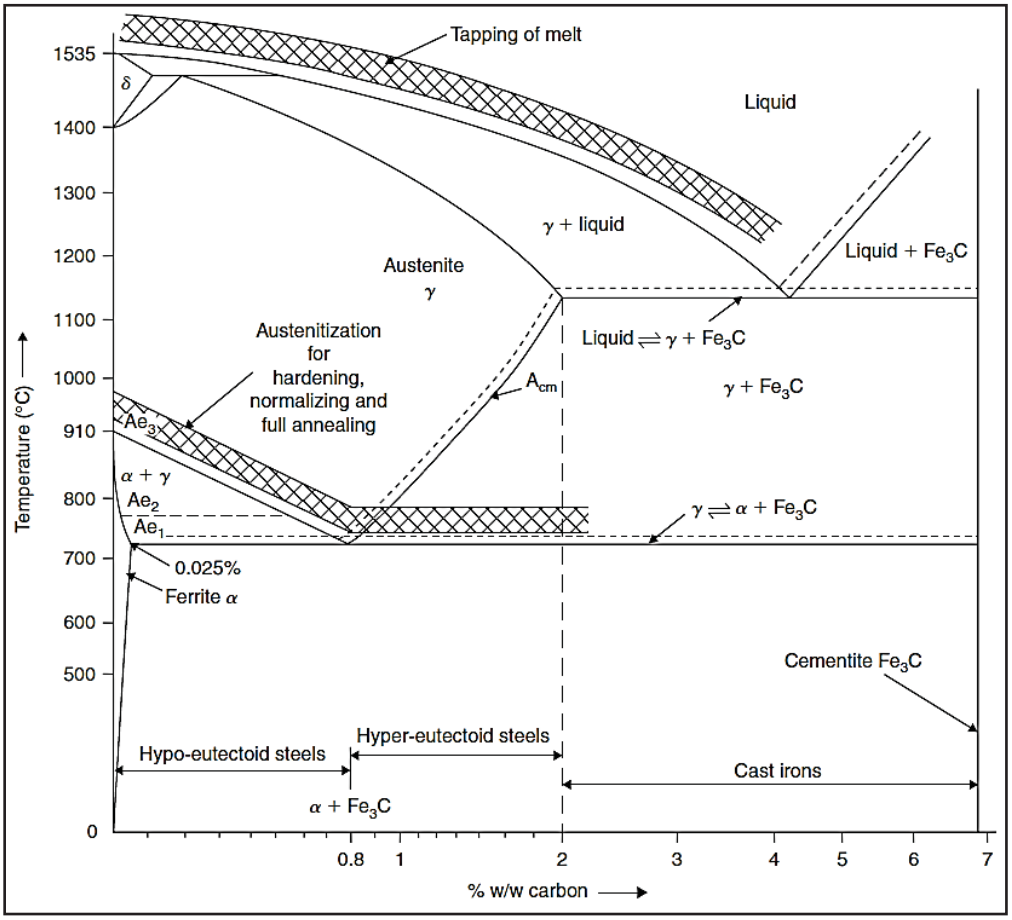

Figure 1-2 Fe-C equilibrium phase diagram
Taken from Smallman et al. (2011, p. 61)

1.3.1 Martensitic Phase Transformation

The martensitic transformation in steels is one of the earliest recognized and most extensively studied examples of a solid-state phase transformation (Pereloma & Edmonds, 2012). Martensite forms when austenite is rapidly cooled to room temperature, causing a diffusionless, shear-dominated lattice rearrangement. During quenching, the carbon atoms

originally dissolved in austenite become trapped within the distorted lattice of martensite, producing a body-centered tetragonal (BCT) structure. This distortion arises from supersaturation of carbon in the interstitial sites of the original FCC lattice, leading to pronounced internal stresses and high hardness. As illustrated in Figure 1-3, the transformation proceeds through a coordinated deformation of the austenitic lattice rather than long-range atomic diffusion. The phase interface advances more rapidly than carbon atoms can diffuse, defining the displacive nature of the martensitic reaction (Bhadeshia & Honeycombe, 2017).

General characteristics of martensite include the fact that the reaction in steels is typically described as athermal; that is, the fraction transformed depends on the undercooling below the martensite start temperature (Ms). From a mechanical properties perspective, the great hardness of martensite and the consequent low toughness at carbon contents above 0.25% is primarily due to carbon, rather than to other possible alloying elements dissolved in the austenite (Verdeja González et al., 2023).

During the manufacturing of large steel blocks, quenching in a water tank induces continuous cooling, generating steep thermal gradients from the surface inward. Owing to the high surface cooling rate, a martensitic transformation typically occurs within several centimeters of the outer layer, while the interior cools more slowly and may transform into mixed microstructures such as bainite. It should be noted that during subsequent manufacturing processes, such as tempering and final machining, most of the martensitic layer will be removed. Therefore, the primary microstructure of the large block is bainite.

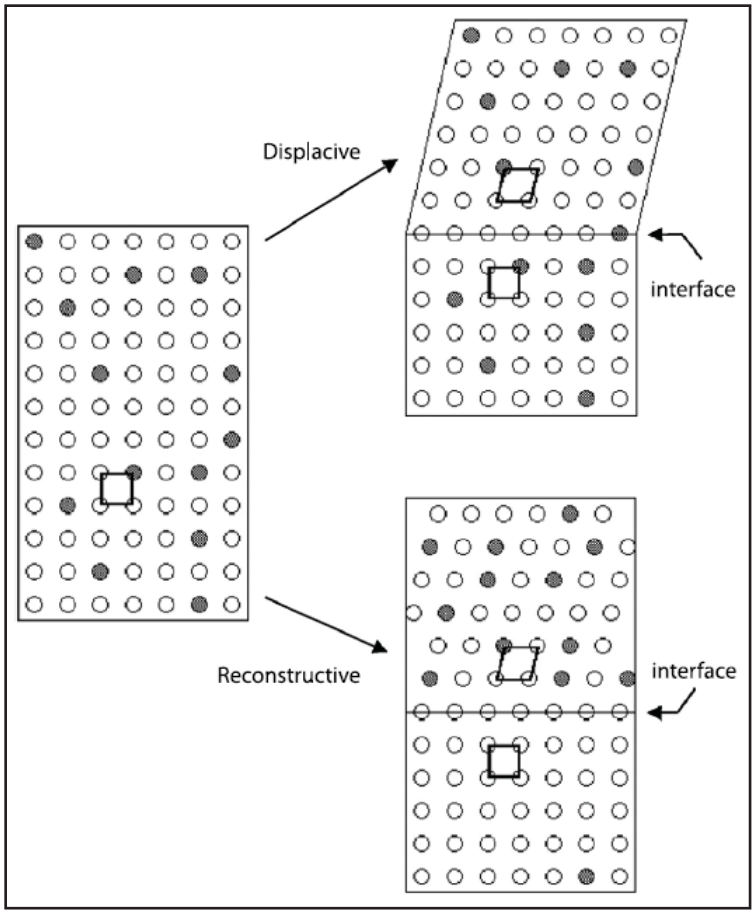

Figure 1-3 Schematic illustration of the transformation mechanisms: displacive and reconstructive
Taken from Bhadeshia and Honeycombe (2017, p. 9)

The Ms temperature is a key characteristic of the martensitic phase transformation and can be influenced by various parameters such as austenite grain size, cooling rate, and chemical composition. Based on the chemical composition, Liu et al. (Liu et al., 2001) demonstrated that while all alloying elements can affect the Ms temperature during the phase transformation, the most significant changes are associated with carbon, as illustrated in Figure 1-4.

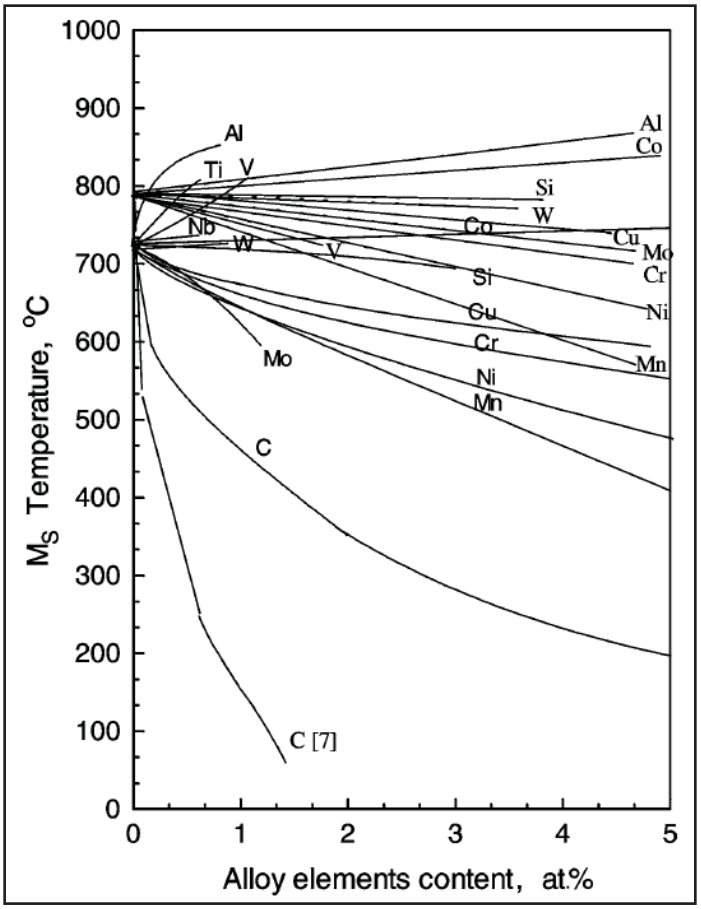

Figure 1-4 The influence of various alloying elements on the Ms temperature of steel
Taken from Liu et al. (2001, p. 558)

As a second controlling parameter, the influence of prior austenite grain size (PAGS) on the Ms has been extensively investigated (Hanamura et al., 2013; van Bohemen & Morsdorf, 2017). Most studies report that increasing PAGS leads to a higher Ms temperature. Two main mechanisms have been proposed to rationalize this behavior:

First, according to the Hall–Petch relationship (Hirth, 1972), finer austenite grains possess a higher grain-boundary density, which enhances strength and inhibits the lattice shearing required for the displacive martensitic transformation. As a result, the transformation is delayed, and Ms decreases.

Second, the geometrical model of Fisher et al. (Fisher, 1949) postulates that the initial martensite fraction formed at the onset of transformation scales with the cube of the austenite grain size. Consequently, larger grains allow the detectable transformation fraction to be reached at a smaller degree of undercooling, producing a higher apparent Ms temperature.

Van Bohemen and Morsdorf (van Bohemen & Morsdorf, 2017) further demonstrated that two factors control this relationship: (i) Hall–Petch hardening (WHP), dominant for coarse grains $D\gamma > Dc$, where $D\gamma$ is prior austenite grain size and Dc is the critical austenite grain size; and (ii) the martensite aspect ratio effect (WC), significant when the grain diameter $D\gamma < Dc$. In the latter case, the increase in aspect ratio raises the stored elastic energy within the transforming region, requiring a higher driving force and thus lowering Ms. These combined effects explain why the dependence of Ms on grain size changes above and below the critical grain size Dc, as illustrated in Figure 1-5.

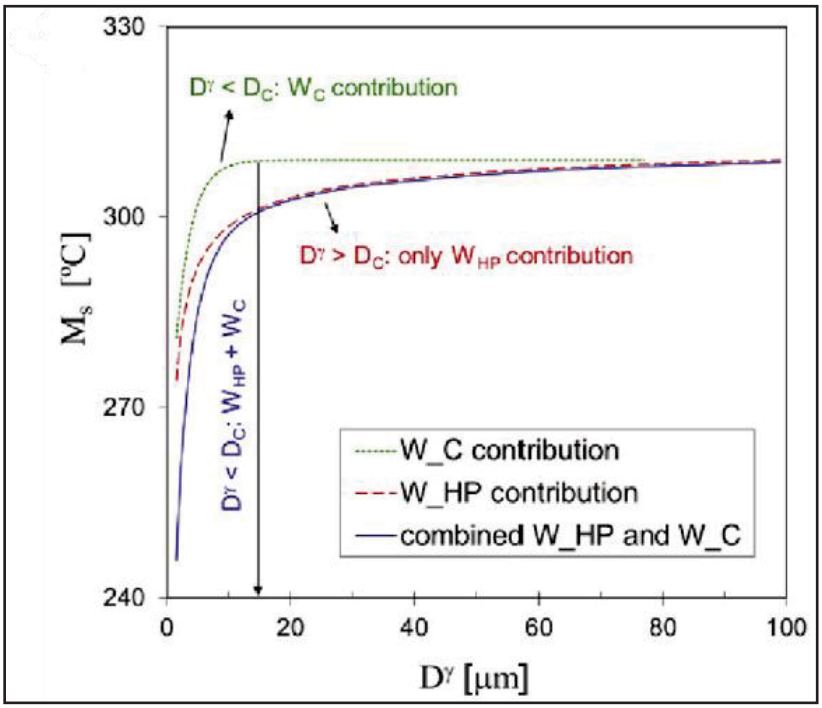

Figure 1-5 The corresponding impact of austenite grain size variation on the M_s temperature Taken from Bohemen and Morsdorf (2017, p. 406)

The effect of cooling rate on the Ms temperature has shown inconsistent results in the literature, being reported as dependent (Souza et al., 2020) and independent (Zhao & Notis, 1995). However, several studies in the literature have indicated that, for medium-carbon low-alloy steels, the Ms temperature remains largely unaffected by the cooling rate. For example, Zhao et al., (Zhao & Notis, 1995) using continuous cooling transformation (CCT) diagrams of a medium-carbon low-alloy steel, showed that the cooling rate has no significant effect on variations in the Ms temperature (Figure 1-6). In addition, Liu et al. (Liu J. H. et al., 2021) (Liu J. H. et al., 2021) reported Ms temperatures in the range of 280–290 °C for cooling rates between 0.11 and 2.27 °C s^{-1} below 300 °C, as shown in Figure 1-7 (Zhao & Notis, 1995). Their results show that, even when the same cooling rate is applied down to 300 °C, variations in the cooling rate to room temperature can lead to differences of maximum 10 °C in the Ms temperature.

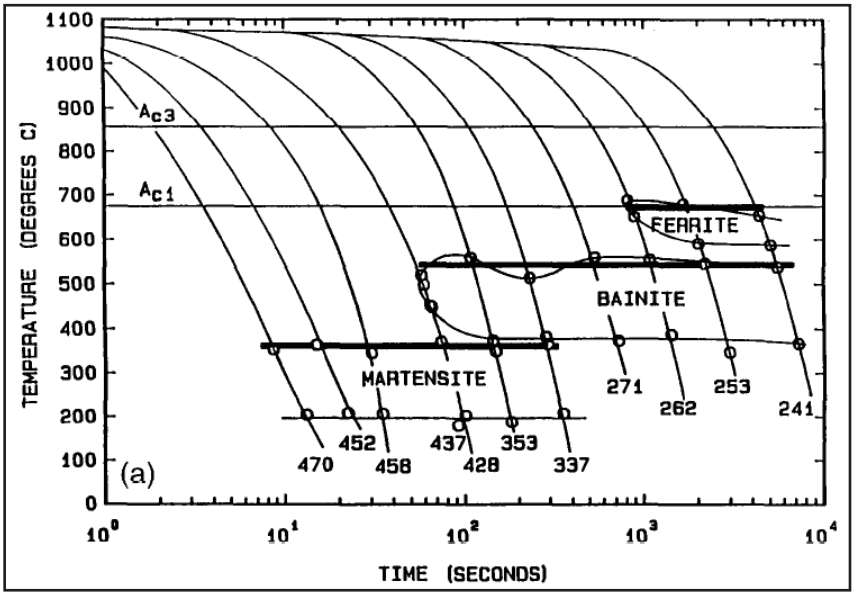

Figure 1-6 The CCT diagram of 0.24C, 1.67Mn, 0.39Si, 0.14Ni, 0.22Mo, 0.11V steel, showing Ms independent of the cooling rate (2.5 – 45 °C/s)

Taken from Zhao and Notis (1995, p. 138)

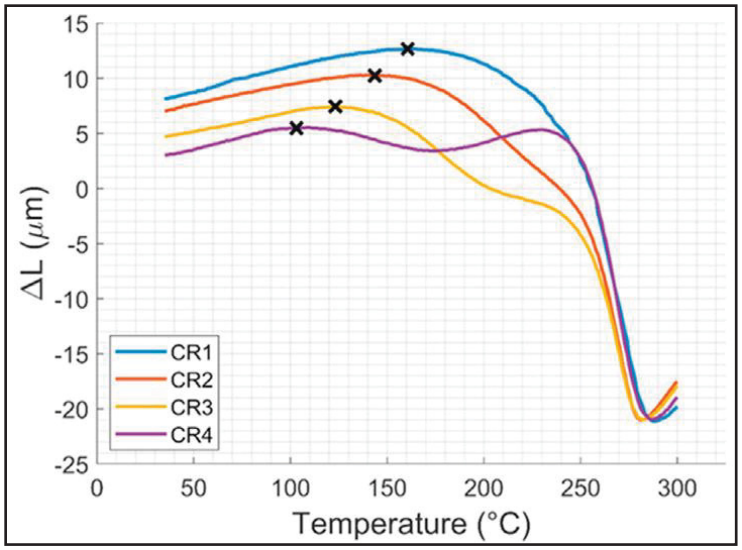

Figure 1-7 The dilatation curves of martensitic transformation for different cooling rates below 300 °C

Taken from Liu et al. (2021, p. 236)

The martensite finish temperature (Mf) lacks a precise thermodynamic definition, as the martensitic transformation proceeds progressively with increasing undercooling and rarely attains full completion. This incomplete transformation is attributed to the stabilization of retained austenite, a phenomenon whereby the remaining austenite becomes increasingly resistant to further transformation upon cooling (Souza et al., 2020). The detailed mechanisms governing this stabilization are discussed in section 1.3.2.2.

Despite its ambiguous definition, the evolution of Mf generally parallels that of the Ms. When Ms is unaffected by the cooling rate or prior austenite grain size, Mf likewise remains relatively constant (Figure 1-6). Conversely, if Ms varies with these parameters, Mf also shifts accordingly, particularly under conditions involving multi-stage martensitic transformations (Figure 1-7) (Hanamura et al., 2013; Liu J. H. et al., 2021).

1.3.1.1 Martensite Auto-tempering

In certain high-strength steels, another phenomenon that commonly occurs during quenching and martensitic phase transformation is auto-tempering. In this process, the first-formed

martensite, generated near the martensite Ms, is tempered during the subsequent stages of quenching or cooling (Bhadeshia & Honeycombe, 2017). As illustrated in Figure 1-8, this leads to the precipitation of fine carbide particles, typically in the form of rods or small plates which is related to auto-tempering. Autotempering is the spontaneous tempering of freshly formed martensite when the Ms is sufficiently high that carbon can diffuse during or immediately after transformation. Consequently, auto-tempering is more likely to occur in steels with a relatively high Ms temperature (i.e., steels with low-carbon content).

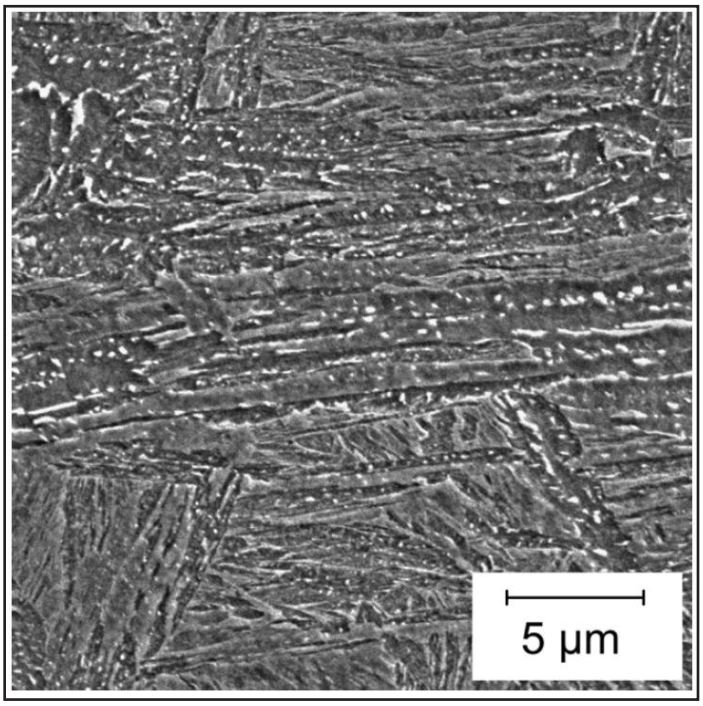

Figure 1-8 A steel containing 0.17 wt% carbon exhibits auto-tempered martensite formed below the Ms temperature

Taken from Bhadeshia and Honeycomb (2017, p. 239)

1.3.2 Bainitic Phase Transformation

Bainite typically forms at temperatures between those of reconstructive pearlite and displacive martensite, although some overlap can occur. It exhibits characteristic features of both pearlite

and martensite transformations. Consequently, the mechanism of bainite transformation has been a subject of intense debate since its discovery around 80 years ago (Pereloma & Edmonds, 2012). In the simplest terms, bainite can be defined as an aggregate of ferrite and carbide.

1.3.2.1 Bainitic Phase Transformation

The bainitic transformation proceeds via two distinct processes: continuous cooling transformation (CCT) and isothermal transformation (TTT). In CCT, the temperature decreases continuously throughout the transformation, whereas in TTT (austempering), the austenite is held at a constant temperature within the bainite range until completion.

In industrial production of large steel blocks, water quenching after furnace austenitization generates pronounced thermal gradients due to block thickness. The surface experiences rapid cooling sufficient for martensite formation within several centimeters of the outer layer, whereas the core cools more gradually, favoring bainite development throughout the bulk. In such cases, CCT diagrams can be used to predict the resulting phases and hardness distribution of the product. Figure 1-9 shows the CCT diagram of the steel investigated in this study.

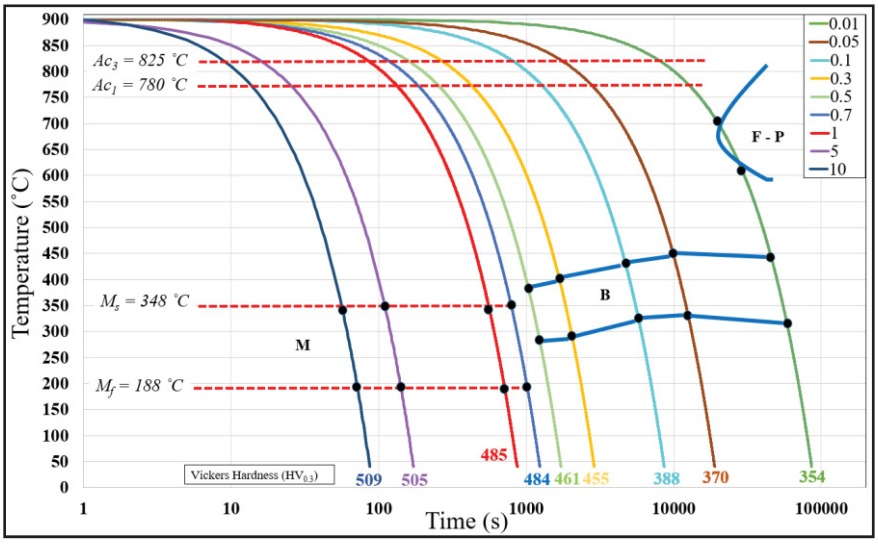

Figure 1-9 CCT diagram of the steel investigated in this study

In the case of isothermal bainitic phase transformation, after austenitization the steel block is immersed in a salt bath maintained at a temperature within the bainitic transformation range. The samples are held for a predetermined time to complete the transformation before cooling to room temperature. Figure 1-10 shows a typical TTT diagram for steel, with the cooling process indicated by red lines.

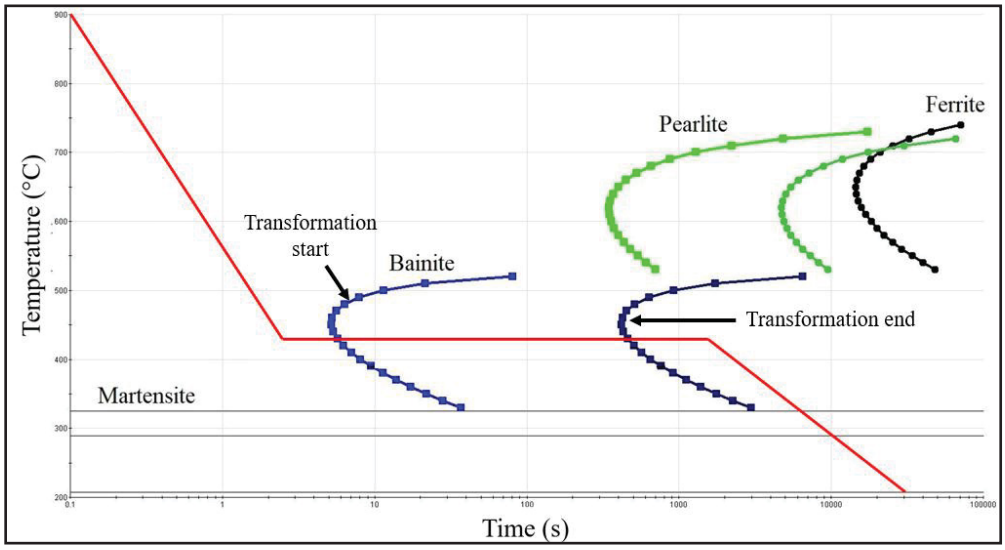

Figure 1-10 Typical TTT diagram of a 0.26% C, low-alloy steel calculated by JMatPro

1.3.2.2 Mechanism of bainitic Phase Transformation

Bhadeshia (H. Bhadeshia, 2001) described the bainitic transformation mechanism, in which bainitic ferrite nucleates preferentially at austenite grain boundaries and subsequently grows in clusters of laths or plates. Adjacent units develop autocatalytically via sympathetic nucleation on pre-existing ferritic plates or grain boundaries, as schematically illustrated in Figure 1-11.

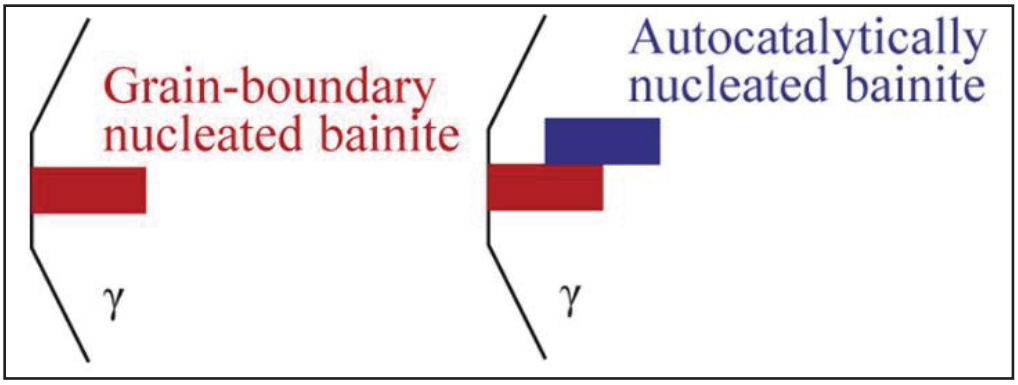

Figure 1-11 Different types of sub-unit nucleation during bainitic phase transformation

Taken from Ravi et al. (2016, p. 1)

These clusters, referred to as sheaves, exhibit a macroscopic wedge-shaped morphology with the thicker end originating at the grain boundary. As shown in Figure 1-12, each sheaf is composed of finer sub-units or platelets, typically less than 1 μm thick and around 10 μm long, which share nearly identical crystallographic orientations and are separated by small-angle boundaries.

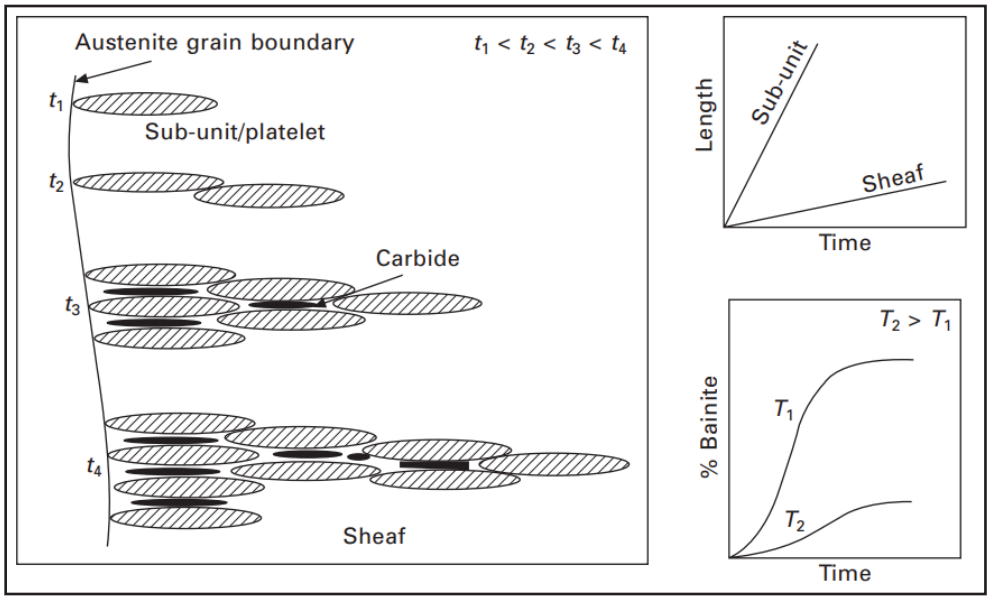

Figure 1-12 Schematic representation of a bainitic microstructure, highlighting its characteristic features

Taken from Bhadeshia (2001, p. 129)

The bainitic transformation is commonly described as occurring under paraequilibrium and diffusionless conditions (Bhadeshia & Honeycombe, 2017). A diffusionless phase transformation is one that occurs through a coordinated, shear-dominated movement of atoms over distances smaller than an interatomic spacing, without long-range atomic diffusion during the transformation. The crystal structure changes by a lattice distortion, and the interface advances rapidly compared to diffusion-controlled transformations.

Under this condition, carbon can redistribute, therefore, during the diffusionless growth of bainitic ferrite, the newly formed ferrite initially inherits the carbon concentration of the parent austenite, since there is no time for carbon partitioning during transformation. Due to supersaturation of carbon in bainitic plate, carbon is rejected from the growing bainitic plates into the surrounding austenite, enriching it. In Bhadeshia's theory of the bainitic transformation, the T_0 line defines a fundamental thermodynamic limit for the diffusionless growth of bainitic ferrite (H. Bhadeshia, 2001). At a given transformation temperature, bainitic ferrite can grow only while the carbon concentration of the remaining austenite is lower than that specified by the T_0 condition. Under these circumstances, the austenite is thermodynamically unstable with respect to a diffusionless $\gamma \rightarrow \alpha$ transformation of identical composition, as shown in Figure 1-13. The transformation proceeds until the austenite carbon concentration reaches the T_0 limit, at which point the free energies of austenite and ferrite of the same composition become equal and further transformation becomes thermodynamically impossible. This provides a natural explanation for the incomplete reaction phenomenon commonly observed during bainitic transformations (Figure 1-13). (H. Bhadeshia, 2001).

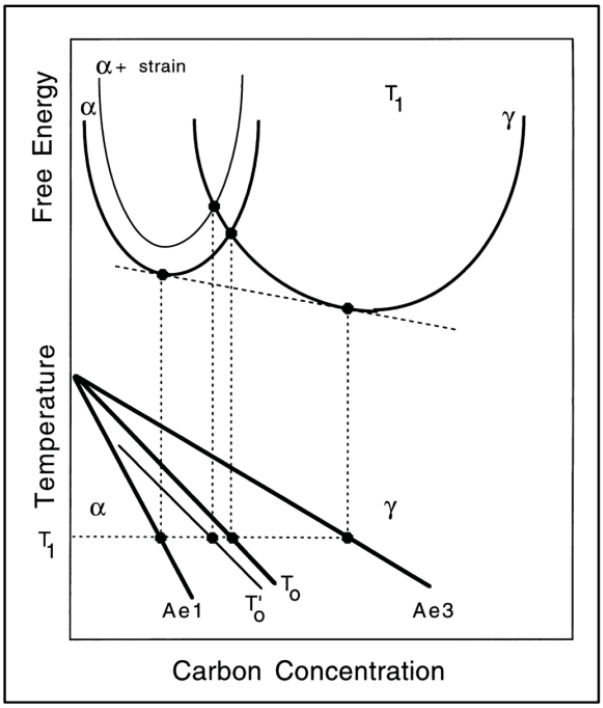

Figure 1-13 Schematic representation of free energy variation versus carbon content, showing the T_o curve

Taken from Bhadeshia (2001, p. 9)

The remaining carbon-enriched austenite after the bainitic transformation is referred to as residual austenite. Upon cooling, this residual austenite may persist to room temperature as retained austenite (RA), partially transform into martensite, or evolve into the martensite–austenite (M–A) constituent. The M–A constituent forms when only part of the carbon-enriched residual austenite transforms into untempered martensite below the Ms, leaving carbon-rich austenite surrounding the martensite islands (Bhadeshia, 2013). Retained austenite that remains fully untransformed at room temperature generally exhibits two morphologies: film-like RA, consisting of thin interlath films with high aspect ratios between bainitic ferrite plates, and blocky RA, composed of coarser equiaxed or irregular regions typically located at prior austenite grain boundaries or between bainite sheaves (Bhadeshia & Edmonds, 1980). As shown in Figure 1-14 for bainitic high-strength steel, field emission electron probe microanalyzer (FE-EPMA) reveal that film-like RA contains higher carbon

concentrations than blocky RA, with carbon content decreasing as the blocky RA size increases (Watanabe et al., 2024).

A key feature of bainitic ferrite (α) and RA is their high dislocation density, attributed to the displacive nature of bainite formation (He et al., 2018). Due to the ultrafine thickness of bainitic laths, dislocations are heterogeneously distributed between the lath interiors and boundaries. Moreover, high dislocation densities have also been observed within RA (Cornide et al., 2011). It is important to recognize that RA is not the sole secondary phase associated with bainitic transformation. The precipitation of carbides and the partial transformation of RA into martensite during cooling are integral to the final bainitic microstructure. Consequently, bainitic ferrite can be regarded as the primary phase, while secondary constituents depending on chemical composition and heat treatment may include RA, carbides, and M–A constituents, either individually or in combination. For instance, alloying elements such as Si or Al, which inhibit cementite formation, can markedly suppress carbide precipitation and thus promote the stabilization of austenite (Bhadeshia & Honeycombe, 2017). The M–A constituent represents another critical microstructural feature in bainitic steels. As It consists of untempered martensite embedded in carbon-enriched retained austenite (Bhadeshia, 2013), it exhibit high hardness due to their elevated carbon content and the presence of brittle untempered martensite, leading to local heterogeneity in hardness and mechanical response (Mohammadijoo et al., 2018). Jiang et al. (Jiang et al., 2021) demonstrated through electron probe microanalysis that M–A zones display a pronounced carbon concentration gradient relative to the bainitic ferrite matrix, whereas other alloying elements remain uniformly distributed. This non-uniform distribution of carbon within M–A zones is illustrated in Figure 1-15c.

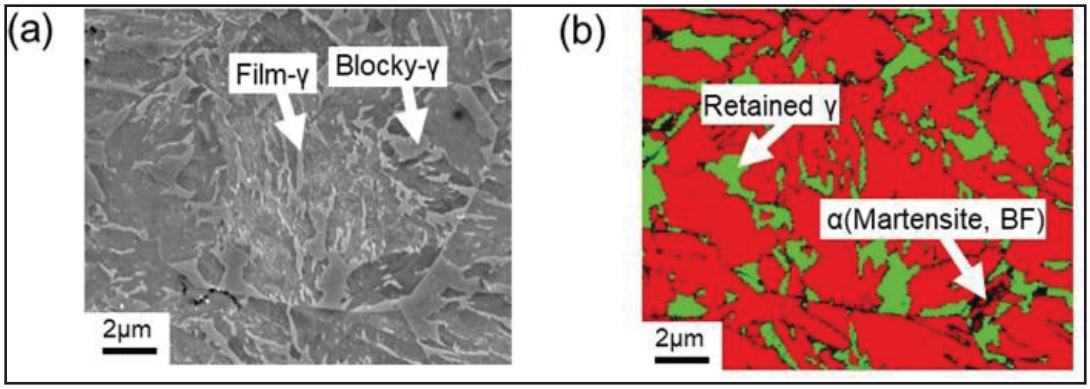

Figure 1-14 SEM and phase map of bainitic microstructure showing retained austenite in two morphologies: thin film-like layers and blocky regions

Taken from Watanabe et al. (2024, p. 1469)

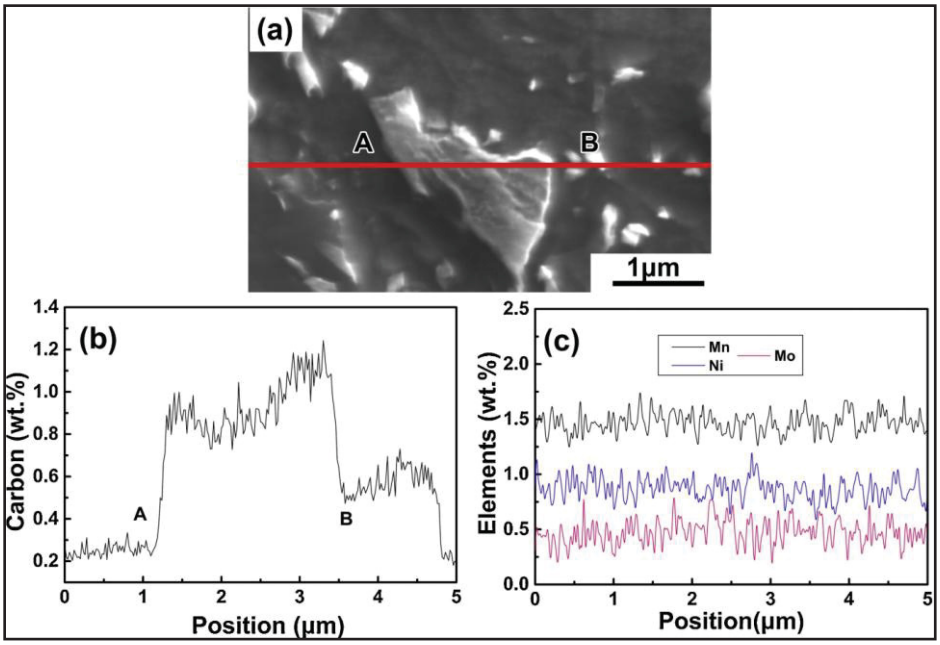

Figure 1-15 Alloying elements concentration measured by EPMA in M-A zone: (a) SEM micrograph, (b) carbon distribution, and (c) distribution of alloying elements

Taken from Jiang et al. (2021, p. 3)

1.3.2.3 Morphologies of Bainite

Bainitic microstructures exhibit various morphologies, each influencing the final properties of the material (Królicka et al., 2023). In particular, the mechanical properties of bainitic steels are highly sensitive to the morphology. Therefore, it is crucial to understand bainite morphology at the scale where these properties are determined. However, bainite is among the most complex microstructures in steel, making quantitative interpretation challenging (Bramfitt & Speer, 1990).

In the literature, various classifications of bainitic morphologies have been proposed. One of the most comprehensive was introduced by Zajac (Zajac et al., 2005), who identified five distinct morphologies of bainite: granular bainite (GB), upper bainite (UB), degenerate upper bainite (DUB), lower bainite (LB), and degenerate lower bainite (DLB) which are shown schematically in Figure 1-16. In the first classification, based on the morphology of bainitic ferrite, two types of bainite are identified: granular and plate-like. Within the plate-like category, a further classification is made based on the location of the second phase (carbides, M/A, or retained austenite), as shown in Figure 1-16.

GB is considered to form only during continuous cooling and is defined as a microstructure composed of irregular ferrite grains with uneven grain boundaries, containing carbon-rich second-phase constituents (M-A) distributed between the ferrite grains (Jentner et al., 2023). Caballero et al. (Caballero et al., 2012) reported that larger PAGS and slower cooling rates favor the formation of GB at the expense of plate-like bainite (PB).

UB displays a lath-like ferrite structure, as it forms at lower temperatures than granular bainite. The second phase, which precipitates from carbon-enriched residual austenite, is always cementite. In a typical UB microstructure, elongated ferrite laths are organized into packets, with cementite distributed along the boundaries of the laths (Zajac et al., 2005). DUB is a form of upper bainite that develops when cementite formation is suppressed, resulting in a microstructure composed of lath-like ferrite with carbon-enriched residual austenite or M-A constituent located along the lath boundaries.

LB, also exhibits a lath-like ferrite morphology. In this respect, low-carbon LB is similar to UB, but it differs from LB in higher-carbon steels, where the ferrite assumes a plate-like morphology (Bramfitt & Speer, 1990). DLB is a newly identified form of lower bainite observed in complex MoNiCuCrB steels (Zajac et al., 2005). This microstructure does not fit the conventional definition of lower bainite and is therefore referred to as degenerated lower bainite. The presence of intra-lath M-A constituents replacing cementite indicates that DUB results from an incomplete transformation, which prevents the formation of cementite.

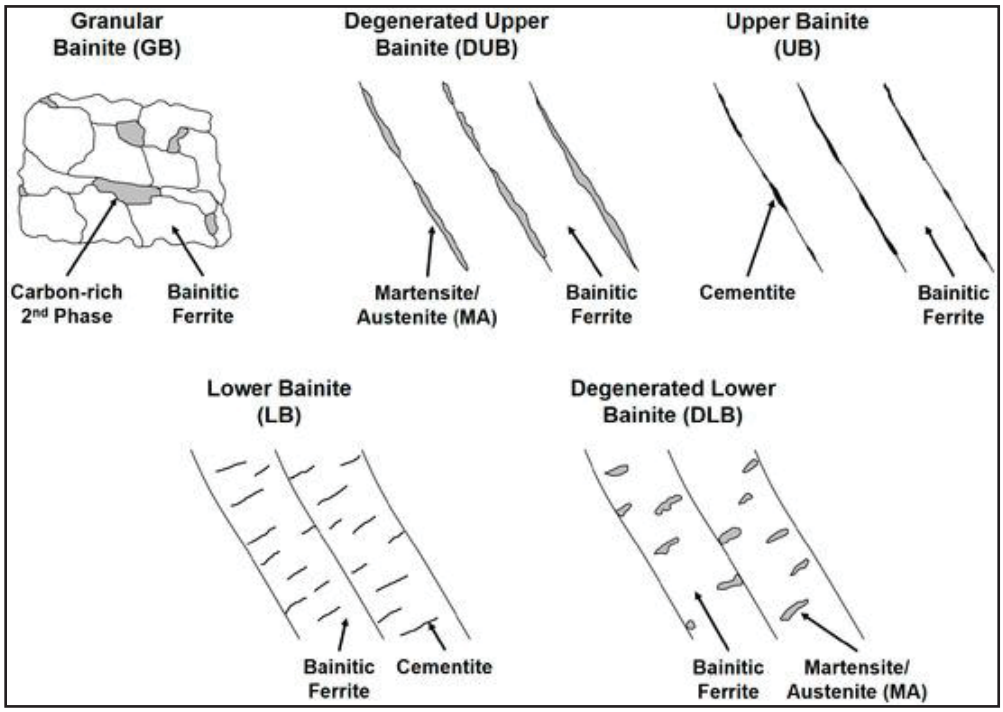

Figure 1-16 Schematic illustration of the five bainite morphologies proposed by Zajac
Taken from Zajac et al. (2005, p. 2)

In general, disregarding the second-phase morphology, bainite can be categorized into two types: granular and plate-like morphologies. Previous studies indicate that both bainitic morphologies originate from the same displacive transformation mechanism (H. Bhadeshia, 2001; Caballero et al., 2012). However, De-Castro et al. (De-Castro et al., 2022) reported that plate-like bainite (PB) exhibits a higher fraction of boundaries with misorientation angles

greater than 50° compared with granular bainite (GB). This observation suggests that, despite sharing a common transformation mechanism, PB develops finer crystallographic packets and high-angle blocks. Consequently, lath-like bainite contains a higher density of high-angle boundaries, which enhances its overall boundary area and potential for strengthening.

1.4 Key Parameters Governing Bainitic Transformation

Bainitic phase transformation can occur under two main processing routes continuous cooling and isothermal holding, each influenced by a range of thermodynamic and kinetic parameters that govern transformation rate, morphology, and the resulting mechanical properties. Among these, chemical composition, particularly the C and Si contents, is the most critical (Lin et al., 2022; Wu et al., 2024). Other influential factors include the PAGS, austempering temperature, and holding time.

In the case of continuous cooling transformation, additional parameters such as cooling rate and the formation of pre-bainitic phases (e.g., ferrite, pearlite) can substantially modify the transformation pathway. For isothermal bainite formation, key factors include austenite grain size (Lan et al., 2011), cooling rate prior to isothermal holding (X. Long et al., 2023), austempering temperature, holding time, temperature uniformity, and the final cooling rate after isothermal treatment. Moreover, external stress or deformation applied during transformation may significantly influence the kinetics and morphology of bainite (Benrabah et al., 2024). Altogether, the literature emphasizes the complex, multivariable nature of bainitic transformation. The following paragraphs introduces two parameters: PAGS and austempering temperature, which are analyzed in detail in Chapters 3 and 4.

PAGS, critically influences the bainitic transformation by affecting nucleation kinetics, transformation start temperature, and the morphology and stability of the resulting phases. Sun et al. (Sun et al., 2020) reported that in high-carbon steels undergoing isothermal transformation, increasing PAGS accelerated bainitic transformation due to higher austenite yield strength accompanying grain refinement. Conversely, Ueji et al. (Ueji et al., 2021) found that in medium-carbon, high-silicon steels, refining PAGS promoted transformation by increasing the density of bainite nucleation sites.

PAGS also impacts the volume fraction and morphology of RA. Ueji et al. (Ueji et al., 2021) observed that refining PAGS reduced RA fraction and promoted a blocky RA morphology, as shown in Figure 1-17. It can be seen that phase maps of samples austenitized at 850 °C (a, c, e) or 1050 °C (b, d, f) and then held isothermally at 400 °C (a, b), 450 °C (c, d), or 500 °C (e, f) for 1800 s. White lines indicate prior austenite grain boundaries (Ueji et al., 2021).

In contrast, Hasan et al. (Hasan et al., 2020) reported that larger PAGS favored bainite formation and enhanced carbon partitioning to austenite, resulting in a higher RA fraction. Mandal et al. (Mandal et al., 2022) later found that, in medium-carbon, high-silicon steels, smaller PAGS refined the RA morphology, increased its carbon content, and elevated the RA volume fraction. Collectively, the above findings underscore the strong influence of PAGS on both bainitic and austenitic phase evolution.

The austempering temperature strongly governs carbon supersaturation in austenite and thus controls the relative fractions of bainite, martensite, and RA, as well as transformation kinetics and the mechanical properties of the final microstructure (X. Y. Long et al., 2023; Su et al., 2022). Lowering the austempering temperature increases the bainite fraction by enhancing the thermodynamic driving force for transformation (i.e., the difference in Gibbs free energy between austenite and bainite) (Bhadeshia & Christian, 1990; X. Y. Long et al., 2023; Tian et al., 2018). This temperature also influences the formation of secondary phases. For example, Mondal et al. (Mondal et al., 2021) reported substantial variations in the relative amounts of bainite, martensite, and RA at different austempering temperatures in medium-carbon, high-silicon steels, highlighting the strong temperature dependence of phase stability, as summarized in Table 1-1.

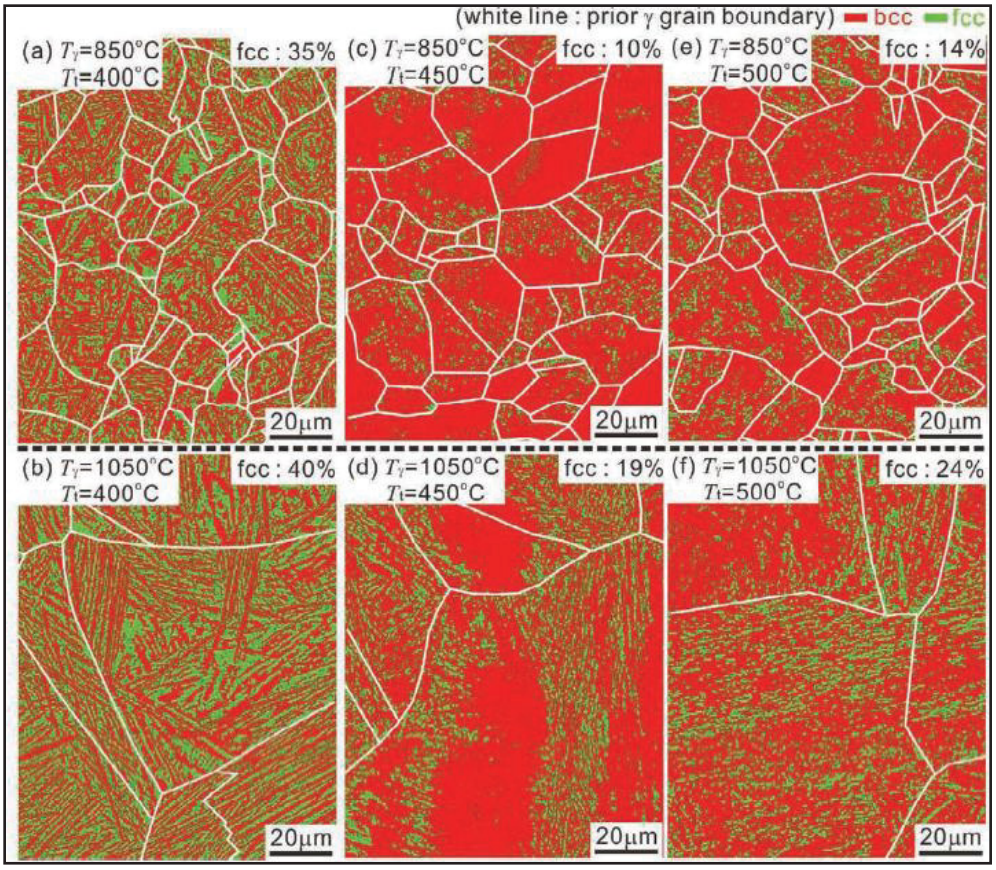

Figure 1-17 Phase maps of samples austenitized at 850 °C (a, c, e) or 1050 °C (b, d, f) and then held isothermally at 400 °C (a, b), 450 °C (c, d), or 500 °C (e, f) for 1800 seconds. The white lines mark the prior austenite grain boundaries

Taken from Ueji et al. (2021, p. 586)

Table 1-1 Phase volume fractions estimated following isothermal treatment. V_{AM} (athermal martensite), V_{BF} (bainitic ferrite), V_{FM} (fresh martensite), and V_{RA} (retained austenite)

Taken from Mondal et al. (2021, p. 3)

Temperature (°C)	V_{AM} (%)	V_{BF} (%)	V_{FM} (%)	V_{RA} (%)
350	4.60	77.65	–	17.75
400	–	76.74	13.50	9.76
450	–	14.46	79.09	6.45

1.5 Tempering of Bainite

Tempering is a heat treatment consisting of heating the material to a temperature belowe the critical temperature (Ac_1) and holding for a specific time, during which the microstructure and mechanical properties change (Bhadeshia & Honeycombe, 2017). Several fundamental phenomena occur during tempering, generally in the order presented, although some overlap is observed (Reed-Hill et al., 1973). They are as follows:

Redistribution of carbon atoms occurring approximately between room temperature and 100 °C, segregation of carbon atoms to lattice defects, such as dislocations, precipitation of a transition carbide or carbides, decomposition of retained austenite conversion of the transition carbide and segregated carbon into small rod-shaped cementite particles, spheroidization of the rod-shaped cementite, alloys carbides formation, recovery of the ferrite structure, recrystallization of the ferrite structure, Ostwald ripening of cementite.

It should be noted that all the aforementioned phenomena are associated with the tempering of martensite. However, some of these reactions may also occur during the transformation itself, particularly in bainite, where auto-tempering takes place due to the higher transformation temperatures (H. Bhadeshia, 2001). As an example, during the bainite reaction, carbon quickly redistributes from supersaturated ferrite to residual austenite, while carbides precipitate, representing true autotempering effects. The following sections discuss the most significant phenomena occurring during the tempering of bainite.

1.5.1 Bainitic Ferrite Evolution

In bainitic microstructures, bainitic ferrite typically exhibits only a limited degree of carbon supersaturation, as most carbon atoms either diffuse into the surrounding austenite or precipitate as cementite (H. Bhadeshia, 2001). However, atom probe tomography studies have demonstrated that bainitic ferrite may remain supersaturated with carbon in high-Si steels, where cementite precipitation is strongly suppressed (Garcia-Mateo et al., 2015).

During subsequent tempering, recovery processes manifested as a reduction in dislocation density occur within bainitic ferrite (Ståhlkrantz et al., 2020). The tempering temperature is a dominant factor controlling this decrease in dislocation density (Garcia-Mateo & Caballero, 2005).

At higher tempering temperatures, rapid softening ensues, as bainitic ferrite plates evolve toward a more equiaxed morphology through recrystallization and grain growth. The driving force for recrystallization arises from the stored energy associated with dislocations and elastic strains. Concurrently, extensive spheroidization and coarsening of carbides occur, further contributing to the softening of the microstructure (H. Bhadeshia, 2001).

1.5.2 Retained Austenite Evolution

As discussed in the previous section, RA is a carbon-enriched constituent present in the bainitic microstructure at room temperature, typically appearing in two morphologies: film-like and blocky (H. Bhadeshia, 2001). According to Bhadeshia (H. Bhadeshia, 2001), the decomposition behavior of RA during tempering depends on its morphology. Blocky RA tends to decompose into pearlite colonies, whereas film-like RA transforms into discrete cementite particles within a ferritic matrix. In contrast, Yan et al. (Yan et al., 2017) observed that the decomposition products of RA may range from ferrite + rod-shaped carbides to bainite, depending on the tempering conditions such as temperature and holding time.

Besides RA decomposition during tempering, residual RA can also transform into fresh martensite during the final cooling to room temperature. Sourmail et al. (Sourmail et al., 2021) identified this transformation using dilatometry, where a characteristic expansion occurs near 100 °C, indicating martensitic formation upon cooling. The accompanying strain–temperature and derivative curves (Figure 1-18) confirm this transformation. The low transformation temperature reflects the high carbon content and corresponding stability of the residual austenite prior to cooling.

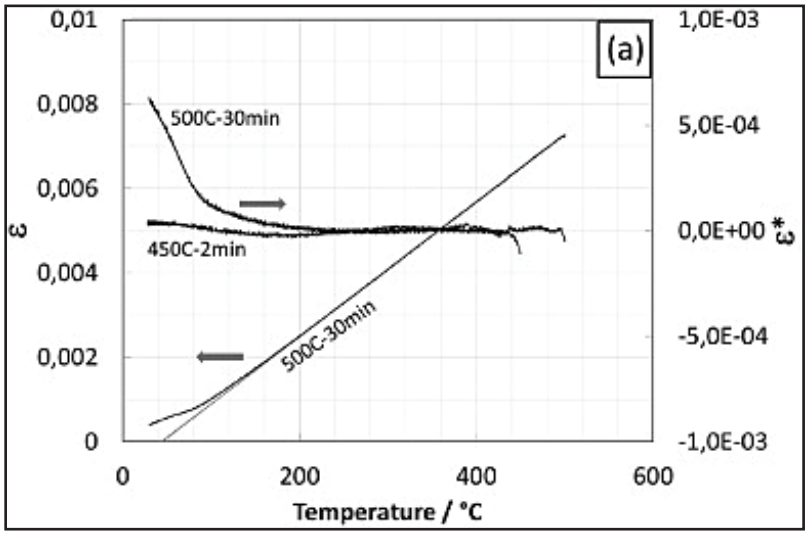

Figure 1-18 Strain versus temperature during final cooling after tempering for 30 minutes at 500 °C for the 200 V material

Taken from Sourmail et al. (2021, p. 6)

1.5.3 Martensite – Austenite Constituent Evolution

The high hardness of M–A constituents, typically associated with untempered martensite, adversely affects both crack initiation and propagation (Lambert-Perlade et al., 2004). Therefore, one of the aims of tempering is to achieve the complete decomposition of these zones.

In low-carbon, low-alloy steels, the decomposition of M-A zones results in the formation of stringy carbides that accumulate within the initial M-A regions, as shown in Figure 1-19. Similar results have shown the formation of aggregated carbide–ferrite zones resulting from the decomposition of M-A constituents during tempering (Jiang et al., 2021; B. Wang et al., 2023).

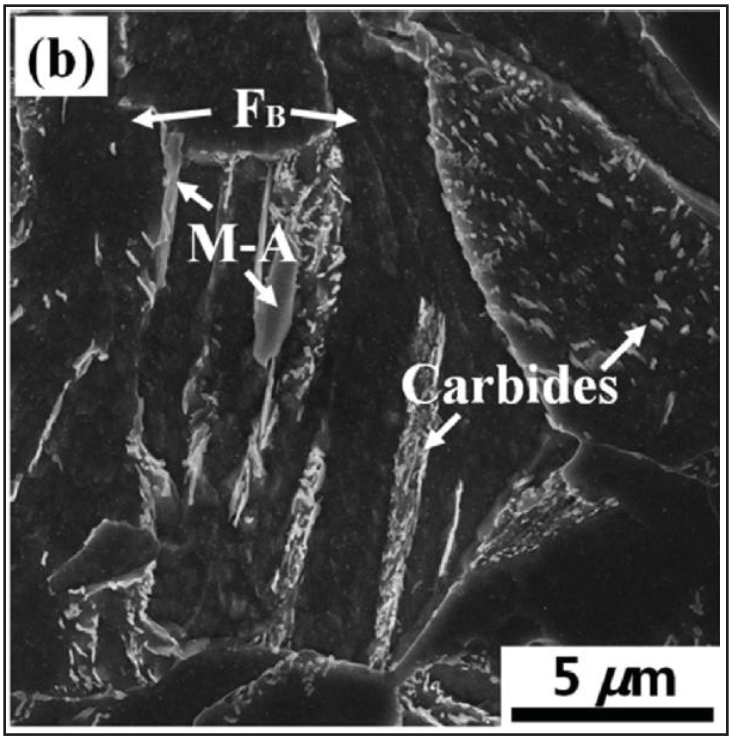

Figure 1-19 SEM micrographs of the steel samples tempered at 580 °C
Taken from Li et al. (2016, p. 249)

1.5.4 Carbides Evolution

Carbides play a crucial role in the properties of tempered bainitic steels; therefore, their size, distribution, morphology, and location are important factors. The evolution of carbides involves several stages: the transformation of unstable carbides into stable ones, the precipitation of new carbides from the supersaturation of bainitic ferrite and RA, and finally the coarsening of carbides. However, significant differences exist between martensite and bainite in this regard, as the auto-tempering process means that much of this evolution has already occurred in the bainitic microstructure.

Depending on tempering time and temperature, different types of carbides with varying thermal stabilities such as M_3C, M_2C, M_6C, M_7C_3, and $M_{23}C_6$ may precipitate (Mitchell & Ball, 2001). As shown in Figure 1-20, the stability of different carbides varies with temperature;

however, chemical composition of the carbide also plays a crucial role. Increasing the tempering time and temperature leads to the transformation of metastable carbides, such as M2C, into more stable equilibrium carbides like M_7C_3 and $M_{23}C_6$ (Talebi et al., 2018).

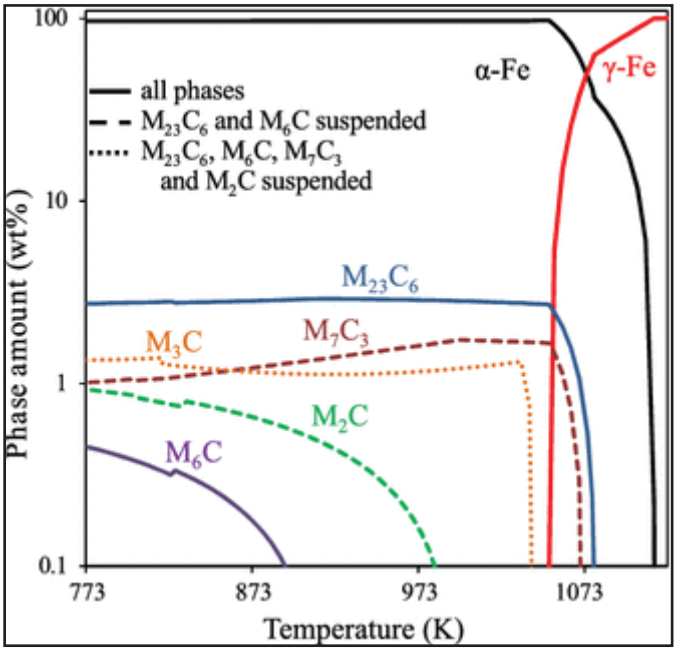

Figure 1-20 Carbide Stability Diagrams Predicted by MatCalc
Taken from Dépinoy et al. (2017, p. 2166)

Figure 1-21 presents experimental data on the coarsening of cementite during the tempering of medium-carbon steel at 700 °C. The top boundary of each shaded region corresponds to the mean particle size at the lath boundaries, whereas the bottom boundary reflects the mean particle size inside the laths. The results indicate a significant difference in carbide coarsening between bainite and martensite as the initial microstructures. In addition, the carbide location (inter-lath or intra-lath) plays a crucial role in the coarsening behavior, as the rapid diffusion of carbon leads to more pronounced coarsening of inter-lath carbides compared with intra carbides (Xie et al., 2022). Nevertheless, due to the stability of bainite and its resistance to tempering, only a slight increase in particle size about 110 nm even after 100,000 seconds (27 hours) of tempering was observed in the bainitic microstructure.

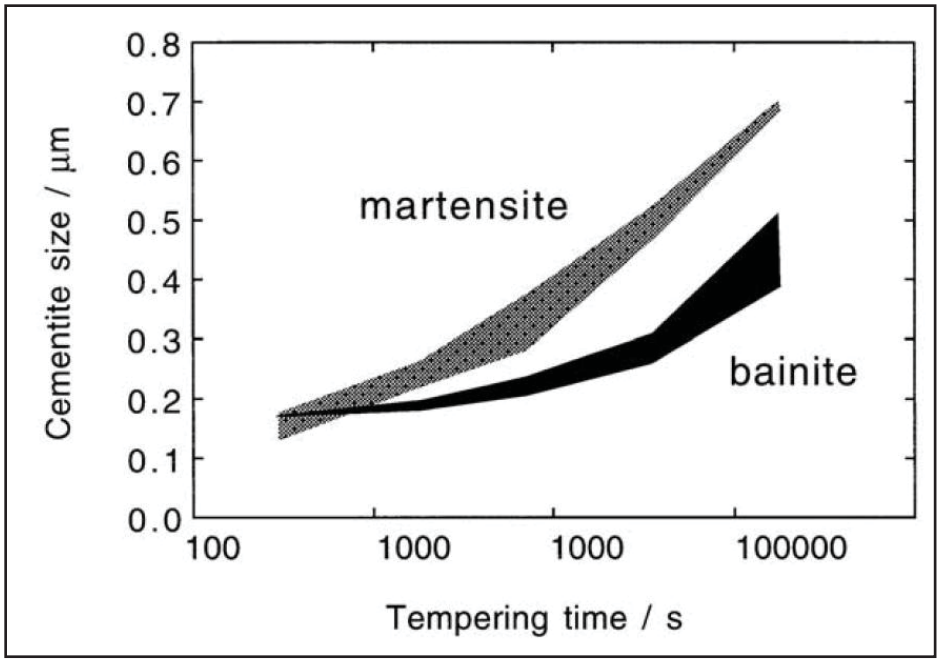

Figure 1-21 Variation in the size of cementite particles during tempering at 700 °C for different initial microstructures. The upper limit of each shaded area denotes the average size of particles situated at lath boundaries, while the lower limit represents those located within the laths

Taken from Bhadeshia (2001, p. 99)

It appears that tempering temperature, rather than tempering time, plays the dominant role in providing the activation energy for carbide coarsening. Ståhlkrantz et al. (Ståhlkrantz et al., 2020) reported no significant change in particle size at 300 °C, even after tempering for two different durations 10 minutes and 24 hours, as shown in Figure 1-22.

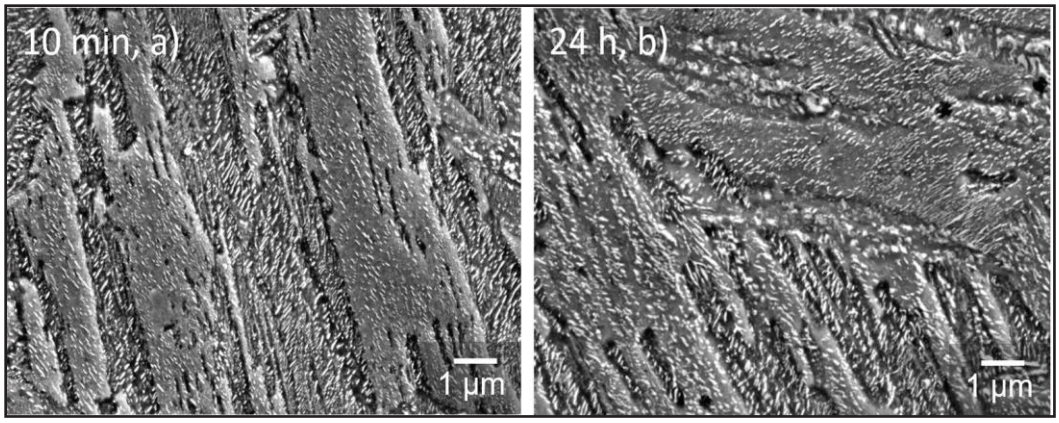

Figure 1-22 SEM micrographs after isothermal heat treatment at 300 °C for (a) 10 minutes and (b) 24 hours

Taken from Ståhlkrantz et al. (2020, p. 6474)

1.6 Medium-Carbon Low-alloy steels

One method for classifying carbon and alloy steels based on their chemical composition, as illustrated in Figure 1-23 (Javed et al., 2024). This system divides steels into carbon steels (low, medium and high) and alloy steels (low and high).

Carbon steels with less than about 2% alloying elements are one of the most widely used ferrous metals. Adjusting its alloy composition or modifying how it's manufactured allows its properties to be tailored for specific uses, such as enhanced tensile strength. Adding elements like chromium, for example, can improve corrosion resistance and make the steel more suitable for harsh environments, including marine settings. Likewise, processing steps such as heat treatment can change the steel's microstructure, which in turn affects both mechanical performance and resistance to corrosion. Techniques like quenching and tempering can significantly increase strength and toughness, but if done improperly, they may create brittle microstructures that make the steel more prone to corrosion. Overall, both, alloying choices and processing methods directly shape the steel's internal structure (Javed et al., 2024).

As one of the most well-known categories, medium-carbon low-alloy steels are extensively employed in the transportation industry, with typical applications including shafts, forgings, crankshafts, couplings, axles, and gears (Davis, 1998). The primary alloying elements in this

steel group are Mn, Cr, and Mo and the compositional range of these steels is presented in reference (Singh, 2011).

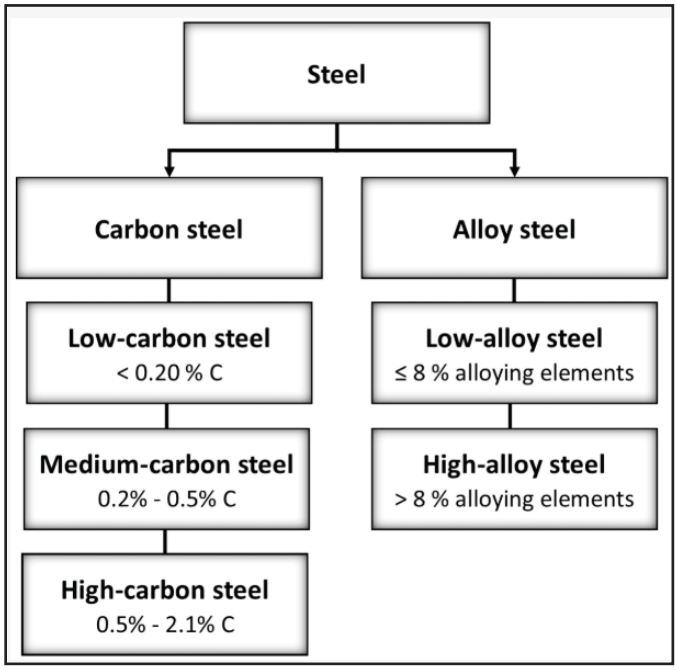

Figure 1-23 Categorization of steels determined by their chemical constituents
Taken from Javed et al. (2024, p. 5)

1.6.1 Mold Applications

In recent years, the use of medium-carbon low-alloy steels, particularly mold steels, has expanded significantly within the manufacturing sector. This expansion is especially evident in the production of large plastic injection molds for the automotive industry, which is the focus of this study. These molds are notable for their substantial dimensions, often extending several meters in length.

A prominent example of such mold steels is the AISI P20 standard, as reported by the American Iron and Steel Institute (AISI), a medium-carbon low-alloy tool steel recognized for its good toughness at moderate strength levels, good machinability, polishability, and wear

resistance. The alloying composition of AISI P20, as shown in Table 1-2, which is correspond to standard DIN 2738.

Table 1-2 Chemical composition of medium carbon low alloy steels based on standard DIN 2738 (%wt)

C	Mn	Si	Cr	Mo	P	S	Fe
0.28-0.40	0.6-1.00	0.20-0.40	1.40-2.00	0.30-0.55	<0.03	<0.03	Bal.

Typically, AISI P20 is equivalent to the above DIN standard grade with added Ni and; exhibits a hardness in the range of 280–320 Brinell hardness (HB). The addition of approximately 1% nickel enhances through-hardening capability. This steel also offers good machinability, is suitable for texturing and fine polishing, provides adequate corrosion resistance.

1.6.2 Manufacturing Challenges

The manufacturing process of large steel blocks, as shown schematically in Figure 1-24 involves several key steps, including casting, forging, heat treatment (austenitization, quenching, and tempering), and final machining (Firrao et al., 2006). Among these stages, heat treatment is particularly critical, as it governs the phase transformations that define the final microstructure and properties of the steel. The process begins by heating the steel into the austenitization region, which is define based on the chemical composition of steel and followed by cooling in the water bath. Depending on factors such as composition and cooling rate, a variety of microstructures can form during this stage.

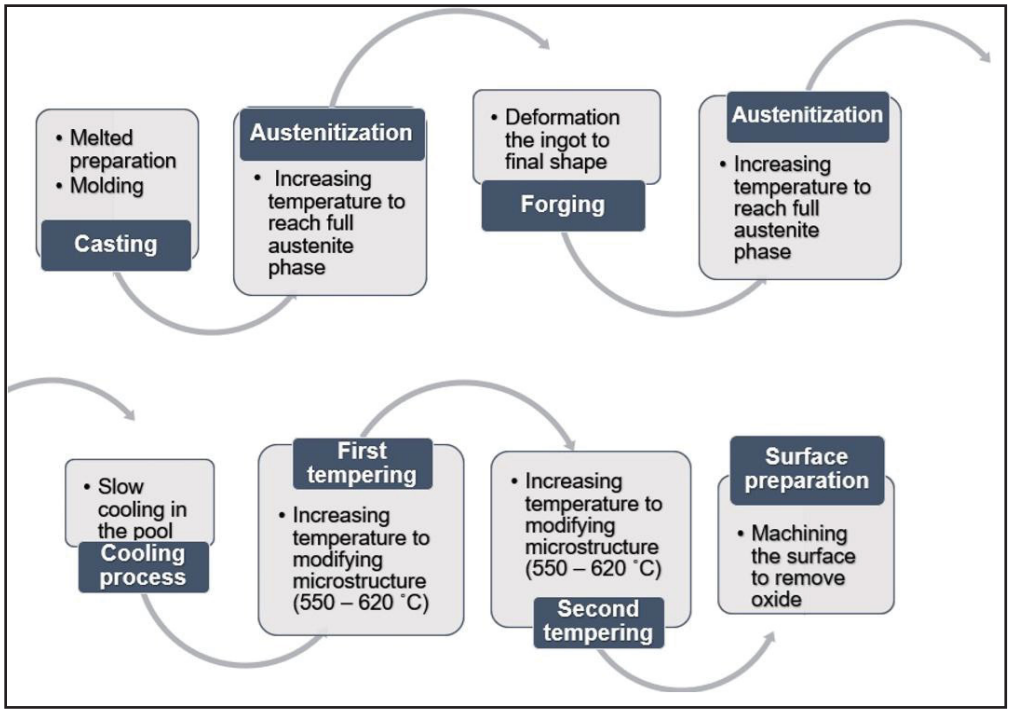

Figure 1-24 Schematic of manufacturing process of large steel blocks

The production of large-scale components, such as plastic injection molds exceeding one meter in length and possessing substantial cross-sectional dimensions, presents significant manufacturing challenges.

The first challenge arises during the casting process, where segregation of alloying elements can occur. During the solidification of metallic alloys, partitioning of solute elements between the liquid and solid phases results in an uneven chemical distribution. Due to the limited atomic diffusion within the solid phase during solidification, microsegregation develops on a fine scale, whereby interdendritic regions become enriched in solute relative to dendrite cores. On a macroscopic scale, macrosegregation produces compositional variations across extended regions of the casting (Thomas, 2009).

In the subsequent forging stage (about 1250 °C), substantial strain heterogeneity occurs due to the large thickness of the block within. Finite element simulations of the open-die forging process, typically applied to such large steel components, reveal pronounced strain gradients

from the surface to the core, as illustrated in Figure 1-25. Consequently, the austenite grain size varies significantly between these regions (Dhondapure et al., 2024). These gradients affect the subsequent phase transformation behavior, leading to differences in transformation kinetics, morphology, and mechanical properties, and ultimately determining the final microstructural distribution (Lee et al., 2008).

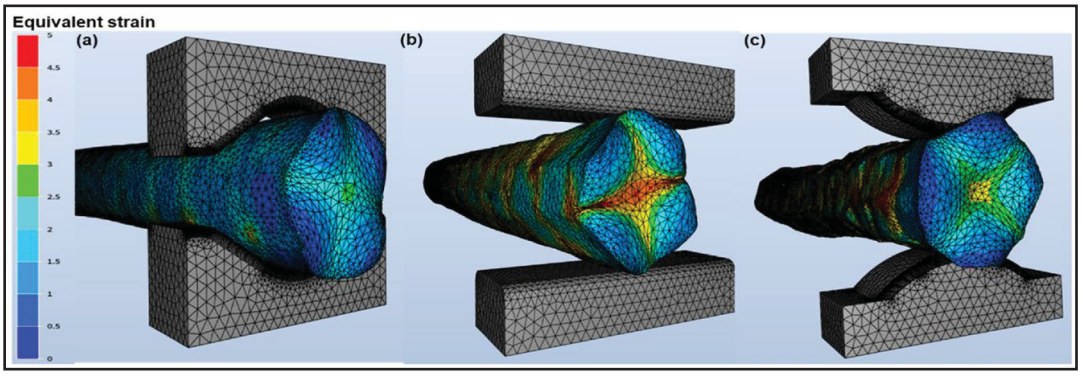

Figure 1-25 Strain distribution at the end of cogging for concave (a), flat (b), and convex (c) dies, based on finite element simulation

Taken from Dhondapure et al. (2023, p. 8251)

During the subsequent water quenching step, the large thickness again becomes critical, generating pronounced differences in cooling rates between the surface and the core of the block. Industrial scale experiments by Bouissa et al. (Bouissa et al., 2021) demonstrated that the center cools considerable more slowly, at an average rate of 0.05 °C/s, whereas the surface cools nearly twice as fast, around 0.1 °C/s (Figure 1-26).

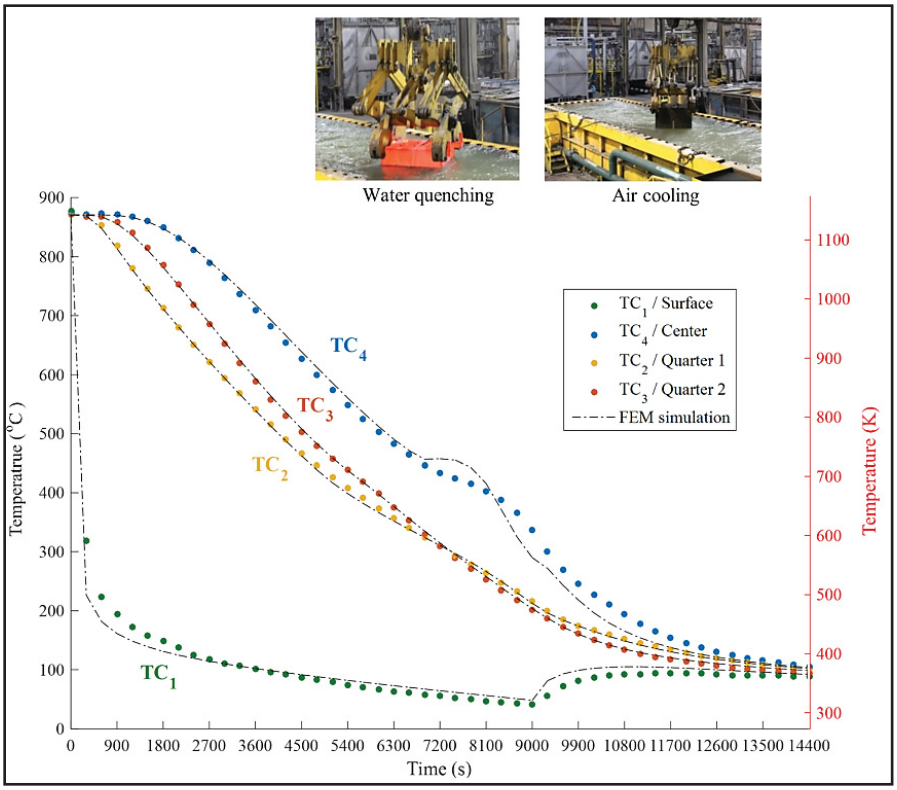

Figure 1-26 Temperature evolution from the surface to the center during the quenching of a large steel block in a water bath

Taken from Bouissa et al. (2021, p. 1892)

This disparity produces variations in phase transformation products and hardness from the surface inward. Hurel (Hurel, 2022) showed that, in medium-carbon low-alloy steel, the microstructure at cooling rates of 0.1 and 0.05 °C/s both exhibits granular bainite, as seen in Figure 1-27b and c, respectively. While the scanning electron microscopy (SEM) analysis indicates a significant variation in the volume fraction of the M-A constituent between these two cooling rates.

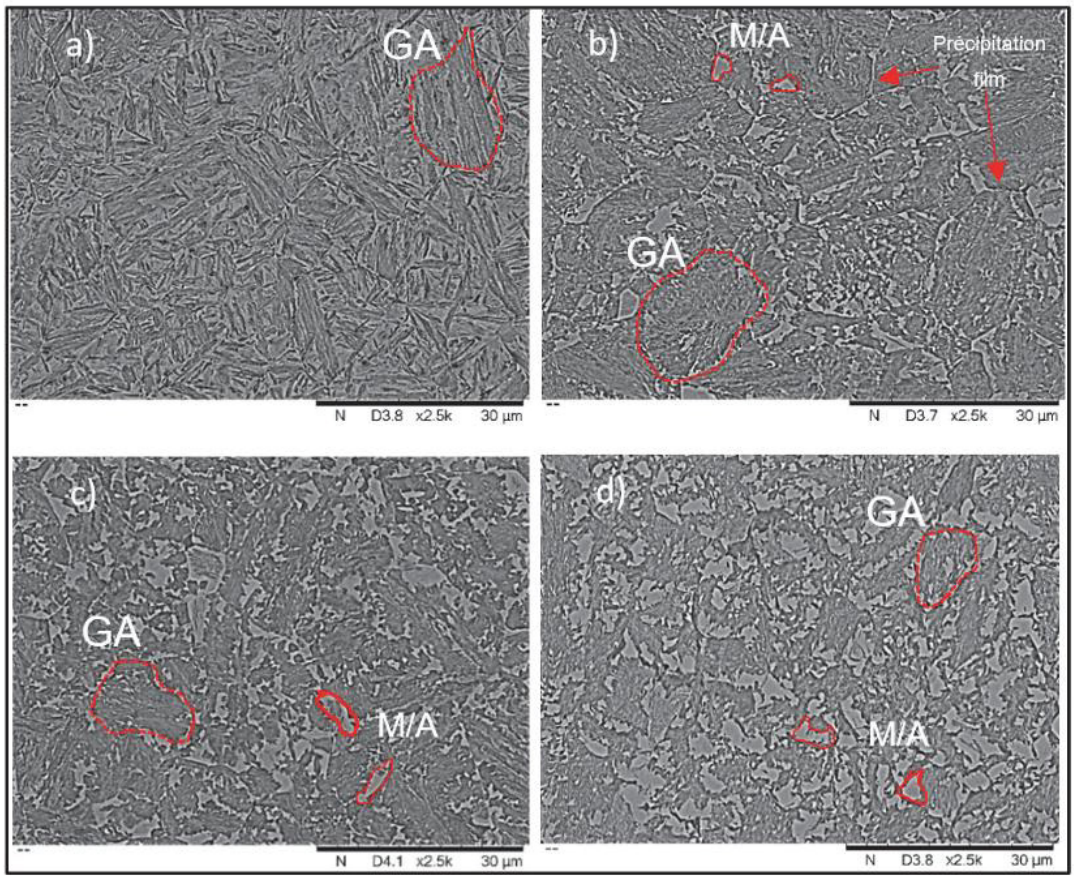

Figure 1-27 Scanning electron microscope (SEM) images showing austenite grains (GA) and martensite/austenite (M/A) blocks in bainitic microstructures under different cooling rates: (a) 0.3 °C/s, (b) 0.1 °C/s, (c) 0.05 °C/s, and (d) 0.01 °C/s

Taken from Hurel (2022, p. 56)

In the next step, tempering process of large steel blocks also presents difficulties. While the surface may quickly reach the target tempering temperature, it can take more than ten hours for the core to achieve the same temperature. Consequently, the surface and the center may experience different tempering conditions, potentially leading to variations in final properties. Figure 1-28 presents a simulation of the time required to reach the target temperature during tempering of an industrial large steel block at its central cross-section. The results show that even after 27 hours, while the corners and surface of the block have reached the target temperature, the center remains below it.

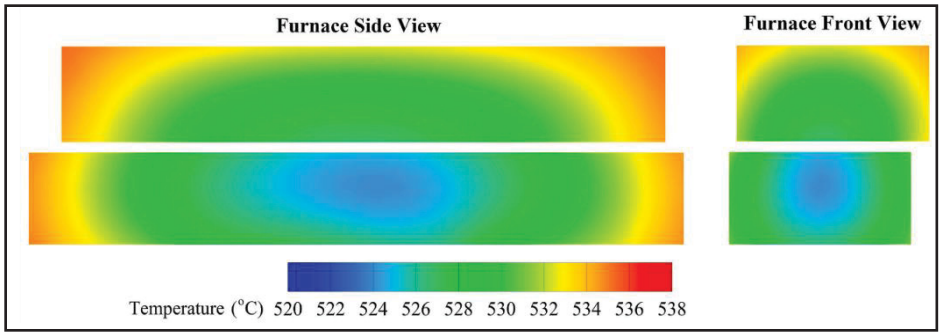

Figure 1-28 Temperature contour of two loaded large steel blocks at the central cross-section at t = 100,000 s during tempering process, with a target temperature of 537 °C

Taken from Mirzaei et al. (2024, p. 12)

1.7 Research Gap and Contribution of this Work

The steel industry has achieved substantial advances in producing large-size components; however, each stage of manufacturing still presents distinct challenges. The main factor underlying these difficulties is the considerable section thickness, which significantly affects material behavior during casting, forging, quenching, and tempering. Such complexities are less evident or entirely absent in smaller parts, making large component production inherently more intricate and difficult to control.

Despite the industrial relevance of these issues, there remains a clear gap in the literature addressing the specific challenges associated with large-size components. Most existing studies focus on small or medium sections, often overlooking the scale-dependent phenomena that govern the microstructural evolution and mechanical performance of massive blocks. Bridging this gap through targeted research is thus essential to optimize manufacturing practices and ensure reliability and uniform quality of large medium-carbon, low-alloy steel parts.

From both scientific and industrial standpoints, understanding the influence of these factors is crucial for improving process control and product consistency. To address the gaps identified

in previous research, three sub-objectives were defined, each focused on a different stage of the manufacturing process.

The first sub-objective investigates the effect of the large austenite grain size gradient, from surface to core, on phase transformation behavior during slow continuous cooling representative of industrial quenching. In this part, the prior austenite grain size distribution in an actual block was characterized, and its influence on transformation kinetics, microstructure, and hardness at both micro and nano scales was analyzed.

The second sub-objective examines the effect of the isothermal bainitic transformation temperature as a potential manufacturing route for mold steels, emphasizing its role in modifying microstructure and hardness. Experiments were carried out under laboratory and industrially relevant conditions, and the global and local phase hardness were evaluated by nanoindentation, providing new insights into AISI P20 steels. The third sub-objective addresses the influence of block thickness on non-uniform tempering during the non-isothermal stage of the process. Numerical simulations and experimental tests were combined to assess how temperature gradients and carbide coarsening affect properties such as surface finish and polishability after long tempering cycles.

Collectively, these sub-objectives elucidate the key parameters controlling the manufacturing of large steel blocks and their impact on the resulting structural and mechanical properties, offering a comprehensive framework for both scientific understanding and industrial optimization.

CHAPTER 2

Material and Methods

2.1 Materials

The samples used in this study were manufactured by Fink Steel-Sorel, Quebec, Canada. Initially, a 25.4 mm-thick slice was cut longitudinal from the as-forged block, as illustrated in Figure 2-1.

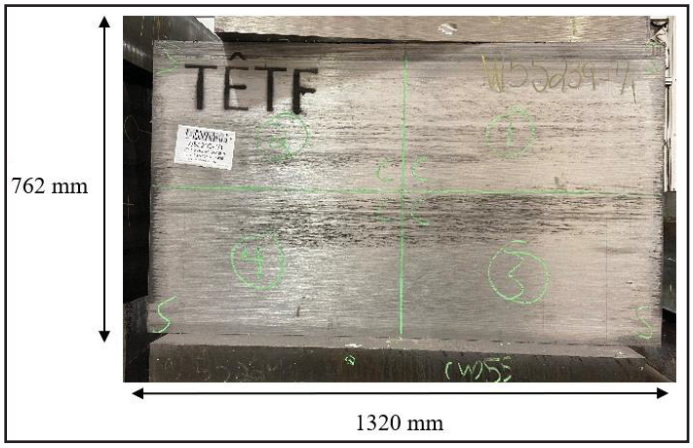

Figure 2-1 Section of industrial as-forged steel block

In the second stage, as schematically illustrated in Figure 2-2, the sliced section was divided into four smaller bars, each representing different zones from the surface to the center of the block, as shown in Figure 2-2a–c.

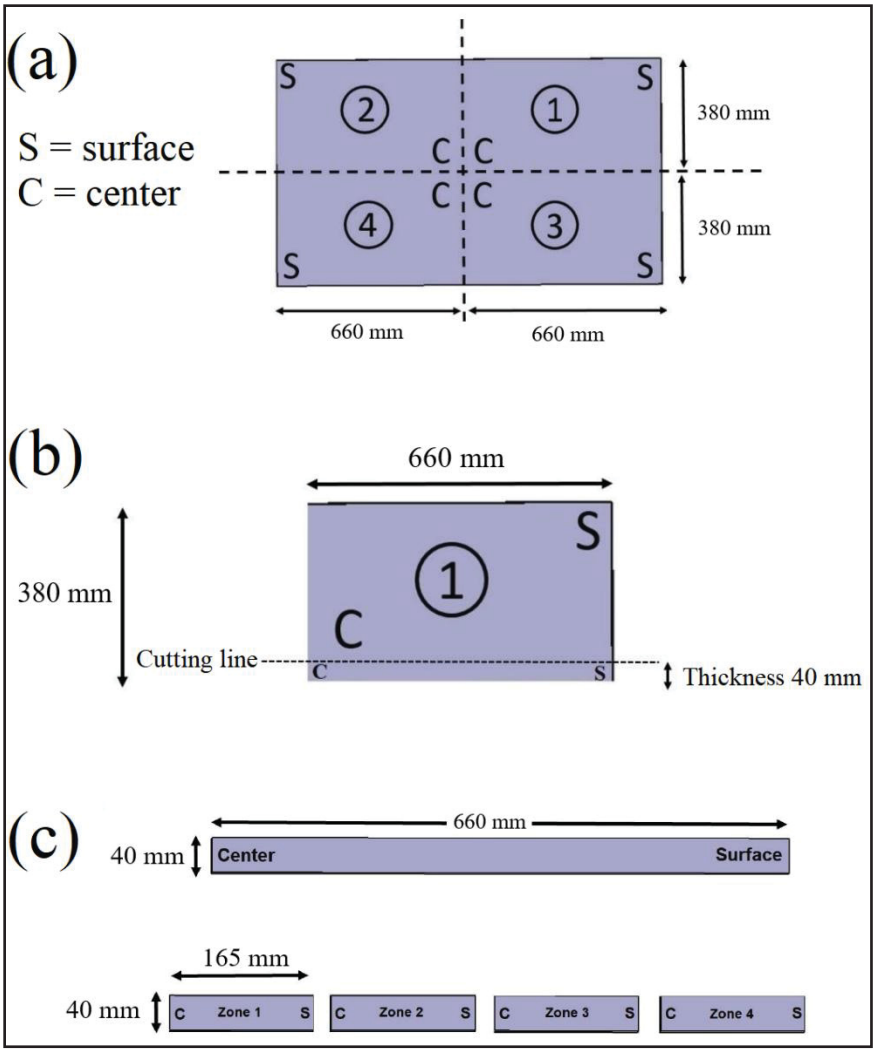

Figure 2-2 Schematical process of cutting of industrial steel block

The chemical composition of the alloy was determined using a SPECTROMAXx LMF08 (Ametec, Kleve, Germany) (Figure 2-3). Each measurement was performed five times to ensure the reliability and reproducibility of the results (Figure 2-4). The spectrometric analysis revealed the absence of compositional segregation from the surface to the center of the block. The detailed chemical composition is provided in Table 2-1. It should be noted that the composition and details of the microalloying used in this steel are proprietary and confidential; therefore, they cannot be reported in this thesis.

Figure 2-3 SPECTROMAXx LMF08, Ametec, Kleve, Germany

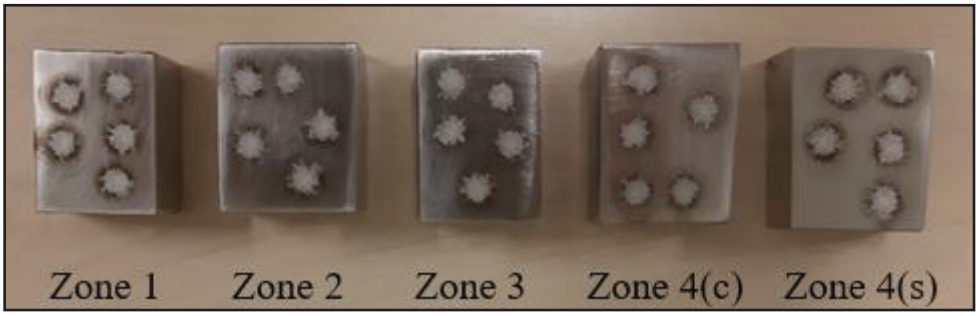

Figure 2-4 Samples analyzed by spectrometer from surface to center zones of the block, the designated zones are defined according to Figure 2-2

Table 2-1 Chemical composition of the steel investigated in this study, (%wt)

C	Mn	Si	Ni	Cr	Mo	Micro-alloys	Fe
0.26 ±0.002	1.15 ±0.017	0.35 ±0.004	0.7 ±0.01	1.5 ±0.012	0.55 ±0.011	<0.2	Balance

2.2 Dilatometry technique

The principal instrument employed for evaluating phase transformation and following tempering process in this study was a high-resolution dilatometer DIL805 A/D (Figure 2-5). The fundamental of dilatometry involves measuring the change in length of a material during all stages of the applied heat treatment. This method is useful for identifying phase transformations, since γ-iron (with an FCC structure) and α-iron (with a BCC structure) have different crystal structures, therefore different volumes per unit cell. This high-precision system is capable of detecting dimensional variations with a 50-nm resolution and a temperature control of 0.05 °C. Electrically conductive specimens are heated inductively using a water-cooled copper coil. Cooling is achieved through the direct introduction of inert gases, such as helium or argon, via the copper coil. Both heating and cooling processes are fully program-controlled, with real-time temperature monitoring performed using a k-type thermocouple spot-welded to the specimen surface. To minimize oxidation effects at elevated temperatures, a partial vacuum (5×10^{-4} mbar) is established during heating and austenitisation. Dimensional changes are recorded by means of two push rods, one stationary and the other linked to a linear variable differential transducer between which the specimen is positioned. Depending on the testing temperature, the push rods are fabricated from fused silica (below 1100 °C) or alumina (above 1100 °C).

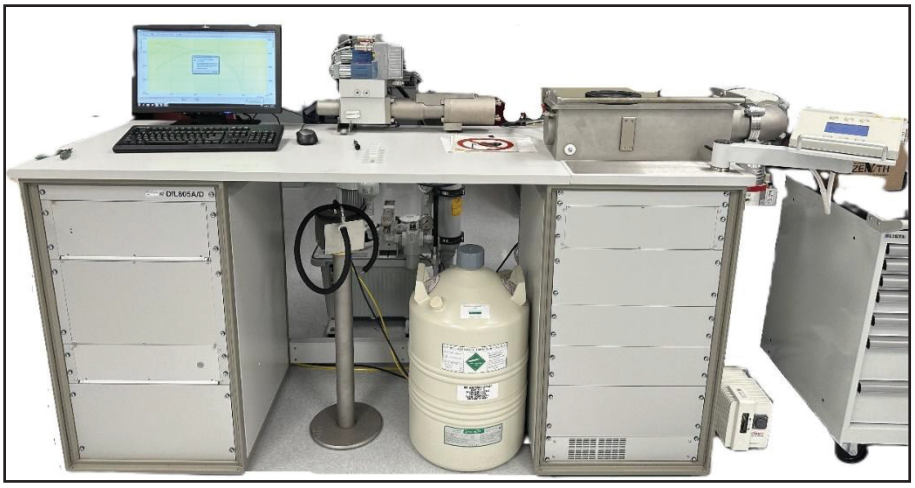

Figure 2-5 Dilatometer DIL805 A/D Taken from TA Instruments

The standard sample geometry utilized is a cylindrical specimen measuring 4 mm in diameter and 10 mm in length, Figure 2-6 presents the assembled configuration of the specimen.

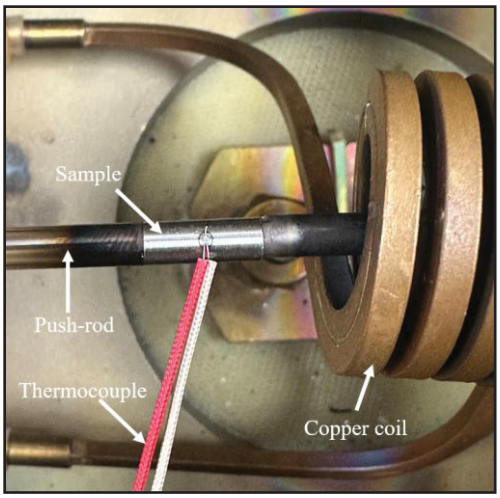

Figure 2-6 Sample and thermocouple assembling between dilatometry push-rods

2.2.1 Heat treatments and phase transformations

All heat-treatment cycles in this study were performed using the mentioned dilatometer to address the following sub-objectives: (1) investigating bainitic phase transformation as a

function of the PAGS during slow continuous cooling, (2) investigating isothermal bainitic phase transformation at different austempering temperatures, and (3) analyzing the effect of tempering time in the bainitic microstructure have been done with dilatometry technique. Details of each heat-treatment procedure are provided in the following sections.

2.2.1.1 First sub-objective

To investigate the effect of bainitic phase transformation as a function of the prior austenite grain size (PAGS), three grain sizes were selected based on measurements obtained from an actual industrial steel block, sampled from the surface to the core. Different holding times were used to reproduce the same PAGS values observed in the industrial case while maintaining a constant austenitization temperature. The final cooling rate applied in this work was selected according to experimental and simulation data reported by (Bouissa et al., 2021).

In order to obtain the desired PAGS values, specimens were austenitized at 1150 °C for 10 s, 10 min, and 35 min under vacuum conditions, using a heating rate of 1 °C/s. The austenitization temperature was kept constant to maximize the similarity among the three sample conditions with respect to temperature-dependent phenomena, such as the diffusion rates of alloying elements. After austenitization, each sample was cooled to 950 °C, slightly above the Ar_3 temperature, and held for 2 minutes to ensure temperature homogenization, then cooled to room temperature at a rate of 0.05 °C/s, as schematically shown in Figure 2-7.

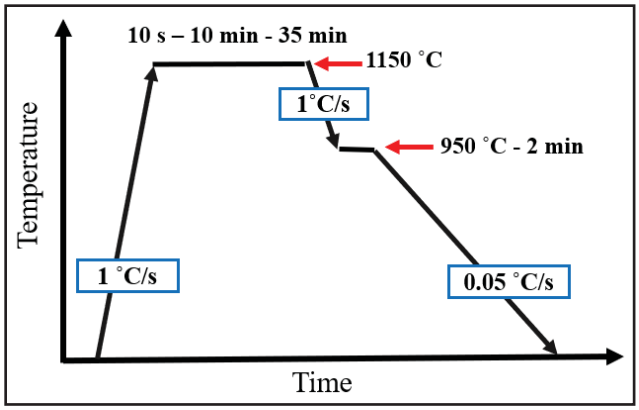

Figure 2-7 Slow continuous cooling heat treatment cycles to room temperature for three different PAGS values

In addition to the test plan illustrated in Figure 2-7, three types of complementary dilatometry experiments were performed. Since the results extracted from Figure 2-7 experiments, as it will be shown later in this manuscript, revealed two-stage phase transformations, the subsequent tests were specifically designed to characterize these transformation stages, as presented in Figure 2-8. In these experiments, the specimens were first cooled at a rate of 0.05 °C/s until the completion of the first transformation stage, followed by rapid cooling at 10 °C/s.

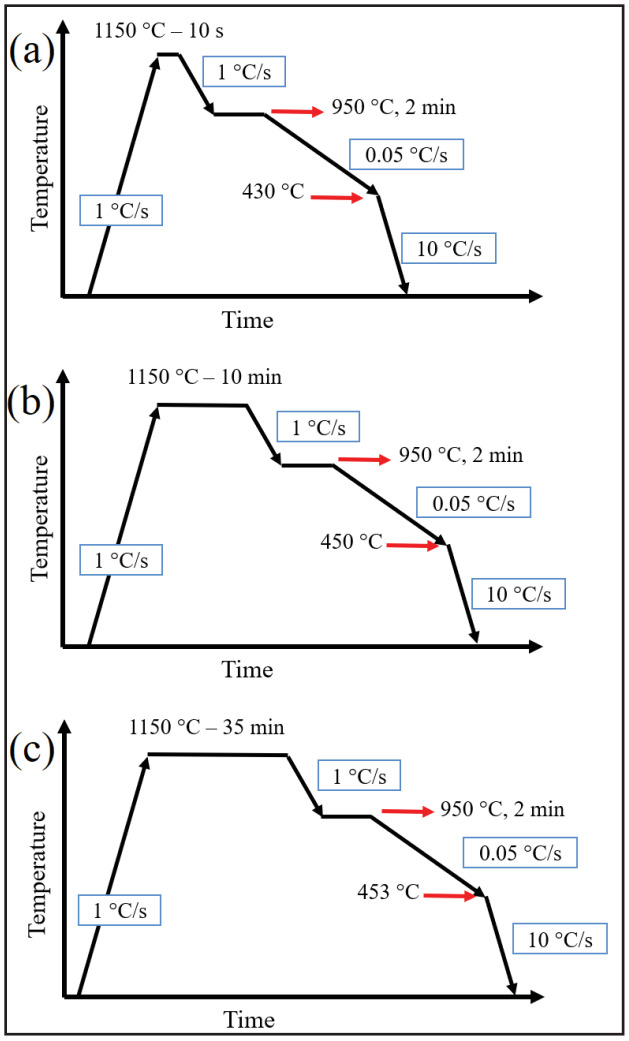

Figure 2-8 Schematic of the heat treatment designed to characterize the first stage of phase transformation

Since martensite forms during the second stage of phase transformation, the effects of different cooling rates and varying PAGS on the martensite start temperature (Ms) of the steel were investigated to characterize the transformations at different stages, as shown in Figure 2-9a and b, respectively.

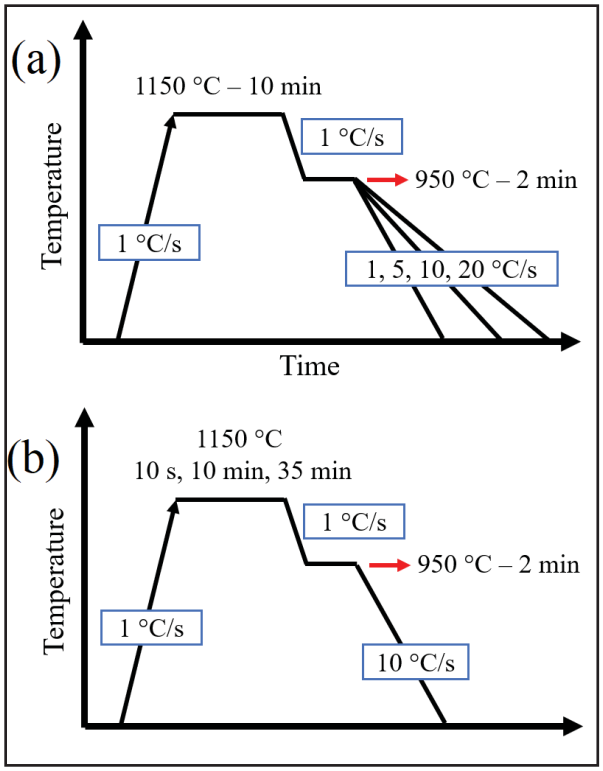

Figure 2-9 Schematic of the heat-treatment procedures designed to characterize the effect of (a) different cooling rates and (b) varying PAGS on the Ms temperature of the studied steel

2.2.1.2 Second sub-objective

In the second sub-objective, the effect of different austempering temperatures on the microstructure and mechanical properties of the products was investigated. Figure 2-10 shows the schematic of the applied heat treatment cycle. Initially, the specimens were heated at a rate of 5 ˚C/s to austenitization temperature at 900 ˚C and held for 15 min under vacuum. The austenitization temperature of 900 °C was selected based on industrial processing conditions. The samples were then cooled with a rate of 2 ˚C/s to different temperatures ranging from 380 ˚C to 450 ˚C, followed by 3 hours holding. The selected temperatures were based on the continuous cooling transformation (CCT) diagram of the steel (Hurel, 2022), chosen above the martensite start temperature, while the austempering time was determined based on the real

industrial scenario. In the final step, the samples were cooled to room temperature at a cooling rate of 10 ˚C/s.

In Chapter six, the same heat treatment was applied, with the only difference being the final cooling rate to room temperature, which was 0.05 °C/s. This heat treatment was designed to more closely simulate industrial conditions and to evaluate the effect of the final cooling rate after isothermal bainitic phase transformation on the resulting microstructure and hardness.

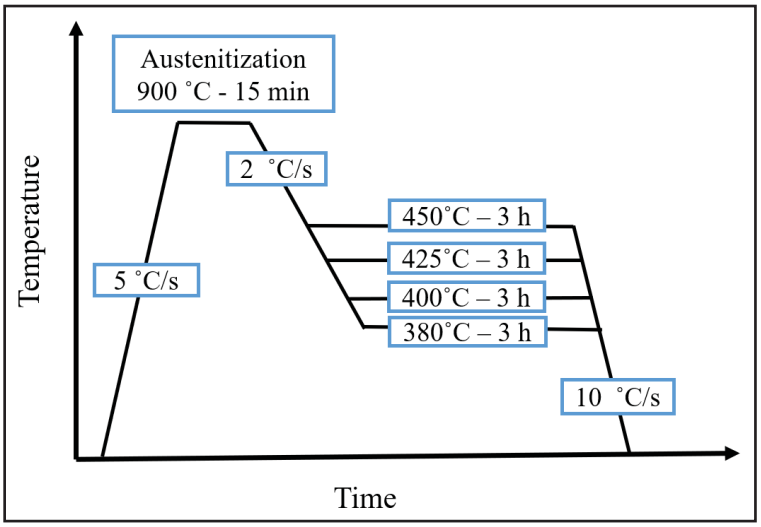

Figure 2-10 Heat treatment cycle applied to the studied steel

2.2.1.3 Third sub-objective

To evaluate the influence of the time to attaining the target tempering temperature on bainitic microstructural evolution, the following dilatometry heat-treatment cycle was applied. The specimens were austenitized at 900 °C for 15 min, cooled to room temperature at 0.05 °C/s to achieve a bainitic microstructure (including bainitic ferrite, RA, carbides, and M-A zones) similar to the center of a large steel block, and subsequently reheated at 0.2 °C/s to 620 °C. Two tempering durations were applied, 30 min and 14 h, followed by cooling to room

temperature at 1 °C/s (Figure 2-11). This experimental design replicates the effect of prolonged heating times required to achieve temperature uniformity between the surface and the core of thick steel blocks.

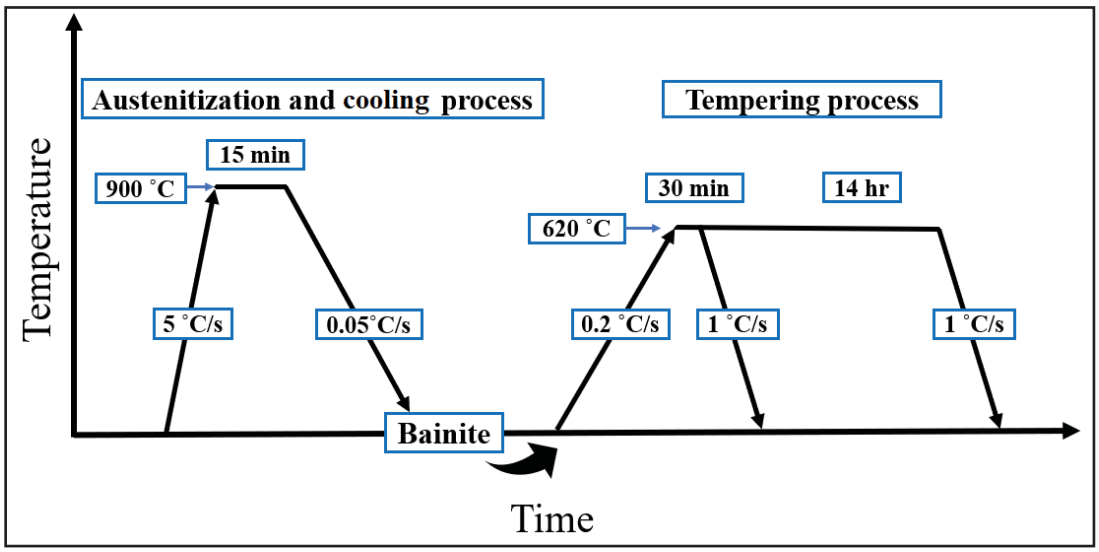

Figure 2-11 Schematic of the applied heat treatment cycle

2.3 Sample Preparation

For microstructural characterization, the specimens were sectioned transversely, and the central region of the specimen was examined. Subsequently, after mounting, surface preparation was performed through sequential polishing with Silicon carbide (SiC) abrasive papers, beginning with coarse grit (120) to remove surface irregularities and progressing to finer grit (1200) to obtain a smooth and uniform finish. At each grit transition, the specimens were rotated 90° to eliminate scratches from the preceding stage. Final polishing was conducted in two separate steps; first using 3 µm SiC suspension, followed by polishing with a 1 µm SiC suspension, each applied on polishing cloths for a duration of 5-10 minutes.

Following mechanical polishing, specimens prepared for microstructural analysis were etched with 3-5% Nital solution for 5–15 seconds, whereas specimens used for X-ray diffraction (XRD) analysis and hardness testing were utilized in their polished state without etching.

For Electron Backscatter Diffraction analysis, specimens underwent additional preparation: after mechanical polishing, a fine polish was performed using a 0.05 µm colloidal silica suspension on a Buehler VibroMet polisher (Figure 2-12a), and the process was finalized with ion milling using a Hitachi IM4000Plus system (Figure 2-12b).

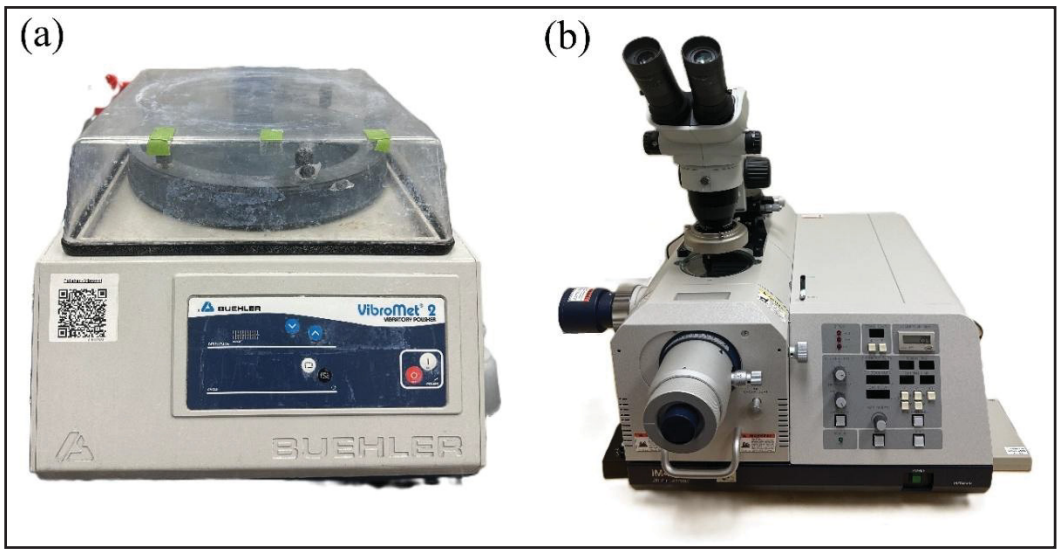

Figure 2-12 Sample preparation equipment: (a) Buehler VibroMet polisher and (b) Hitachi IM4000Plus ion milling system

2.4 Microstructure Characterization

Microstructure characterization was carried out using several complementary techniques, including optical and electron microscopy for prior-austenite grain size measurement and detailed microstructural analysis, together with X-ray diffraction for determining the retained austenite volume fraction.

The average prior austenite grain size was revealed using the thermal etching technique (Vander Voort, 1999). In this technique, a dilatometry sample was polished longitudinally to create 1 mm wide surface, finishing with 3 μm diamond paste. The samples were subjected to the same austenitization process as described (1150 ºC – 10 s, 10 min, and 35 min), the whole process in vacuum to avoid oxidation of the polished surface, and finally cooled down to room temperature at 1 °C/s. After cooling to room temperature, the prior austenite grains became clearly distinguishable the polished surface. In this technic, to minimize the total thermodynamic energy, atoms migrate away from the high-energy grain boundary region through surface diffusion or evaporation-condensation, leading to the formation of microscopic V-shaped grooves that provide contrast under optical or scanning electron microscopy (SEM). The micrographs were acquired using an Olympus LEXT4100 laser confocal microscope (Shinjuku City, Japan), which allows image stitching and merging over large surface areas (Figure 2-13(a)).

For microstructural detailed analysis of the retained austenite, fresh martensite, and bainitic characteristics, scanning electron microscopy (SEM) was used. Two high-resolution instruments were employed: the Hitachi TM3000 SEM and the Hitachi SU8230 FE-SEM (Hitachi High-Tech Canada, Toronto, ON, Canada), both equipped with energy-dispersive spectroscopy (EDS) for elemental mapping (Figure 2-13(b-c)). To further resolve the microstructural features, electron backscatter diffraction (EBSD) analysis was conducted.

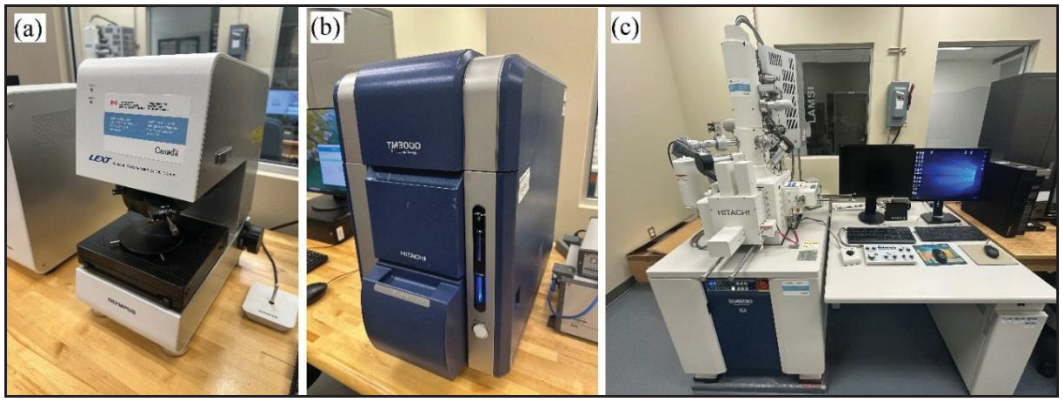

Figure 2-13 Characterization equipment: (a) Olympus LEXT4100 laser confocal microscope, (b) Scanning electron microscopy TM3000, and (c) Scanning electron microscopy SU8230

The retained austenite volume fraction was determined by XRD using a PANalytical X'Pert Pro diffractometer with Co Kα radiation (λ = 1.78896 Å), operated at 45 kV and 40 mA (Figure 2-14). Diffraction patterns were recorded over a 2θ range of 40°–130° with a step size of 0.0083° and a counting time of 150 s per step, ensuring high-resolution structural characterization. Quantification of RA was performed by Rietveld refinement using HighScore software (version 4.2, Bruker AXS). Special care was taken to avoid and remove any deformed surface layer during sample preparation for XRD measurements, therefore, several etching and polishing cycles were applied to remove the deformed surface layer (Morawiec et al., 2022). To quantify the retained austenite (RA) volume fraction, two methods were used; modified Miller's method reported in ASTM E975 standard applied in chapter four (Committee, 2013) and Rietveld method (Young, 1993), as applied in chapter six. To calculate the carbon content of retained austenite, the equation provided in Reference (Cheng et al., 1990), together with Bragg's law (Bragg William Henry & Lawrence, 1913), was used.

Figure 2-14 X'Pert3 MRD PANalytical X-ray diffraction machine

2.5 Hardness Measurement

To evaluate the mechanical properties of the microstructure after different heat treatments, both, microhardness and nanohardness measurements were performed. Vickers hardness (HV) was measured under loads of 0.3 and 0.5 kgf using a Duramin-40 semi-automatic micro tester (Struers) (Figure 2-15a). On average, 10 indents were applied to the polished specimen surface, and the reported values represent the mean of these measurements.

For phase-specific mechanical properties, nanohardness testing was conducted using two instruments: a Hysitron PI88 SEM PicoIndenter (Figure 2-15b) installed in a Hitachi S3600-N SEM for precise indentation positioning, and an Anton Paar NHT³ instrument (Figure 2-15c). The Hysitron PI88 was used to perform in situ nanohardness measurements within a SEM in order to determine the hardness of specific phases. In both cases, a Berkovich indenter tip was employed, and the equipment was calibrated using a fused silica standard. For each microstructural feature, three indents were applied to obtain representative values.

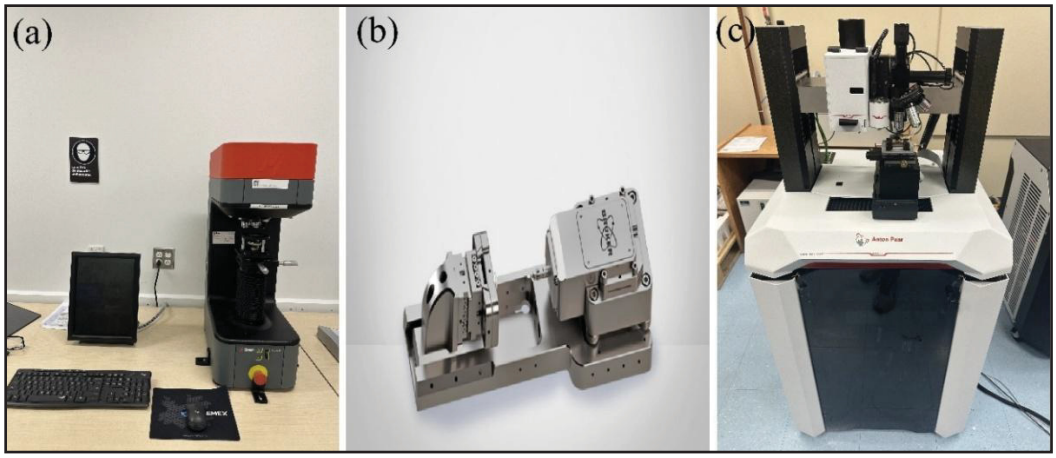

Figure 2-15 Hardness machines, (a) Duramin-40 semi-automatic micro tester Struers, (b) Hysitron PI88 SEM PicoIndenter nanoindenter, and (c) Anton Paar NHT³ nanoindenter

Tests were conducted under load-control with a loading-unloading rate of 10 mN/s and a dwell time of 2 s. After initial calibration using a standard SiC reference sample, multiple trials were performed at loads ranging from 20 mN to 100 mN to evaluate result repeatability. Based on these trials, a constant load of 50 mN was selected. For reproducibility, a minimum of 5 indentations were made in each analyzed region (bainitic and martensitic). Figure 2-16 illustrates a schematic representation of the load–penetration depth curve obtained from a nanoindentation experiment. The maximum displacement, denoted as *hm*, reflects the combined effect of elastic and plastic deformation. The depth where the load reduces to zero during unloading is termed the final indentation depth *hp*, representing the permanent plastic deformation. The contact stiffness S, determined at the initial stage of unloading, is calculated as the slope of the unloading curve, given by S = *dF/dh*. The parameter *hr* indicates the contact depth used to determine the contact area (*A*), which is essential for calculating the material's hardness (Mazaheri et al., 2015). The values for *hr* and hardness were determined using the standard Oliver and Pharr method (Oliver & Pharr, 1992). The contact area A can be expressed as equation (2-1)) (Lei et al., 2022):

$$A = 24.56h_r^2 \tag{2-1}$$

According to the Oliver and Pharr method; h_r can be calculated using to following equation (Mazaheri et al., 2015):

$$h_r = h_m - \varepsilon\left(\frac{F_m}{s}\right) \tag{2-2}$$

where ε is a constant which is dependent on indenter shape (ε = 0.75). The hardness is expressed as follows (Lei et al., 2022):

$$H = \frac{P}{A} \tag{2-3}$$

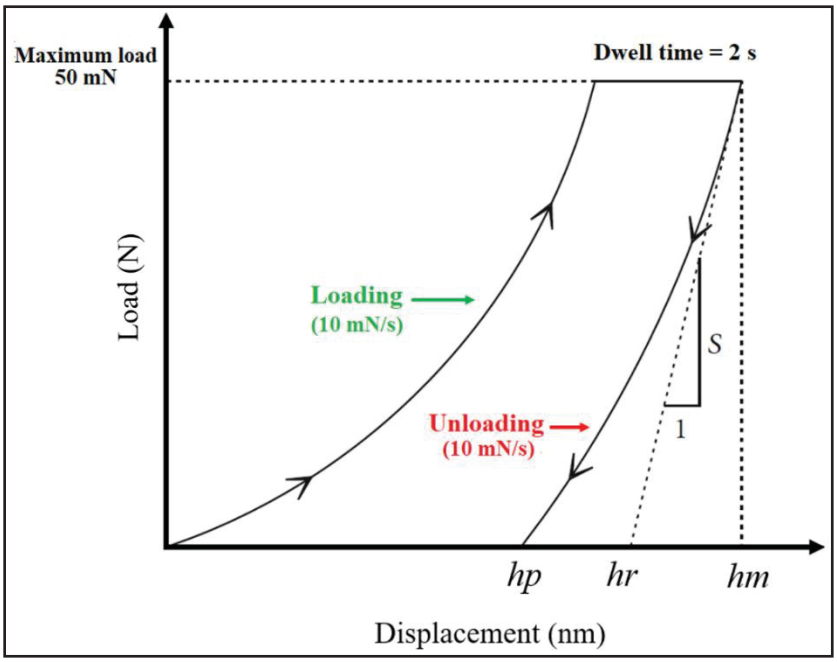

Figure 2-16 Schematic of the applied nanoindentation load–displacement cycle

Furthermore, nanoindentation experiments were carried out in chapter five to compare the local hardness of bainitic ferrite, aggregated carbide zones, and fresh martensite, at ambient temperature using an Anton Paar NHT³ instrument. A Berkovich indenter was employed for the measurements. The tests were performed under load control, applying a loading and unloading rate of 25 mN/min and 10 mN/min, respectively, and with a holding time of 10 seconds at maximum load of 20 mN. The hardness values were calculated following the standard Oliver and Pharr approach (Oliver & Pharr, 1992).

2.6 Thermodynamic Simulations

To investigate the stability of carbides and other phases in the steel, thermodynamic calculations were performed using Thermo-Calc (version 2021a) software. In this software, the calculations are based on Gibbs free energy (ΔG) minimization. Temperature, composition, and pressure are used as input parameters to determine the equilibrium state of the system. The software calculates the stable phases by minimizing the Gibbs free energy, allowing the identification of temperature ranges where specific carbides (such as cementite or alloy carbides) and matrix phases (e.g., ferrite, austenite, bainite) are thermodynamically favored. The results of these simulations can be visualized in phase fraction vs. temperature plots, which provide a clear representation of the stability and evolution of phases and carbides during cooling. Such plots can also be correlated with experimental observations from SEM and microstructural analyses and carbide precipitation.

2.7 Numerical simulation of Temperature Distribution

To investigate the temperature distribution during tempering of a large steel block in the third sub-objective, numerical simulations were performed. The transient thermal behavior of the block was modeled in ANSYS by solving the three-dimensional heat conduction equation to predict the temperature distribution during the heating stage of the tempering process. All simulations were carried out by Sajad Mirzaei. Further details of the finite element method (FEM) framework, including the model, governing equations, and meshing strategy, are presented in Section 5.3.

The block, with dimensions of 3.5 m × 1.4 m × 0.81 m (corresponding to the actual size of an industrial block) and a mass of approximately 31 metric tons, initially at 23 °C, is exposed to a preheated furnace environment maintained at 620 °C. In the numerical simulations, the transient thermal behavior of the block was modeled by solving the three-dimensional heat conduction equation (ANSYS Inc., 2023 R2):

$$\rho c_p \frac{\partial T}{\partial t} = \nabla \cdot (k \nabla T) \tag{2-4}$$

Where ρ is the density (kg/m³), c_p is the specific heat capacity (J/(kg·K)), T is the temperature (°C), t is time (s), and k is the thermal conductivity (W/(m·K)). The primary objective is to determine the time required for the center of the block to reach the furnace temperature, assessing its thermal uniformity. The computational domain represents the steel block entirely. A poly-hexahedral mesh (ANSYS Inc., 2020), comprising 112,500 cells, was generated to ensure an optimal balance between computational efficiency and result accuracy. Mesh independence was verified by refining the mesh until further refinement caused negligible changes in the temperature distribution results, ensuring sufficient resolution for capturing thermal gradients (Mirzaei et al., 2024). The block's thermal properties, specific heat capacity, and thermal conductivity were modeled as temperature-dependent piecewise polynomial functions (Mirzaei et al., 2023). These functions were derived from JMatPro software(*JMatPro*), which calculates property values based on the block's material composition. This approach ensures realistic modeling of thermal behavior over the temperature range of interest. Following the final simulation, it was determined that approximately 14 hours were needed for the block to attain a completely uniform temperature, as shown in Figure 2-17.

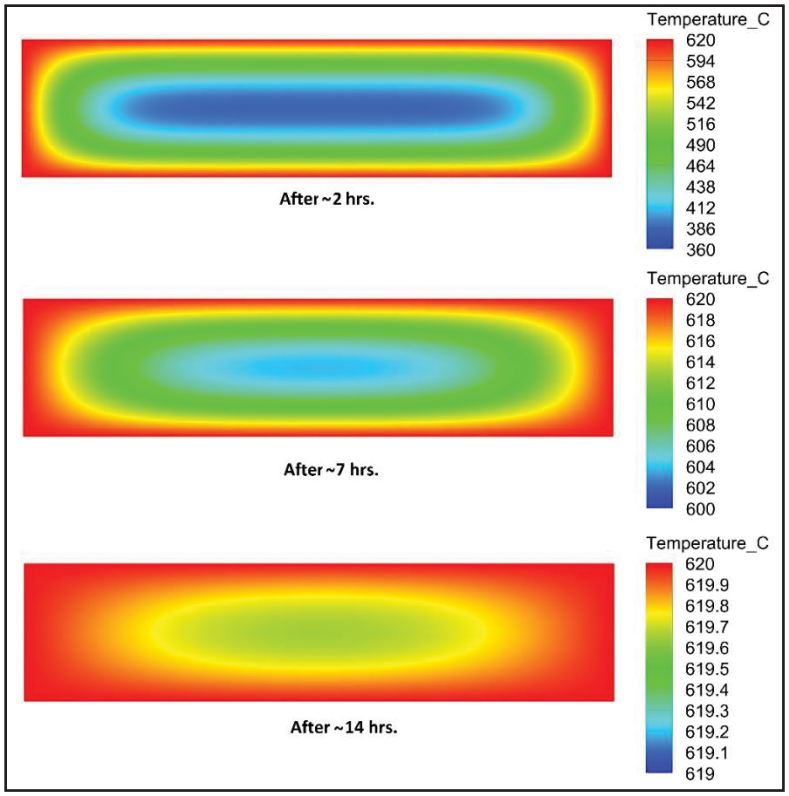

Figure 2-17 Temperature distribution contours at the central cross-section of the industrial-size steel block at 2, 7, and 14 hours

2.8 Chapter Summary and Outlook

This chapter describes the experimental methods adopted to support the objectives of this research. It provides detailed descriptions of sample preparation particularly the sampling procedure from a large industrial steel block as well as the equipment, characterization techniques, and thermodynamic and numerical simulations employed. The methodologies presented enable a systematic investigation of phase transformations and microstructural features, forming the foundation for the results and discussion presented in the subsequent chapter. Additionally, in the following chapters, the specific heat-treatment cycles, including temperatures, holding times, heating and cooling rates, and detailed dilatometry analyses, are presented and discussed.

CHAPTER 3

Multi-step phase transformations during slow continuous cooling in steel with large prior austenite grain size

Ehsan Tolouei[a], Simin Dourandish[b], Carlos Garcia-Mateo[c], and Mohammad Jahazi[a]*

[a] Department of Mechanical Engineering, École de Technologie supérieure (ETS), 1100 Notre-Dame St. W, Montreal, QC, H3C 1K3, Canada

[b] Finkl Steel-Sorel, 100 McCarthy, Saint-Joseph-de-Sorel, QC, J3R 3M8, Canada

[c] Department of Physical Metallurgy, National center for metallurgical research (CENIM-CSIC), Materalia Research Group, Avenida Gregorio Del Amo, 8, Madrid, 28040, Spain

* Corresponding author: Mohammad.Jahazi@etsmtl.ca, Tel: +1-514-396-8974, Fax: +1-514-396-8800

Published in Journal of Materials Research and Technology

3.1 Abstract

The influence of different prior austenite grain sizes (PAGS) on phase transformation during slow continuous cooling was investigated by high-resolution dilatometry in a medium-carbon low-alloy steel. The selection of different PAGS values was motivated by an industrial case study of a large steel block, in which significant grain size variation occurs between the center and the surface. PAGS of 101 μm, 202 and 304 μm, were achieved through austenitization at 1150 ˚C for 10 seconds, 10 and 35 minutes followed by continuous cooling with a rate of 0.05 ˚C/s to room temperature, representative of the cooling of the large size steel block. Analysis of the dilatometry results combined with microstructure investigation using scanning electron microscopy revealed a two-stage phase transformation process. The first one occurred at high temperature and led to the formation of granular bainite and plate-like bainite. The second stage proceeded slowly over an extended duration, leading to the tempering of the bainite formed in the first stage and the formation of martensite from the residual austenite, accompanied by the auto-tempering. X-ray diffraction analysis indicated that, an increase in

PAGS led to a rise in the volume fraction of retained austenite from 10% to 24.4%. Average microhardness values remained very similar despite variations in PAGS and volume fraction of phases. In contrast, nanohardness measurements revealed that bainitic ferrite in granular bainite exhibits the lowest hardness, whereas plate-like morphology shows intermediate hardness, and the (M-A) constituents display the highest hardness.

Keywords: Prior austenite grain size; granular bainite; plate-like bainite; retained austenite; auto-tempering; multi-step phase transformation

3.2 Introduction

In recent years, the demand for large steel blocks, used as mold for the production of large size automotive components, has significantly increased (Tolouei, Hurel, et al., 2025). These blocks can reach thickness and widths of over a meter, with lengths of more than 2 meters. These large blocks are produced using ingot casting, open-die forging, and a heat treatment process that includes quenching followed by tempering (Tolouei et al., 2024). Due to the significant thickness of these blocks, their microstructure predominantly consists of bainite, generated during the slow cooling process, when quenched in a water pool.

Bainitic steels have garnered significant attention due to their outstanding mechanical properties, such as high strength and toughness (Y. Li et al., 2016); however, diverse bainite morphologies, with different mechanical properties, could be produced as a function of alloy composition or microstructure conditioning before bainitic transformation (Bramfitt & Speer, 1990). The latter initiates by the nucleation and growth of carbon-supersaturated bainitic ferrite plates (H. K. D. H. Bhadeshia, 2001), accompanied by carbon partitioning into surrounding austenite. Progressive carbon enrichment reduces the thermodynamic driving force until the T_0 condition is reached, terminating the transformation and resulting in carbon-enriched residual austenite (H. K. D. H. Bhadeshia, 2001). Upon cooling to room temperature, the stability of the residual austenite depends on its carbon content: insufficient carbon leads to partial or complete transformation to martensite, forming martensite–austenite (M–A) constituents, whereas sufficient carbon results in stable retained austenite (RA) (Garcia-Mateo et al., 2012).

Since bainite primary nucleation sites are the austenite (γ) grain boundaries, austenite conditioning, particularly the prior austenite grain size (PAGS), significantly influences phase transformation behavior and final microstructures (Hasan et al., 2020; Ravi et al., 2016; Yamamoto et al., 1995). The combination of high temperature, often above 1250 °C, and variations in strain and strain rate distribution during forging results in non-uniform austenite grain sizes from the surface to the center of the large size block (Dhondapure et al., 2024). Therefore, the bainitic phase transformation throughout the block's thickness will vary in terms of kinetics and bainite type due to differences in PAGS. Consequently, understanding how the PAGS influences the bainitic transformation and the final microstructure requires a thorough analysis (Lee et al., 2008; Zhu et al., 2013).

A critical examination of the existing literature reveals certain gaps in understanding the influence of PAGS on bainitic phase transformation. Notably, the investigations on PAGS effects have primarily focused on a limited size range lower than 100 μm (Hu et al., 2014; Lan et al., 2017; Ueji et al., 2021; Zhu et al., 2013), leaving the impact of extra-large PAGS in bainitic phase transformation largely unexplored. Ueji et al. (Ueji et al., 2021) reported that refining PAGS from 50 to 11 μm accelerated the bainitic phase transformation, under isothermal transformation conditions, due to increasing the density of nucleation sites, while no significant difference was observed in the transformed phase product. Although some studies have investigated the effect of PAGS on the kinetics of bainitic phase transformation, the results remain inconsistent; however, this aspect is beyond the scope of the present study (Hu et al., 2014; Matsuzaki & Bhadeshia, 1999; Sun et al., 2020). Chen et al. (Chen et al., 2022), reported that austenitization at different temperatures, resulting in varying PAGS, alters the bainite morphology from granular to lath-type. Ueji et al. (Ueji et al., 2021) noted a reduction in RA volume fraction with refined PAGS. Similar findings were reported by Hasan et al. (Hasan et al., 2020), linking increased PAGS to a higher volume fraction of bainite during phase transformation, explaining that greater bainite formation led to increased carbon diffusion to the remaining austenite, leaving a larger fraction of RA in isothermal bainitic phase transformation. Conversely, Mandal et al. (Mandal et al., 2022) found that in medium-carbon high-silicon steels, smaller PAGS led to a higher RA volume fraction and increased carbon

content. Overall, the literature suggests that austenite grain size plays a critical role in determining the bainitic phase transformation.

Another interesting and less explored facet of bainitic phase transformation is the occurrence of multi-stage phase transformations, a distinctive feature highlighted in this paper. While the occurrence of multi-stage phase transformations has been reported in the context of pearlite phase transformation (T. Liu et al., 2018; Mateusz Morawiec et al., 2020), very little data is available on this topic in the case of bainitic transformation. Bao et al. (Bao & Wang, 2021) reported a two-stage phase transformation in continuous cooling bainitic phase transformation, revealing a high-volume fraction of bainitic formation in the initial stages and a low volume fraction of bainitic ferrite formation in the final stage of the phase transformation. However, multi-stage phase transformation and the influences of austenite condition, such as PAGS or process parameters such as cooling rate have not been investigated. Finally, it must be noted that the majority of research efforts reported above has been concentrated on isothermal bainitic phase transformations, despite the fact that in real world operations, a significant portion of bainitic steels is produced during continuous cooling of the parts.

The present works aims to address the above gaps in the literature by investigating the influence of PAGS on bainitic phase transformation and the resultant microstructure, specifically during the slow continuous cooling process, representative of the cooling in different regions of large size forged blocks, and characterization of each stage of phase transformation.

3.3 Materials and Methods

The detailed methodology employed in this chapter is described in Chapter Two.

3.4 Results

3.4.1 Different PAGS

Figure 3-1(a-c) shows the prior austenite grain at 1150 °C after different holding times and Figure 3-1d shows the histogram of the measured grain size distribution. The average grain sizes are 101 ± 37 µm, 202 ± 74 µm, and 304 ± 120 µm for holding times of 10 s, 10 min, and 35 min, respectively. The results show that as the holding time increases, the average PAGS increases and the histogram exhibits a wider grain-size distribution.

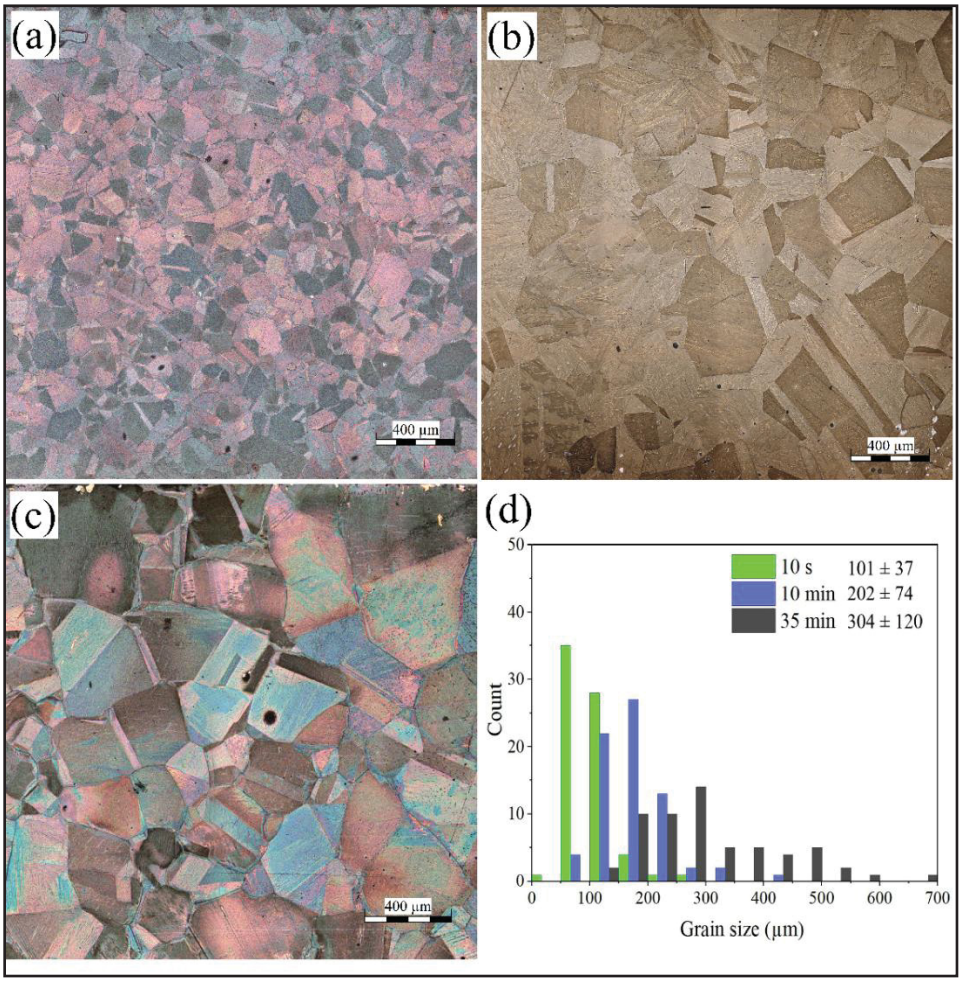

Figure 3-1 Optical micrographs display the prior austenite grain boundaries at 1150 °C for different holding times: 10 s (a), 10 min (b), 35 min (c), and the histogram of grain size distribution (d)

3.4.2 Effect of PAGS and cooling rate on Ms temperature

In order to characterize the bainitic and martensitic phase transformations during slow cooling, the influence of different PAGS and cooling rates on the Ms temperature was investigated as two effective factors (Babasafari et al., 2020; Celada-Casero et al., 2019). Figure 3-2a shows that the Ms temperatures, determined via the tangent method from dilatometry curves, are 395, 385, 390, and 380 °C for cooling rates of 1, 5, 10, and 20 °C/s, respectively (see Figure 2-9a for the corresponding test design). A minor trend suggesting that the Ms temperature decreases with increasing cooling rate; however, the differences are negligible, with the maximum variation observed being approximately 10–15 °C. It appears that, the sensitivity of the Ms temperature to alloying elements, especially carbon, is greater than its sensitivity to cooling rate (Liu et al., 2001). The findings are also in agreement with those of Bibby et al. (M.J. Bibby & Parr, 1964), Zhao et al. (Zhao & Notis, 1995), and Liu et al. (Liu J. H. et al., 2021) who reported that the Ms temperature changes very little with cooling rate, as long as it is sufficiently rapid to avoid diffusion-controlled transformations.

Figure 3-2b presents dilatometry results illustrating the effect of holding time (i.e., different PAGS values) on Ms (see Figure 2-9b for the corresponding test design). All Ms temperatures fall within 380–390 °C, indicating that austenite grain size variations in this range have negligible influence on the Ms temperature. According to van Bohemen et al. (van Bohemen & Morsdorf, 2017), this effect is highly grain-size-dependent for fine austenite grains (<10 - 28 μm), but becomes negligible for coarser grains (100 - 600 μm), where it would cause only about a 3 °C change in Ms.

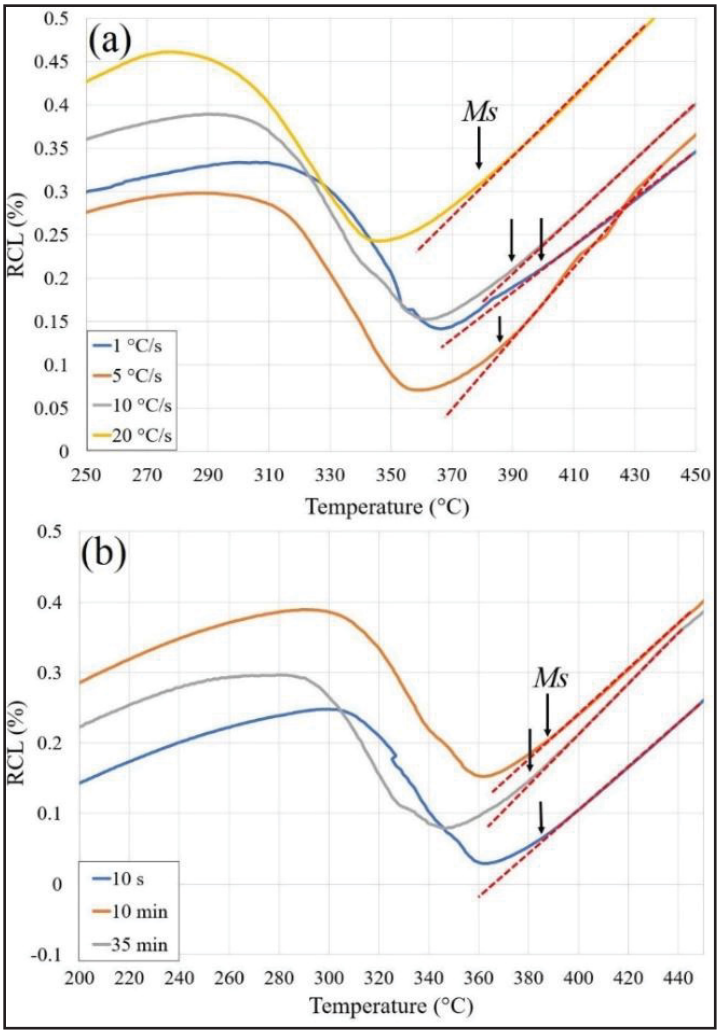

Figure 3-2 Dilatometry results showing (a) the effect of different cooling rates and (b) the effect of different PAGS on the Ms temperature

Figure 3-3(a-c) show the as-quenched lath martensitic microstructure corresponding to the conditions presented in Figure 2-9b. Figure 3-3d, which is a higher-magnification image of the region marked in Figure 3-3c, reveals fine carbides distributed within martensitic laths, indicating the occurrence of auto-tempering during cooling after martensite formation. As reported by Krauss, (Krauss, 1999) in steels with relatively high Ms temperatures and low carbon content, dispersed cementite precipitation can take place within the martensite (Krauss, 1999). This precipitation is generally delayed or even suppressed in steels with higher Si

content; however, the low Si content in the investigated steel, does not hinder cementite formation (Kozeschnik & Bhadeshia, 2008).

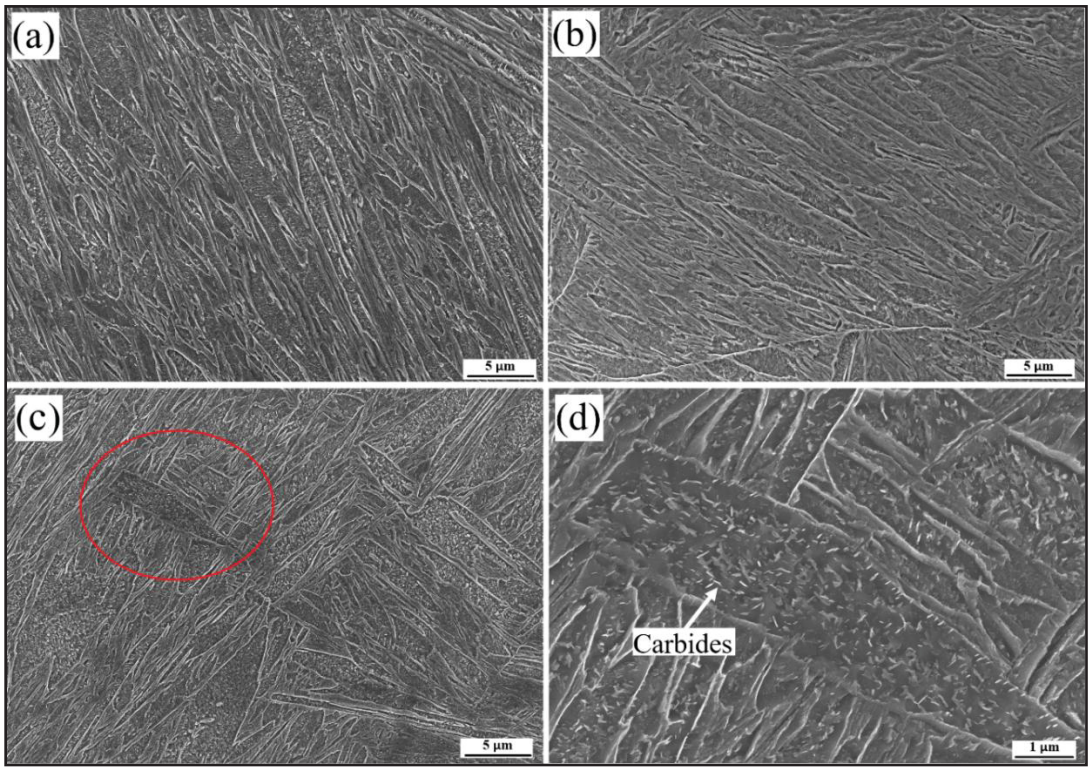

Figure 3-3 SEM images of the martensitic microstructure cooled at a rate of 10 °C/s after different austenitization holding times: (a) 10 s, (b) 10 min, (c) 35 min, and (d) a higher-magnification image of the red-circle region in (c), showing the auto-tempered carbides distribution within the martensitic laths

3.4.3 Slow Continuous Cooling

In this section, tests performed under slow cooling rates, Figure 2-7, representative of those experienced in large industrial blocks, were investigated. Figure 3-4 illustrates the relative change in length (RCL) as a function of temperature during cooling for the three investigated PAGS. As indicated by the double-headed arrow for the 10 s case, the phase transformation in all three samples occurred in two major stages, identified by changes in the slopes of the RCL curves. The onset and completion of each phase transformation stage under the three conditions are marked by red arrows in Figure 3-4. In the following paragraphs a comprehensive analysis

is conducted using different techniques in order to identify the different events taking place at each stage.

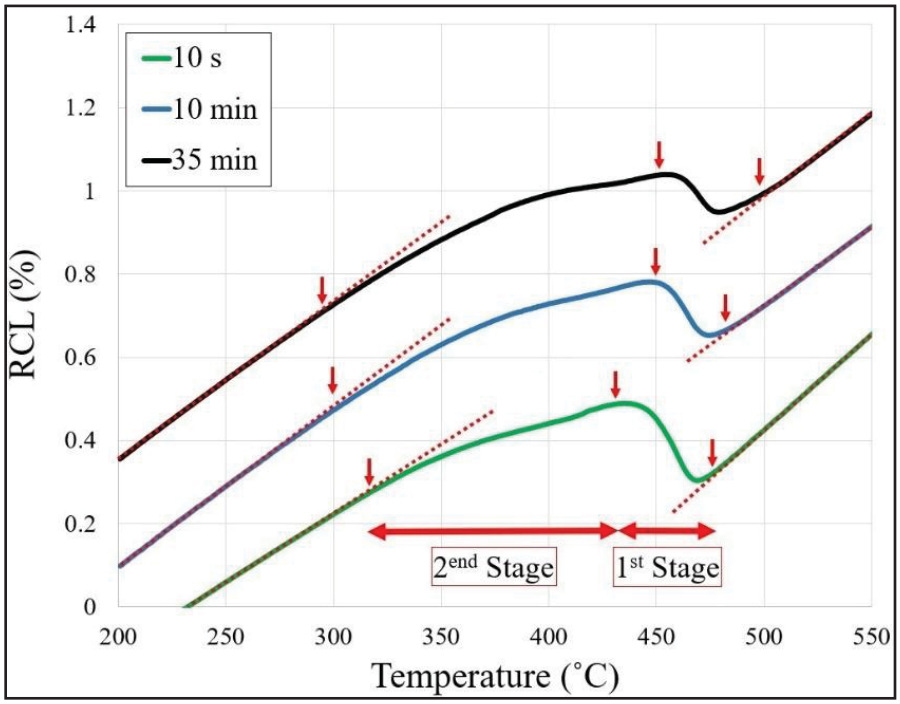

Figure 3-4 Variation of RCL with temperature during continuous cooling of the samples austenitized at 1150 °C for different holding time 10 seconds, 10 and 35 minutes. Double-headed arrows illustration for the 1st and 2nd stage of transformation. The start and end of each stage are indicated by red arrows

3.4.4 Phase transformation (first stage)

The first-stage transformation detected in the dilatometry curves appears as an expansion in the relative change in length (RCL), arising from the larger atomic volume of ferrite relative to austenite (Christien et al., 2013). The magnitude of this expansion correlates directly with the volume fraction of the newly formed phase, enabling semi-quantitative assessment of transformation progress. According to the results in section 3.2, the Ms temperature lies

between 380 and 395 °C. However, the onset of the first-stage transformation occurs between approximately 470 and 500 °C (Figure 3-4), significantly above the Ms range. This temperature mismatch eliminates martensite formation as the cause of the observed expansion.

These observations identify the first-stage transformation as bainite formation. The bainite start (Bs) temperatures, determined by the tangent method, increase systematically with austenitization time: 472 °C, 483 °C, and 494 °C for the samples held at 1150 °C for 10 s, 10 min, and 35 min, respectively. Concurrently, the first-stage expansion magnitude decreases from 0.18% to 0.12% and 0.09% with increasing prior austenite grain size (PAGS). This inverse relationship arises because coarser PAGS reduces grain boundary area the primary nucleation sites for bainitic ferrite thereby, suppressing the bainite fraction formed during continuous cooling and leaving more austenite available for the subsequent martensitic transformation.

Characterization of bainite

To characterize the first phase transformation product, a dedicated test was designed, (see Figure 2-8). The treatment was interrupted at the end of the first stage, 430, 450 and 453 °C for the 10 s, 10 min, and 35 min treatments respectively, with all samples quenched to room temperature at 10 °C/s. The dilatometry curves (Figure 3-5) reveal multiple martensitic transformations from residual austenite during quenching, indicating compositional heterogeneity within the residual austenite following bainitic transformation, despite anticipated local carbon enrichment from bainite formation. However, the onset of the first transformation during the second cooling matches the Ms temperature of bulk austenite, as established by austenitization and quenching tests (Figure 3-2), suggesting that a significant fraction of residual austenite retains the original bulk carbon content rather than uniform enrichment.

Lower-temperature transformations arise from fresh martensite in carbon-enriched austenite regions, highlighting chemical inhomogeneity as the primary factor governing local stability. Quenching at 10 °C/s proved insufficient to fully suppress these transformations, as evidenced

by these "extra" events and auto-tempered carbides in the resulting martensite (Figure 3-3). This auto-tempering introduces additional microstructural features that influence phase stability and mechanical properties.

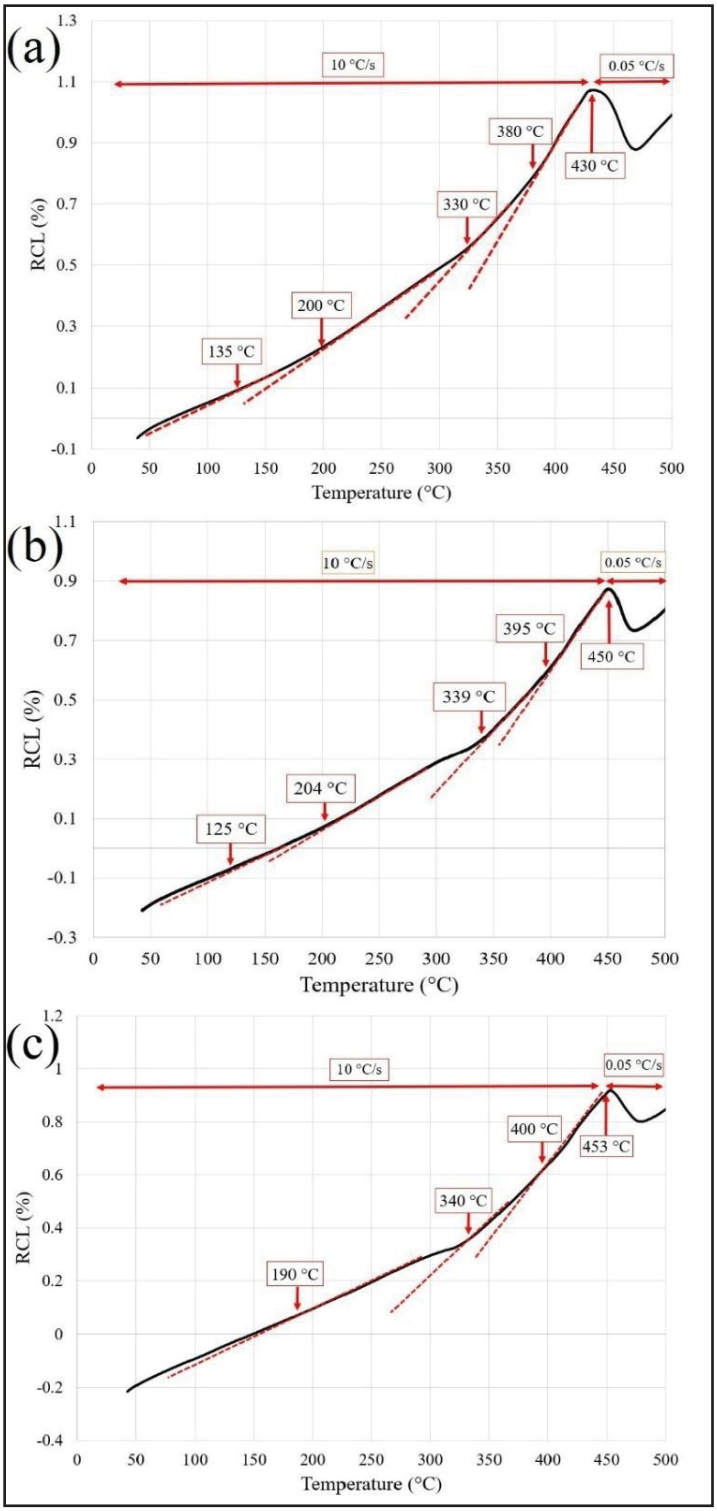

Figure 3-5 Relative change in length as a function of temperature for tests conducted at two different cooling rates, for three austenitization holding times: (a) 10 s, (b) 10 min, and (c) 35 min

As a representative case, the microstructure produced under the 1150 °C – 10 min two cooling rates condition (Figure 8b) was examined in detail, and the results are shown in Figure 3-6a-c. This microstructure reveals two distinct bainite morphologies, granular bainite (GB) and plate-like bainite (PB) alongside martensite (or martensite-austenite, M-A) constituents formed during the first transformation stage, plus additional martensitic regions generated from residual austenite during final cooling to room temperature.

Although GB is typically reported to form at higher temperatures than PB (Mazancová & Mazanec, 1997), both morphologies were observed to nucleate simultaneously during the initial transformation stage. GB, commonly observed in low-carbon steels subjected to continuous cooling, is characterized by irregular ferrite grains with non-uniform boundaries and dispersed carbon-enriched martensite-austenite (M-A) constituents (Jentner et al., 2023). Its formation under the present conditions can be attributed to the synergistic effects of enlarged prior austenite grain size (PAGS) and reduced cooling rates, which favor GB development over PB, in agreement with observations in commercial low-carbon bainitic steels (Caballero et al., 2012).

Rapid carbon partitioning at elevated temperatures during GB formation generates chemically heterogeneous austenite regions (Qiao et al., 2009), promoting subsequent PB nucleation and growth within carbon-enriched domains during cooling within the bainitic domain. This carbon inhomogeneity constitutes the primary mechanism underlying the concurrent formation of both morphologies and directly correlates with the multiple martensite start (Ms) temperatures evident during final cooling (Figure 3-5), reflecting the diverse carbon contents and stabilities of residual austenite populations. The yield strength of austenite (YS_γ), predominantly controlled by temperature and carbon concentration (Eres-Castellanos et al., 2020; Yang et al., 2019), represents a key factor governing bainite morphology. Nanoindentation measurements on these distinct morphologies, detailed in the subsequent section, provide further validation of these insights.

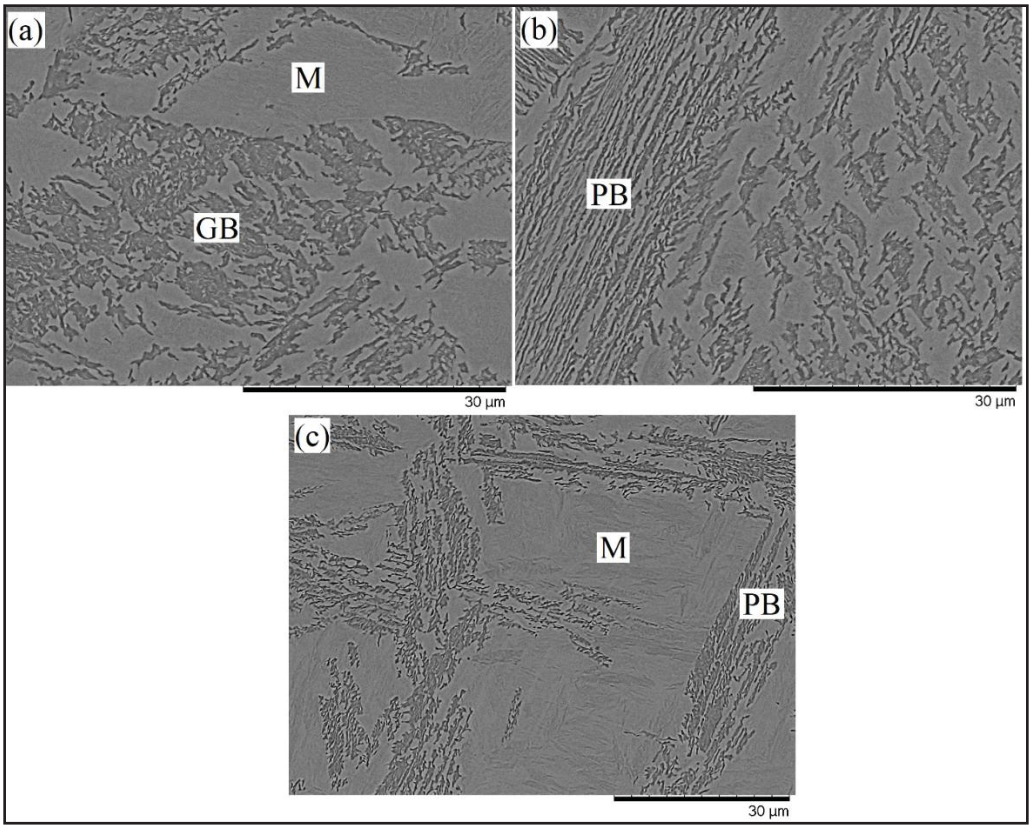

Figure 3-6 SEM image of the microstructure after tests with two different cooling rates, following austenitization at 1150 °C for 10 min. Granular bainite (GB), plate-like bainite (PB), and martensite (M)

3.4.5 Phase transformation (second stage)

As reported in Figure 3-4, the bainite transformation finish temperatures (B_f) are 430, 445, and 455 °C for holding times of 10 s, 10 min, and 35 min, respectively. The second transformation stage concluding at 320, 300 and 280 °C under the same conditions. On a time-temperature scale, this corresponds to second stage durations of approximately 36, 48 and 58 min for the investigated holding times of 10 s, 10 min, and 35 min, respectively.

Possible microstructure evolution scenarios during the second stage of cooling are schematically summarized in Figure 3-7. In this process, residual austenite may transform to martensite, while both the martensite and bainite phases could also undergo tempering. During the tempering of a carbon-supersaturated ferritic matrix (encompassing both bainite and

martensite) in the presence of a dispersed, carbon-rich austenitic phase, several pathways are plausible:

- One scenario involves the direct decomposition of retained austenite into ferrite and cementite (θ), following the reaction $\gamma \rightarrow \alpha + \theta$, which can result in either expansion or contraction in the RCL, depending on the retained austenite carbon content (Bhadeshia & Edmonds, 1980; Garcia-Mateo et al., 2012).
- Alternatively, Cementite may partially precipitate as via $\gamma \rightarrow \gamma^{-} + \theta$, (RCL expansion) stabilizing a lower-carbon austenite phase (γ^{-}), which may subsequently decompose fully into ferrite and cementite (Ruiz-Jimenez et al., 2020), or transform into martensite during further cooling ($\gamma^{-} \rightarrow \alpha' + \theta$) (RCL expansion).
- Another possible event is the partial loss of carbon supersaturation from the ferritic matrix, either by discrete precipitation within martensite (α (bct) $\rightarrow \alpha$ (bct or bcc) + θ) (Bhadeshia & Honeycombe) or by carbon transfer from the martensite to adjacent austenite ($\gamma + \alpha$ (bct) $\rightarrow \gamma^{+} + \alpha^{-}$ (bct)) (negligible contraction) (Ruiz-Jimenez et al., 2020).

All of these transformations are often overlapping and not strictly sequential, contributing to opposing features in the dilatometric signals. The observed response is the net result of these simultaneous processes. Accurately characterizing and quantifying these phenomena, and determining their individual contributions, is a complex process that requires advanced techniques such as high-temperature in-situ transmission electron microscopy or atom probe tomography. This detailed microscopic quantification is beyond the scope of the present macroscopic study and will be the subject of future collaborative work.

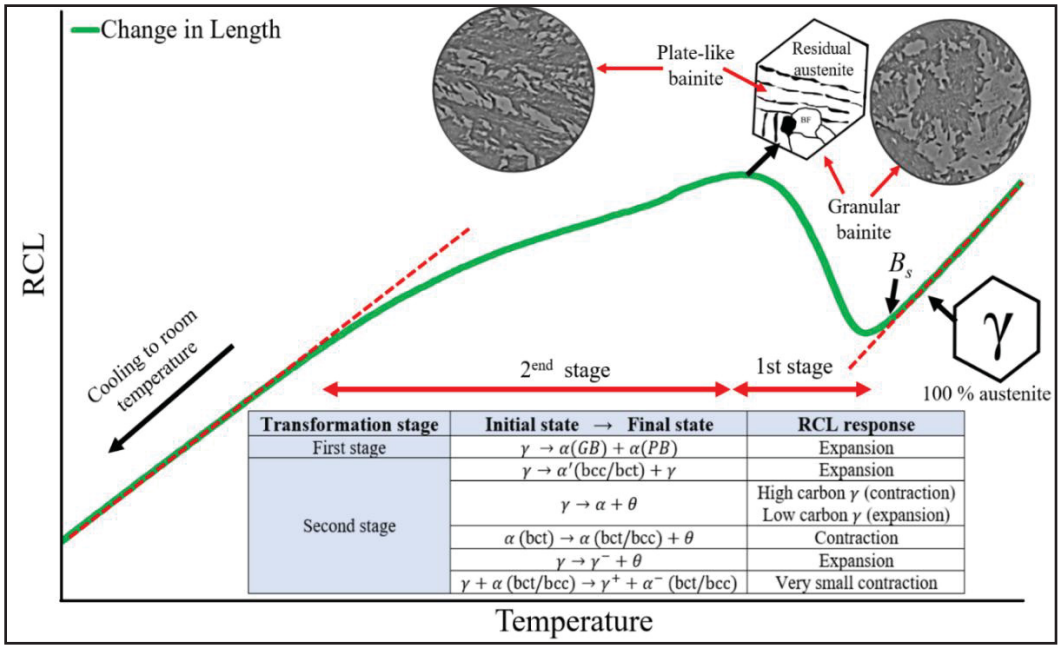

Transformation stage	Initial state → Final state	RCL response
First stage	$\gamma \rightarrow \alpha(GB) + \alpha(PB)$	Expansion
Second stage	$\gamma \rightarrow \alpha'(\text{bcc/bct}) + \gamma$	Expansion
	$\gamma \rightarrow \alpha + \theta$	High carbon γ (contraction) Low carbon γ (expansion)
	$\alpha\ (\text{bct}) \rightarrow \alpha\ (\text{bct/bcc}) + \theta$	Contraction
	$\gamma \rightarrow \gamma^- + \theta$	Expansion
	$\gamma + \alpha\ (\text{bct/bcc}) \rightarrow \gamma^+ + \alpha^-\ (\text{bct/bcc})$	Very small contraction

Figure 3-7 Change in length versus temperature, accompanied by SEM images and schematics illustrating microstructural changes at each stage of the phase transformation. Summary of the phase transformations in each stage and the associated RCL responses (table)

3.4.6 Microstructure analysis (SEM and XRD)

SEM analysis

Figure 3-8 presents SEM images of microstructures obtained after slow continuous cooling from the three PAGS, as in Figure 2-7. These reveal GB alongside plate-like morphology comprising morphologically indistinguishable PB and tempered martensite, as noted by Bhadeshia (H. Bhadeshia, 2001). In contrast to the rounded GB features, PB exhibits elongated, parallel ferrite sheaves separated by M-A constituents.

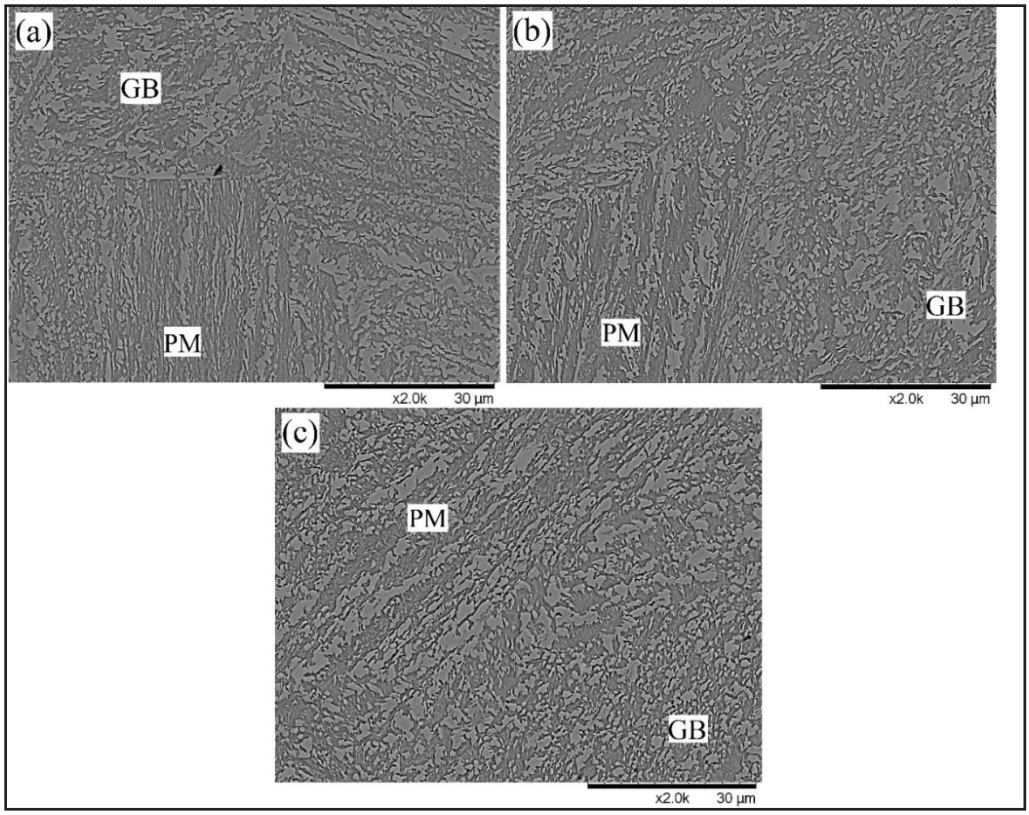

Figure 3-8 SEM images of the microstructure after cooling from 1150 °C with (a) 10 second, (b) 10 minutes, and (c) 35 minutes holding time. Plate-like Morphology (PM) and granular bainite (GB)

XRD analysis

Figure 3-9 shows the XRD diffractograms, with Table 3-1 summarizing the retained austenite (RA) volume fraction, the balance comprising ferritic matrix. The results indicate that RA increases from 10% to 24.4% as PAGS increases across the three samples. Although overlapping second stage transformations preclude precise identification of RA origins, this PAGS dependence resembles isothermal bainitic trends (Hasan et al., 2020; Ueji et al., 2021), however, continuous cooling conditions differ fundamentally and are not directly comparable. Previous studies of PAGS effects on bainitic transformation under continuous cooling did not asses its effect on RA stability (Lan et al., 2018; Lee et al., 2008; Zhao et al., 2017). The dilatometry results (Figure 3-4) clearly demonstrate that smaller PAGS promotes greater first

stage bainite formation, thereby reducing residual austenite available for further transformation in the second stage, a relationship consistently observed in the final microstructures.

Determination of the Carbon content

Using the equation from reference (Cheng et al., 1990) and Bragg's law (Bragg William Henry & Lawrence, 1913), the carbon content of RA was calculated for each condition and reported in Table 3-1. Due to overlap of the (111) austenite peak, values were as the average of the remaining three austenite peaks. The results indicate that RA carbon content across all conditions averages ≈1.2%, substantially enriched relative to the nominal carbon content (0.26%) of the alloy. Such increase contributes to its thermodynamic stability at room temperature, as will be discussed subsequently.

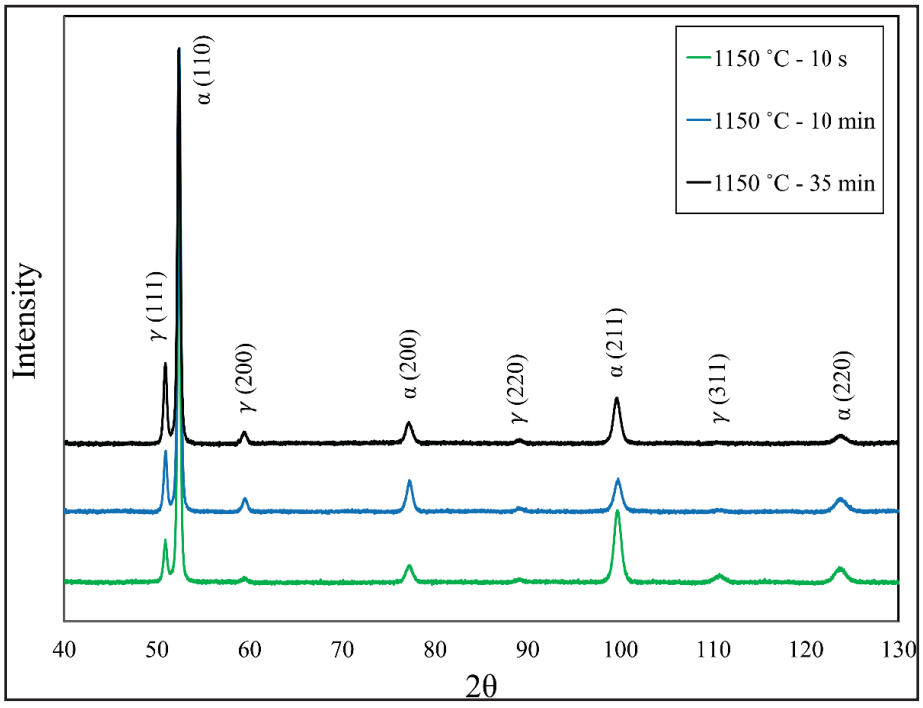

Figure 3-9 XRD patterns of samples with three different PAGS

Table 3-1 Quantitative data of RA in different thermally treated samples as obtained from the XRD analysis

Heat cycles	RA volume fraction (%)	C_γ	Ferrite volume fraction (%)
10 Sec – 1150 °C	10 ±1	1.23 ± 0.08	90 ±1
10 Min – 1150 °C	14 ±2	1.15 ± 0.03	86 ±2
35 Min – 1150 °C	24.4 ±3	1.22 ± 0.09	75.6 ±3

3.4.7 Hardness analysis (micro and nanohardness)

The results presented in the previous sections demonstrated that variations in PAGS lead to differences in phase transformation sequences and phase volume fractions. To evaluate the effect of these variations on the mechanical properties, hardness tests were conducted. Figure 3-10a shows microhardness measurement on the three samples with different PAGS. The hardness of the samples with different PAGS values was measured as 364±4 HV, 348±7 HV, and 347±3 HV for holding times of 10 s, 10 min, and 35 min, respectively. Although the differences in hardness are negligible, they align with the general trend that an increase in PAGS tends to reduce hardness (Alsalamah, 2020). In this system, hardness reflects the combined effect of several competing factors, including the retained austenite fraction, the formation of carbon-enriched martensite due to non-uniform carbon partitioning, the presence of M-A constituents, and strengthening contributions associated with martensite characteristics, such as, the density of high-angle boundaries and the dislocation density. Because these transformations occur concurrently and involve multiple stages, the hardness remains relatively stable despite changes in phase fractions. It is crucial to take into account various factors that can impact hardness after heat-treated cycles. These factors include the grain boundary density, the volume fractions of bainite, martensite, and retained austenite, the morphology of the phases (granular or plate-like) and the potential influence of the dislocation density. Due to the complexity of the multi-stage phase transformations and the simultaneous tempering processes, attributing hardness measurements directly to the grain size is challenging.

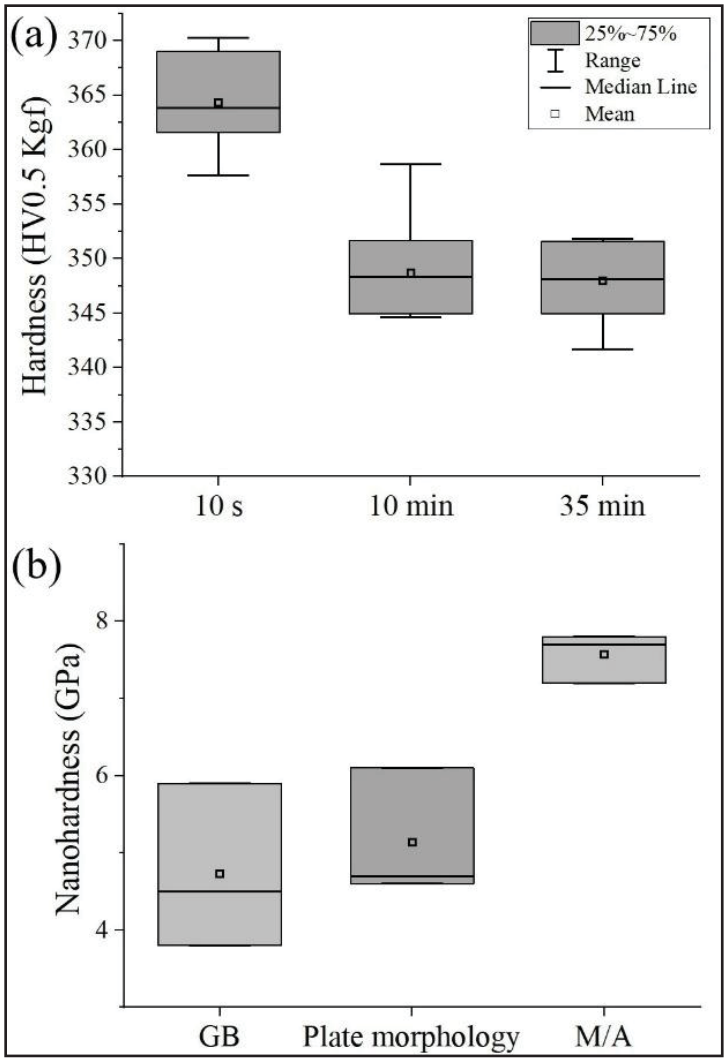

Figure 3-10 Microhardness variation for different austenitization holding times (a), and nanohardness of bainitic ferrite in granular bainite (GB), plate-like morphology, and M-A constituent (b)

To assess the contribution of individual phases to overall microstructural hardness, nanoindentation tests were conducted. Regions containing granular bainite (GB) and plate-like morphology identified as a mixture of PB and tempered martensite were targeted in the sample austenitized at 1150 °C for 10 min. Figure 3-11 presents representative SEM images acquired before and after nanoindentation of an M-A constituent. From 64 indentations, nine fully confined within α(GB), PB, or M-A regions were selected to compute average nanohardness values: 4.7 ± 1.0 GPa for α(GB), 5.1 ± 0.8 GPa for PB, and 7.3 ± 0.6 GPa for M-A zones (Figure 3-10b).

The markedly higher hardness of M-A zones reflects their elevated carbon content, consistent with electron probe microanalysis findings (Jiang et al., 2021). Differentiating nanohardness within plate-like morphology (PB vs. tempered martensite) proves challenging owing to morphological similarity, fine lath thickness, and identification difficulties in SEM. While local nanohardness provides insight into their differing mechanical responses based on boundary density, an exact crystallographic distinction of these phases requires advanced EBSD or TEM characterization of carbide precipitate orientations, which is slated for future work. Although nanoscale comparisons are unreported, macroscale studies indicate comparable hardness ranges for these phases. The lower α(GB) hardness arises from structural disparities relative to PB: despite shared transformation mechanisms, PB exhibits a higher density of high-angle boundaries (>50° misorientation), resulting in finer crystallographic packets and blocks (De-Castro et al., 2022). This enhanced boundary density accounts for PB's superior hardness.

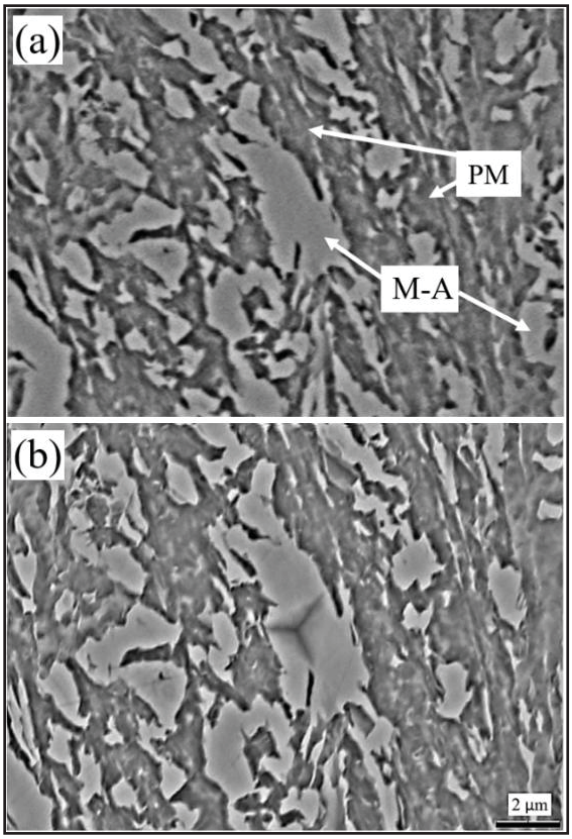

Figure 3-11 SEM images of the microstructure before (a) and after nanoindentation (b) on M-A zone in sample austenitized at 1150 °C for 10 minutes. α in plate-like morphology (PM), and martensite-austenite (M-A) constituent

3.5 Conclusion

In this research, the effect of PAGS on the bainitic phase transformation under continuous cooling was investigated, kinetics, microstructure and hardness were studied. The main conclusions can be summarized as follows:

1. Multi-stage phase transformation was observed under slow continuous cooling of large prior austenite grain size. First stage involved the formation of granular bainite and plate-like bainite. In the second stage, multiple phenomena occurred, including tempering of bainite formed in the first stage, followed by transformation of residual austenite to martensite and M-A zones, and an auto-tempering process.
2. Decreasing PAGS led to an increased volume fraction of the first-stage transformation products, while the volume fraction of the second-stage products decreased.

3. XRD measurements show a higher amount of retained austenite in samples with larger PAGS; however, despite differences in the volume fractions of retained austenite and other transformation products between the two stages, the overall hardness varied by less than 5%.

Acknowledgements

This work was supported by Natural Sciences and Engineering Research Council of Canada (NSERC-CRDPJ 536444). The authors gratefully acknowledge Finkl Steel-Sorel, particularly Mr. Jean-Benoît Moring, for providing materials and technical support for this study. We also extend our sincere thanks to Dr. Mohammad Saadati for his technical assistance in the laboratory. Carlos Garcia-Mateo acknowledges financial support from the Spanish National Research Council (CSIC) through project PIE-202560E084.

3.6 Chapter Summary and Outlook

This chapter examines bainitic transformation during continuous cooling in steels with very large prior austenite grain sizes. A multi-stage transformation sequence was identified, involving the formation of granular and plate-like bainite, followed by partial tempering and subsequent martensitic transformation with auto-tempering, attributed to austenite heterogeneity.

An increase in prior austenite grain size from 100 to 303 μm led to a significant rise in retained austenite (from 10% to 24.6%), emphasizing its key role in controlling the final microstructure and properties. These findings highlight the need for carefully optimized tempering cycles in large steel components to ensure effective decomposition of retained austenite, particularly in the core.

CHAPTER 4

Influence of bainitic transformation temperature on microstructure evolution during isothermal holding and subsequent cooling

Ehsan Tolouei[a], Mohammad Saadati[a], Jean-Benoit Morin[b], Carlos Garcia-Mateo[c], Mohammad Jahazi[a*]

[a] Department of Mechanical Engineering, École de technologie supérieure ÉTS, 1100 Notre-Dame St. W, Montreal, QC, H3C 1K3, Canada

[b] Finkl Steel-Sorel, 100 McCarthy, Saint-Joseph-de-Sorel, QC, J3R 3M8, Canada

[c] Department of Physical Metallurgy, National center for metallurgical research (CENIM-CSIC), Materalia Research Group, Avenida Gregorio Del Amo, 8, Madrid, 28040, Spain

* Corresponding author: Mohammad.Jahazi@etsmtl.ca, Tel: +1-514-396-8974, Fax: +1-514-396-8800

This article was published in Materials Chemistry and Physics, November 2025

4.1 Abstracts

Modified mold steels have recently gained attention as a novel approach in steel grades due to their high-performance applications. In this study, high-resolution dilatometry was used to study the isothermal bainitic transformation of a medium-carbon low-alloy steel after full austenitization at 900 ˚C, followed by austempering for 3 hours at temperatures ranging from 380 to 450 ˚C. The results showed that no bainitic phase transformation occurred at 450 ˚C, while an incomplete transformation was observed at all lower tested temperatures, and martensitic transformation occurred upon cooling at the final stage. Increasing the austempering temperature from 380 ˚C to 425 ˚C resulted in a lower volume fraction of bainite and a higher amount of martensite, whereas at 450 ˚C, a full lath martensite microstructure formed during final cooling. Electron backscatter diffraction (EBSD) and scanning electron microscopy (SEM) analyses revealed that increasing the isothermal holding temperature led to increased thickness of the bainitic blocks and a higher volume fraction of martensite. Vickers

hardness increased from 412 to 500 HV between 380 and 450 ˚C holding temperatures. This increase was attributed to the phase volume fraction, the carbon content of martensite, and the thickness of bainitic ferrite blocks. Nanoindentation tests were conducted on different martensitic and bainitic regions to compare the influence of isothermal holding temperature on the characteristics of the phases. The results indicated that as the isothermal temperature increased, the carbon content of martensite decreased, leading to a reduction in the nanohardness of the martensitic regions from 8.3 GPa at 400 ˚C to 7.8 GPa at 425 ˚C and 6.9 GPa at 450 ˚C. Furthermore, the average block thickness of bainitic ferrite increased from 0.71 μm to 1.98 μm as the isothermal temperature was raised from 380 ˚C to 425 ˚C, resulting in a decrease in nanohardness from 6.3 to 5.4 GPa. These findings are interpreted in terms of the evolution of bainitic block thickness and the carbon content of martensite at different austempering temperatures, as well as their impact on the hardness of the phases.

Keywords: Carbon-enriched martensite; nanohardness; block thickness; bainitic ferrite; retained austenite

4.2 Introduction

The rapid growth of automobile and plastics production markets has significantly promoted the production of new generation of mold steels to address the ever-increasing quality requirements of the industry (Wu et al., 2017). Specifically, microstructure uniformity and stability of mechanical properties are crucial requirements (H. Liu et al., 2018), particularly in the case of large size molds that have been developed in response to industry needs for very large bumpers and dashboards used in new vehicles. Medium-carbon Si-lean low-alloy steels, mostly derived from the AISI P20 family, are typically used for such applications. They are produced through ingot casting, open die forging, quenching and tempering (QT) treatments.

Recently, however, in addition to conventional QT treatment, the austempering process has also been employed to heat treat these mold steels (Ren et al., 2022). Due to the large thickness of the forged block, often more than 1000 mm, the resulting microstructure mainly consists of bainite, which offers a combination of high strength and good ductility, and has gained

considerable attention in the development of modern mold steel grades (Liu et al., 2019; Tolouei et al., 2024).

Although bainitic microstructures offer several advantages, their complexity stems from the fact that the type, morphology, and transformation kinetics of bainite are influenced by a combination of material-related factors, such as the alloy's chemical composition (Long et al., 2022), and process-related parameters. These include the austenitization temperature, which determines the prior austenite grain size (Mandal et al., 2022), cooling rate (Zhang et al., 2021), holding time and temperature in the bainitic field (commonly known as austempering) (Liu et al., 2016), etc. The mechanism of bainitic phase transformation, initiates with the nucleation and growth of bainitic ferrite (BF) plates supersaturated in carbon (H. K. D. H. Bhadeshia, 2001). Upon their formation, carbon is rejected into the surrounding austenite and the subsequent plates of bainitic ferrite nucleate in a more carbon-rich austenite. As the transformation continues, the remaining austenite becomes continuously enriched in carbon, reducing the driving force for further transformation (Bhadeshia & Waugh, 1982; Elena Pereloma & V.Edmonds, 2012; Zhao et al., 2019). This process progresses until the carbon content in the remaining austenite reaches a critical point where further transformation becomes thermodynamically unfavorable. This state is described by what is known as the T_0 curve, which represents the temperature at which austenite and ferrite with the same composition possess equal free energy. This phenomenon is referred to as the 'incomplete reaction phenomenon'. The austenite that remains untransformed at this stage is termed residual austenite (H. K. D. H. Bhadeshia, 2001).

In the austempering process, once the isothermal bainitic phase transformation is finished the microstructure consists of BF and carbon-enriched austenite (residual austenite). During the subsequent cooling to room temperature, and depending on the carbon content of the residual austenite, it may transform into martensite, or remain stable until room temperature, resulting in what is known as retained austenite (RA) (Garcia-Mateo et al., 2012).

Consequently, the room temperature microstructure may be composed of BF, martensite, and RA, with multiple factors affecting the volume fraction of each phase. These variations in phase volume fractions are key drivers of changes in the mechanical properties of austempered steels.

Austempering temperature is a key factor influencing carbon supersaturation in austenite, phase fractions, transformation kinetics, and mechanical properties (X. Y. Long et al., 2023; Su et al., 2022). However, RA is generally undesirable in mold steels, as its transformation under stress can impair machinability and dimensional accuracy (Wu et al., 2017). Thus, understanding RA stability during austempering is crucial for these steels. It is widely acknowledged that lowering the austempering temperature increases the volume fraction of bainite due to a higher driving force for transformation (lower free energy) (Bhadeshia & Christian, 1990; X. Y. Long et al., 2023; Tian et al., 2018). As the volume fraction of bainite increases, the proportion of austenite correspondingly decreases (Gao et al., 2022). Moreover, a higher volume fraction of bainite leads to enhanced carbon partitioning, leading to an increase in the carbon concentration within the remaining austenite (Franceschi et al., 2021; Tian et al., 2018). Consequently, this carbon-enriched austenite becomes more stable, reducing the likelihood of martensite formation during the final cooling to room temperature. This stabilization allows a significant portion of the austenite to remain stable at room temperature as RA.

For instance, Lee et al. (Lee et al., 2002), studied the austempering process of a high silicon steel and found that RA initially increased with rising austempering temperature and then decreased with further temperature increase. They reported that RA stability is influenced by the $f\gamma \times C\gamma$ parameter, representing the volume fraction of RA ($f\gamma$) and its carbon content ($C\gamma$), and as the volume fraction of residual austenite increases at higher austempering temperatures, the carbon content decreases slightly, leading to reduced RA stability. In another low-carbon, high-silicon steel, Tian et al. (Tian et al., 2018), reported that decreasing the austempering temperature from 430 ˚C to 400 ˚C resulted in a 3% increase in RA and a 20% decrease in martensite. It is evident that the RA volume fraction and the formation of martensite during the final cooling process can be influenced by the isothermal phase transformation temperature.

For example, Mondal et al. (Mondal et al., 2021), reported that raising the austempering temperature by 50 ˚C resulted in an increase in the volume fraction of martensite from 13.5% to 79% in medium carbon, high-silicon steels. It is worth mentioning that other factors, such as the deformation temperature prior to austempering, and Si content influence the volume fractions of bainite and retained austenite, as reported in (Bhadeshia & Edmonds, 1979; Franceschi et al., 2023). Austempering temperature affects not only phase volume fractions but also the morphology and mechanical properties of each phase. Lower temperatures refine the bainitic microstructure, while higher temperatures cause coarsening (Han et al., 2014). Garcia-Mateo et al. (Garcia-Mateo et al., 2003) highlight bainite plate thickness as key to its mechanical properties. Additionally, martensite formed at lower temperatures has higher carbon content, impacting its properties (X. Wang et al., 2023).

The above literature review emphasizes the importance of austempering temperature and its complex influence on determining the volume fraction of phases, the characteristics of each phase, and the resulting mechanical properties. Modifications of steel grades within the AISI P20 standard have introduced a new approach to mold steels in industrial applications. While most recent studies have focused on high-silicon steels examining, for instance, the effects of varying austempering time (Bhuyan et al., 2023; Han et al., 2017; Luo et al., 2021), and temperature (Kim et al., 2018; Pashangeh et al., 2020; Putatunda et al., 2011) these investigations are largely limited to high-silicon compositions. Other studies have explored high-manganese steels under austempering conditions, including deformation-assisted transformations (Grajcar & Krztoń, 2011; Grajcar et al., 2018; Morawiec et al., 2022), which differ significantly from the steel grades typically used in mold applications. In high-silicon steels, silicon plays a crucial role in suppressing carbide precipitation during the bainitic transformation, leading to the formation of carbide-free bainite. As a result, the bainitic microstructures in these steels differ markedly from those in medium-carbon low-alloy steels, particularly in terms of RA volume fraction, dislocation density (Long et al., 2017), the bainitic features size (Branco et al., 2018; Long et al., 2018), and the volume fraction and distribution of carbides (Gulbay et al., 2023). Therefore, there is a clear gap in the literature regarding the

behavior of novel, modified mold steel grades under austempering conditions. From an industrial perspective, quench and temper treatments are still widely used to achieve the desired mechanical properties in large forged mold steels. However, austempering presents a promising alternative that could eliminate the need for these costly and time-consuming processes. Realizing this potential requires a deeper understanding of bainitic transformation under isothermal conditions in medium-carbon low-alloy steels. Another novel aspect of the present study is the evaluation of global hardness after austempering using localized data. This was achieved through a comparative analysis of the nanohardness of individual microstructural phases, offering a new approach to characterizing bainitic microstructures.

4.3 Materials and methods

The detailed methodology employed in this chapter is described in Chapter Two.

4.4 Results and Discussion

4.4.1 Dilatometry analysis and phase evolution

Variations in the length during the entire heat treatment cycle are shown in Figure 4-1a for all tested conditions. The Ac_1 and Ac_3 temperatures which correspond to the onset and conclusion of the austenitic transformation, were determined to be 780 ˚C and 825 ˚C, respectively, coinciding with the commencement and conclusion of the shrinkage observed during the heating process to 900 ˚C.

Upon cooling to the isothermal temperatures after the austenitization stage, the fully austenitic microstructure remains stable, as indicated by the linear contraction due to the decrease in temperature observed in Figure 4-1, suggesting that no intermediate transformations such as ferrite/perlite occur.

Once at the targeted isothermal temperatures (Figure 4-1b), and with the exception of the 450 ˚C treatment, an expansion of the material is observed at 380, 400 and 425 ˚C which is associated with the occurrence of the bainitic phase transformation (Gao et al., 2022).

As expected, the maximum length change ΔLmax (L_{max} - L_0) increases with decreasing austempering temperature (Figure 4-1b) where, L_0 and L_{max} represent the sample length before and after the isothermal phase transformation. As already anticipated, this observed trend aligns with theoretical predictions and other experimental evidence (Gao et al., 2022; Rampelberg et al., 2021), indicating that a higher fraction of BF forms at lower austempering temperatures. The greater length change is attributed to the volume expansion that occurs when austenite transforms to BF.

For the case of isothermal holding at 450 ˚C, as can be observed in Figure 4-1b, no expansion is detected during the isothermal step, i.e. no bainitic transformation takes place. Accordingly, on cooling to room temperature, martensitic transformation of the untransformed austenite occurs, starting and finishing at 345 ˚C and 212 ˚C, respectively (Table 4-1).

Further analysis of the dilatometric curve of the 425 ˚C treatment reveals that during the final cooling stage, the martensitic transformation starts at 328 ˚C and finishes at 166 ˚C (Table 4-1). Similarly, for the 400 ˚C treatment, martensitic transformation is observed, but at the lower temperature of 110 ˚C (Table 4-1). Finally, after the formation of bainite at 380 ˚C, no martensitic transformation is observed.

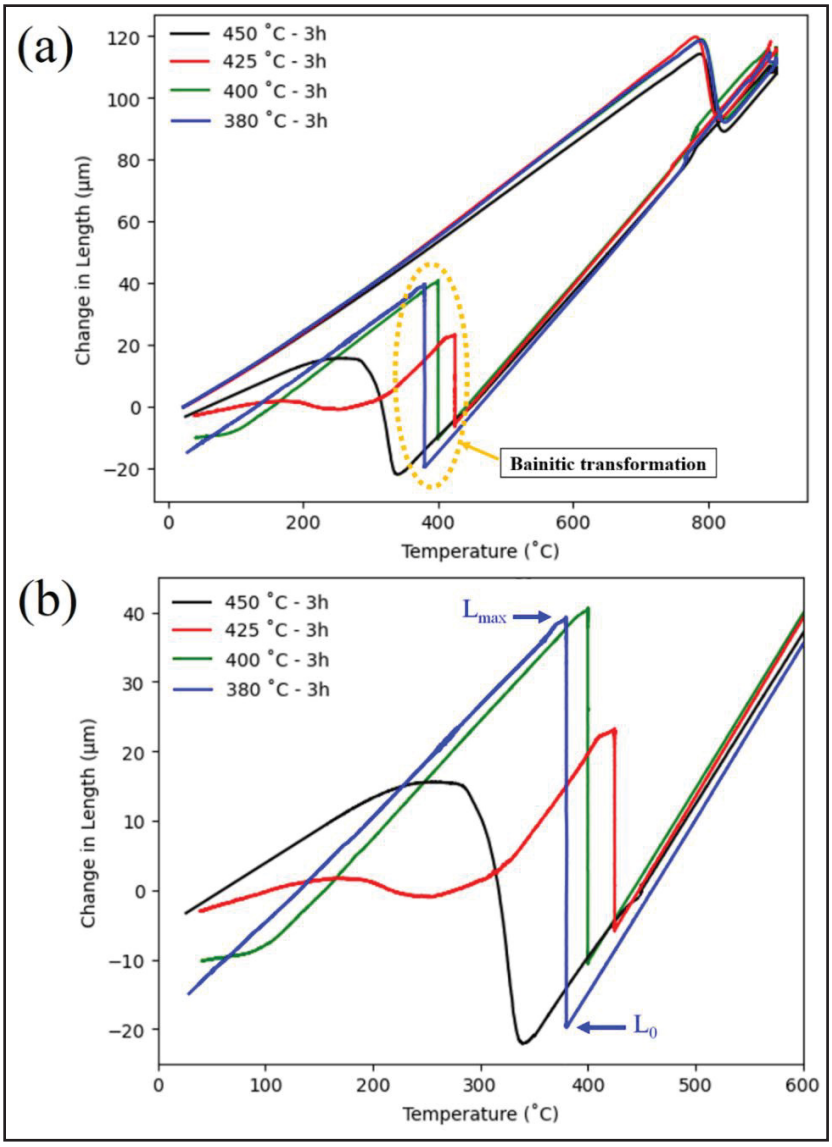

Figure 4-1 Change in length as a function of temperature for the dilatometry specimens: (a) during the whole treatment as in Figure 1; (b) magnified view of the isothermal step followed by final cooling to room temperature

Therefore, based on the results in Table 4-1, it is clear that as the isothermal transformation temperature decreases and the amount of bainite increases, the Ms temperature also decreases, indicating an increase in the carbon content of the transformed residual austenite. Such differences in the martensite start temperature (Ms) after isothermal holdings is another notable observation, as it is not identical for all temperatures. It can be seen that lowering austempering temperature causes the Ms temperature to drop from 345 ˚C to below room temperature in

samples held at 450 ˚C and 380 ˚C, respectively (Table 4-1). These changes can be explained by the nature of the bainitic transformation, in which the redistribution of carbon from supersaturated bainitic ferrite to the surrounding austenite is an inherent part of the transformation process (H. K. D. H. Bhadeshia, 2001). The carbon content of the martensite formed during cooling to room temperature, after the isothermal step, can be indirectly estimated using empirical equations that relate the Ms temperature to the chemical composition of the austenite from which it forms. In the present work, the equation reported by Barbier (Barbier, 2014) was selected, as it yield the calculated Ms value (346 ˚C) closest to the experimental result for the 450 ˚C treatment (345 ˚C), as shown in Table 4-1. Since no bainitic transformation occurred at that temperature, the carbon content of the austenite transforming to martensite corresponds to the bulk composition (Table 2-1). On this basis, the martensite carbon content in samples treated at the other temperatures was calculated and is summarized in Table 4-1. As anticipated, the results clearly show an enrichment in the residual austenite after the bainitic transformation, as the isothermal transformation temperature decreases and more bainite forms.

Table 4-1 Characteristics of samples subjected to different isothermal bainitic phase transformation treatments

Isothermal temperature (˚C)	M_s temperature (˚C)	Carbon content of martensite (wt%)	Martensite volume fraction (%)	RA volume fraction (%) ±3%	Bainitic ferrite volume fraction (%) ±3%
450	345	0.26	100	0	0
425	328	0.29	57	4.7	38.3
400	110	1.02	12	7	81
380	< 25	-	0	6.4	93.6

Dilatometric curves can be utilized to estimate the volume fraction of martensite formed during heat treatment, as described in reference (Morawiec et al., 2022) and illustrated in Figure 4-2. The curve corresponding to the 450 ˚C treatment was used as a reference, representing a fully martensitic microstructure (100% martensite with no RA), which was later confirmed by XRD analysis. By comparing the magnitude of length change associated with each isothermal holding treatment to this reference, the volume fraction of newly formed, carbon-enriched martensite was determined. For samples cooled from 400 ˚C and 425 ˚C, the estimated martensite volume fractions were 12% and 57%, respectively (Table 4-1).

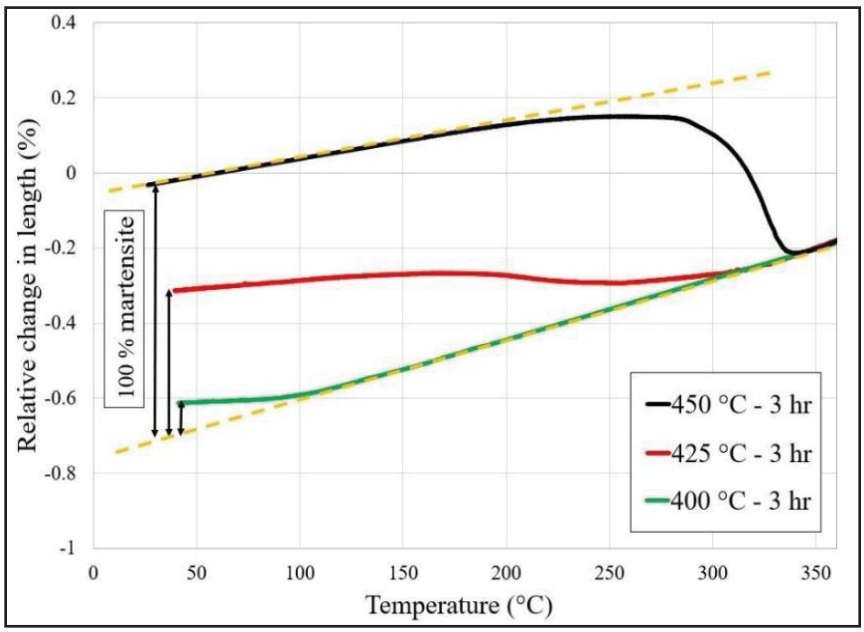

Figure 4-2 Relative change in length versus temperature for the determination of martensite fraction upon cooling to room temperature

4.4.2 Microstructure analysis

As previously stated, before the remaining residual austenite stabilizes at room temperature, a portion of it, which is low in carbon, transforms into martensite prior to reaching room temperature (M. Morawiec et al., 2020). The volume fraction of RA at room temperature was determined using XRD and the results are reported in Table 4-1. For all treatments, the XRD

patterns are shown in Figure 4-3. It can be seen that the volume fraction of RA is close to zero at 450 ˚C and no γ peaks appear in the diffraction pattern. RA volume fractions increase with lowering the isothermal phase transformation temperature (380 ˚C and 400 ˚C), but none of the samples had an RA volume fraction above 10%. The RA volume fraction was calculated to be approximately 6.4%, 7%, and 4.7% at temperatures of 380 ˚C, 400 ˚C, and 425 ˚C, respectively. The above results are in agreement with those of Morawiec et al. (M. Morawiec et al., 2020) who observed that with decreasing austempering temperature, a higher content of stable RA with higher carbon, would be present at room temperature. Yao et al. (Yao et al., 2021) attributed this to the fact that lower austempering temperatures promote a greater degree of bainitic transformation, allowing more carbon to partition into the surrounding untransformed austenite.

Using the calculated martensite volume fraction from the dilatometry test results (Figure 4-2 and Table 4-1) and the RA volume fraction derived from the XRD analysis, the bainite volume fraction at each temperature was determined as 100 - (Martensite + RA), and is summarized in Table 4-1. The findings indicate that as the isothermal temperature rises, the volume fraction of martensite increases, while the volume fraction of bainite decreases. This finding is in agreement with dilatometry results which showed lower expansion during bainitic phase transformation. It appears then that the lower carbon content in residual austenite at 400 and 425 ˚C leads to instability, causing partial transformation to martensite during final cooling.

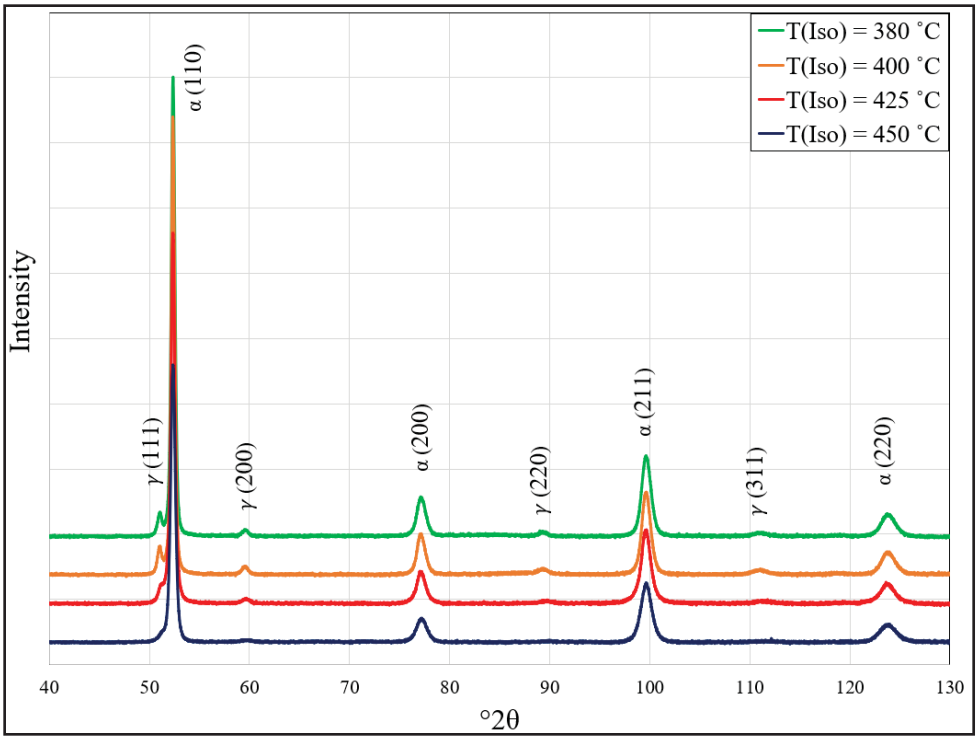

Figure 4-3 XRD patterns of samples held at different austempering temperatures

Figure 4-4 shows SEM micrographs of samples after the selected isothermal treatments. The microstructure of the samples tested at 380 ˚C (Figure 4-4a) shows bainite and RA islands. Increasing temperature to 400 and 425 ˚C, Figure 4-4 (b and c), shows large martensite zones surrounded by bainite and dispersed RA zones. Finally, a full lath martensite microstructure can be seen in the sample tested at 450 ˚C (Figure 4-4d). The identified microstructures are in accordance with the previous phase calculations and dilatometric experiments.

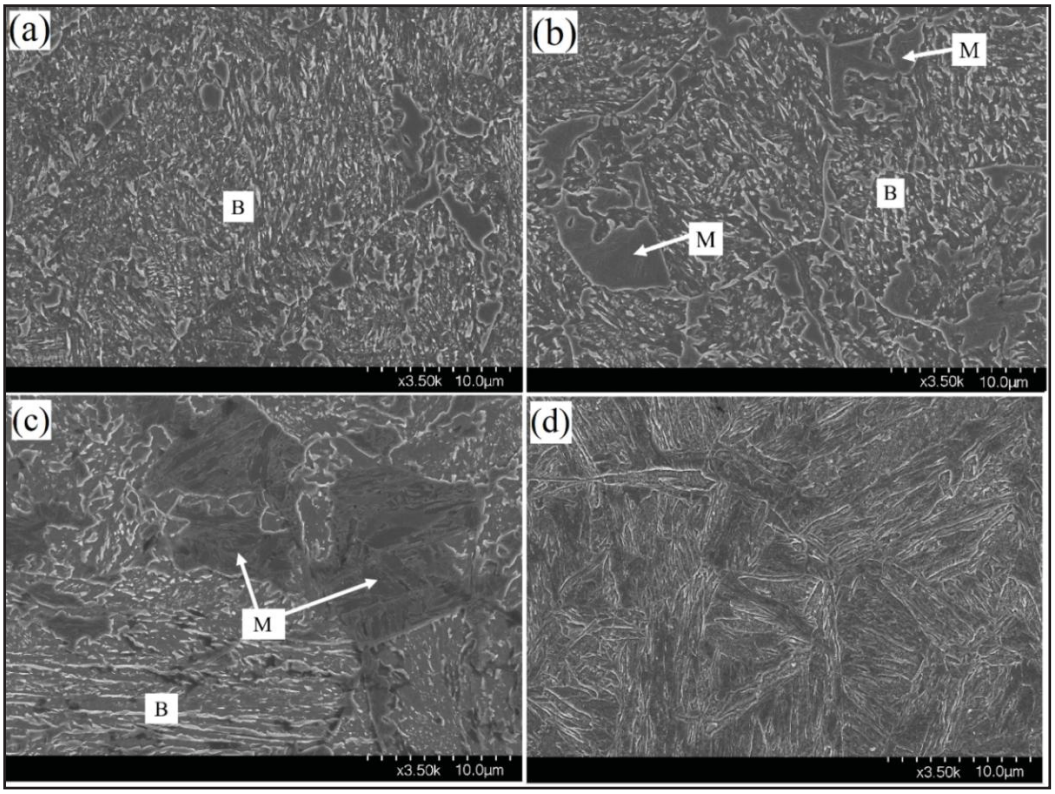

Figure 4-4 SEM of the steel after different isothermal holding at (a) 380 ˚C, (b) 400 ˚C, (c) 425 ˚C and (d) 450 ˚C for 3 hours. Bainite (B), retained austenite (RA), and martensite (M)

In order to measure the thickness of the BF block, the EBSD technique was employed. Figure 4-5 presents the EBSD map along with the corresponding distribution of the BF thickness. The dark pixels (non-indexed regions) in the phase map represent areas where no indexing solution could be determined for the corresponding diffraction patterns either due to disproportion of selected phase parameters or could be due to lack of any patterns from the measured spot. The latter is a result of relatively high strain and a high density of lattice defects which lead to low-quality or undetectable patterns (Baek et al., 2020; Isasti et al., 2016; Jeong et al., 2002; Tolouei et al., 2024). The martensite areas also display poor crystallographic indexing due to internal strains and dislocations, resulting in lower pattern contrast and darker regions compared to the bainitic areas, which are generally better indexed in EBSD analysis when the two phases coexist (Navarro-López et al., 2017; Pashangeh et al., 2019). The bainitic block thickness was

calculated using the open-source crystallographic toolbox MTEX (v5.7.1) along with MATLAB (version R2022a) add-on. In this method, it is important to note that for samples tested at 400 ˚C and 425 ˚C, where both bainite and martensite are present, measurements were performed individually for each grain. This approach ensured that martensite zones were not mistakenly identified as BF blocks. In Figure 4-5(b, d, and f), the average of the block thickness, for the sample held at 380 ˚C, is 0.71 μm. For the sample held at 400 ˚C, the average thickness range shifts to 1.37 μm and it further increases to 1.98 μm for the sample held at 425 ˚C. The variation in the thickness of the BF blocks cannot be attributed to a single factor; indeed, multiple factors play combined roles for the observed variations (Cornide et al., 2013). Garcia-Mateo et al. (Garcia-Mateo et al., 2017) reported that the thickness of the BF plates are mainly influenced by three factors: the strength of austenite at the transformation temperature, the austenite dislocation density, and the chemical free energy change associated with the transformation. However, they have reported that as the transformation temperature decreases, all the above three factors increase, resulting in thinner BF blocks (Cornide et al., 2013).

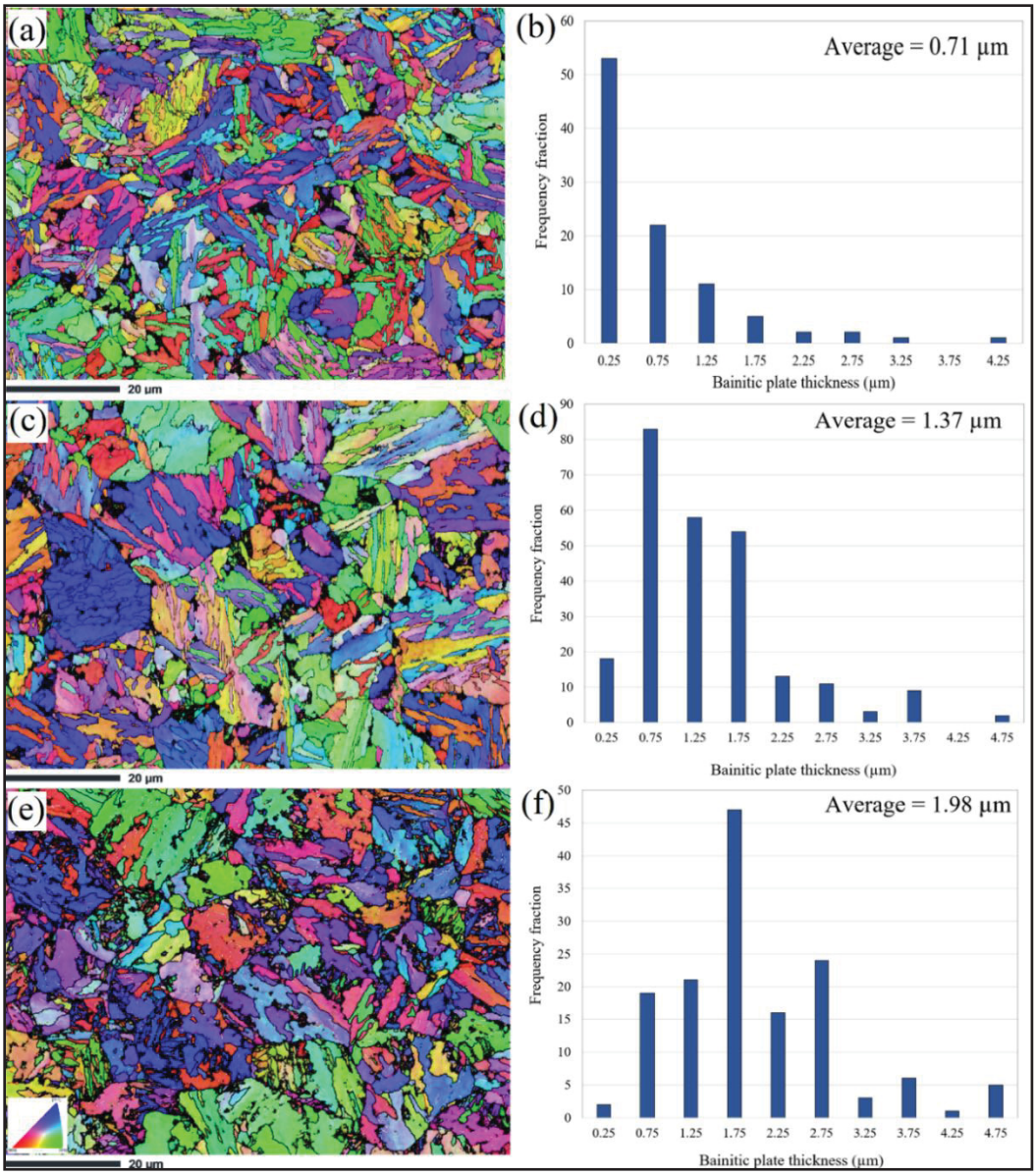

Figure 4-5 EBSD map and corresponding distribution of bainitic block thickness of the steel after different isothermal holdings at, (a-b) 380 ˚C, (c-d) 400 ˚C, and (e-f) 425 ˚C for 3 hours holding

4.4.3 Hardness evolution

4.4.3.1 Micro-hardness

Figure 4-6 shows the variation in phase volume fractions and micro-Vickers hardness after different isothermal transformation temperatures. The overall trend in hardness indicates that, as the isothermal holding temperature increases, the microhardness rises. The results show that, despite different microstructures, the hardness of isothermally treated samples at 380 and 400 ˚C are in the same range, 412 and 411 HV, respectively. Although the amount of retained austenite is similar in both samples, the main difference between the samples held at 380 and 400 ˚C is the presence of 12% martensite and bainite with thicker blocks. In bainitic microstructures, the primary factor affecting hardness is the thickness of the bainitic plates, as reported by Garcia-Mateo et al. (Garcia-Mateo et al., 2003). The results indicate that while the presence of 12% carbon-enriched martensite in the microstructure increased the variation in hardness (as evident from the error bars), the average hardness remained unchanged.

The microstructures of the samples treated at 425 ˚C and 450 ˚C exhibited significant differences (Figure 4-4). At 425 ˚C, the microstructure comprises 38.3% thick block bainite (1.8 μm), 4.7% RA, and 57% carbon-enriched martensite, resulting in a hardness of 485 HV. In contrast, the sample treated at 450 ˚C consists entirely of martensite with nominal carbon content, yielding a hardness of 500 HV. This comparison reveals that the lower hardness of bainite in thick block is compensated by the carbon-enriched martensite formed at lower temperatures. This observation underscores the crucial role of carbon content in determining the hardness of martensite (Kwak et al., 2022).

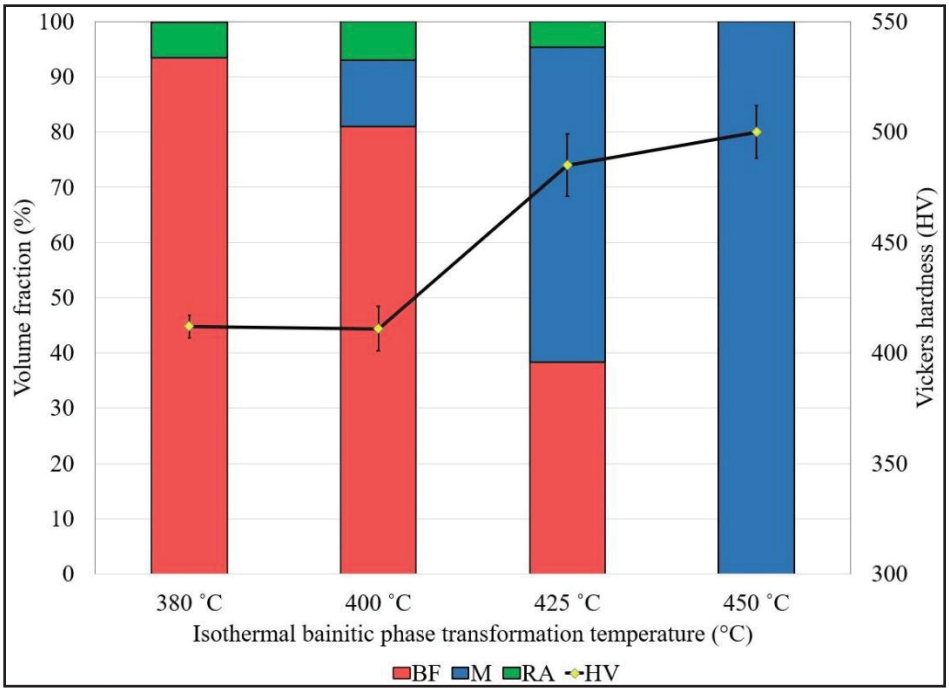

Figure 4-6 Variation in micro-hardness and phase volume fraction after different isothermal treatment temperatures. Bainitic ferrite (BF), martensite (M), retained austenite (RA)

4.4.3.2 Nanohardness

Despite the above reported observed differences in the carbon content of martensite, due to the small size of martensite islands, more local analysis is needed to eliminate any interference from the neighbouring microstructural features. To this end, nanoindentation tests were performed inside the bainite and martensite zones to evaluate the mechanical properties of each of the phases at 380, 400, 425, and 450 ˚C.

Figure 4-7 and Figure 4-8 show the load-displacement curves obtained from nanoindentation tests conducted on bainite and martensite in samples treated at different temperatures, and Figure 4-9 and Table 4-2 summaries the corresponding average nanohardness. The results clearly reveal that as the isothermal phase transformation temperature increases, the average penetration depth also increases in bainite zones. Correspondingly, as shown in Figure 4-9, the average measured nanohardness decreases, with values dropping from 6.3 GPa at 380 ˚C to

5.7 GPa at 400 ˚C, and further to 5.4 GPa at 425 ˚C. The reduction in the thickness (1.98 to 0.71 µm) of the bainitic block, can be an essential factor for enhancing the hardness of austempered steels (Skowronek et al., 2022). As noted earlier, the final thickness of the bainitic block is primarily influenced by several factors, and it can generally be reduced by conducting the bainitic transformation at lower temperatures (Garcia-Mateo et al., 2017; Huang et al., 2013; Skowronek et al., 2022).

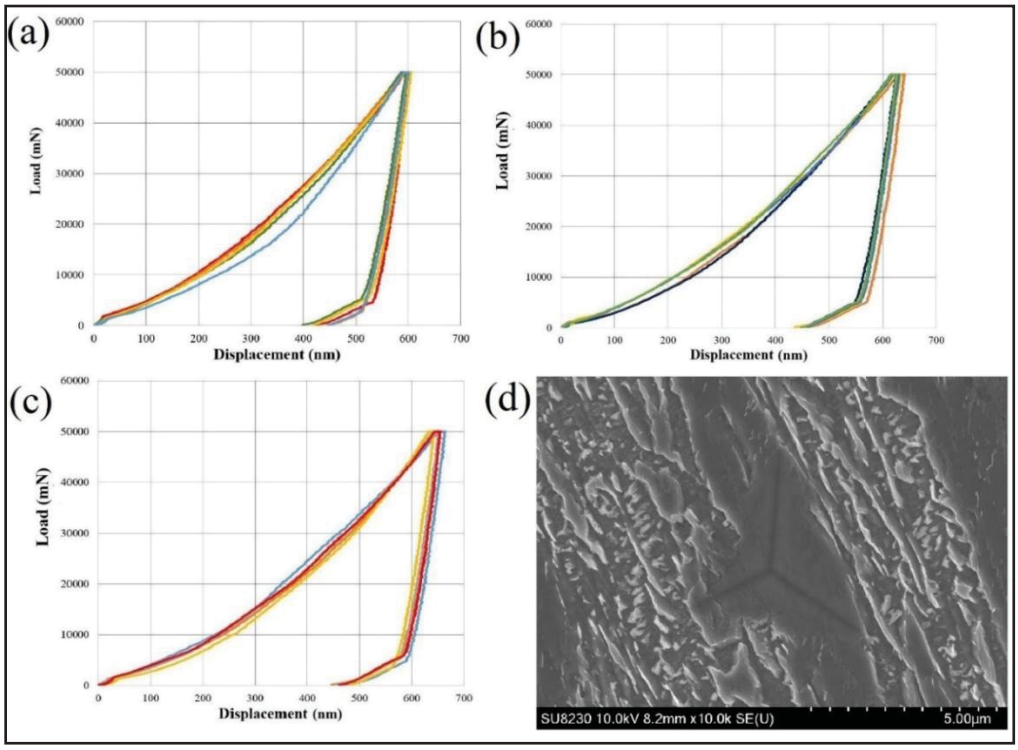

Figure 4-7 Load-displacement curves obtained in a nanoindentation on the bainitic zones at different cycles (a) 380 ˚C, (b) 400 ˚C, and (c) 425 ˚C, and the typical SEM image after indentation on the bainitic zones (d)

Figure 4-8 (a-c) presents nanoindentation curves for martensite in samples treated at 400 ˚C, 425 ˚C, and 450 ˚C, respectively. The results reveal that the maximum depth of penetration is obtained in the martensite zones, averaging 500, 533 and 580 nm, for the samples 400, 425 and 450 ˚C, respectively. This observation suggests that the martensite formed at 400 and 425 ˚C from residual austenite with higher carbon, possesses a greater resistance to deformation in comparison to the martensite formed from primary austenite in the 450 ˚C sample. The average

measured nanohardness was 8.3, 7.8 and 6.9 GPa for the martensite at 400, 425, and 450 ˚C, respectively, as reported in Figure 4-9. An overview of all hardness measurements can be found in Table 4-2.

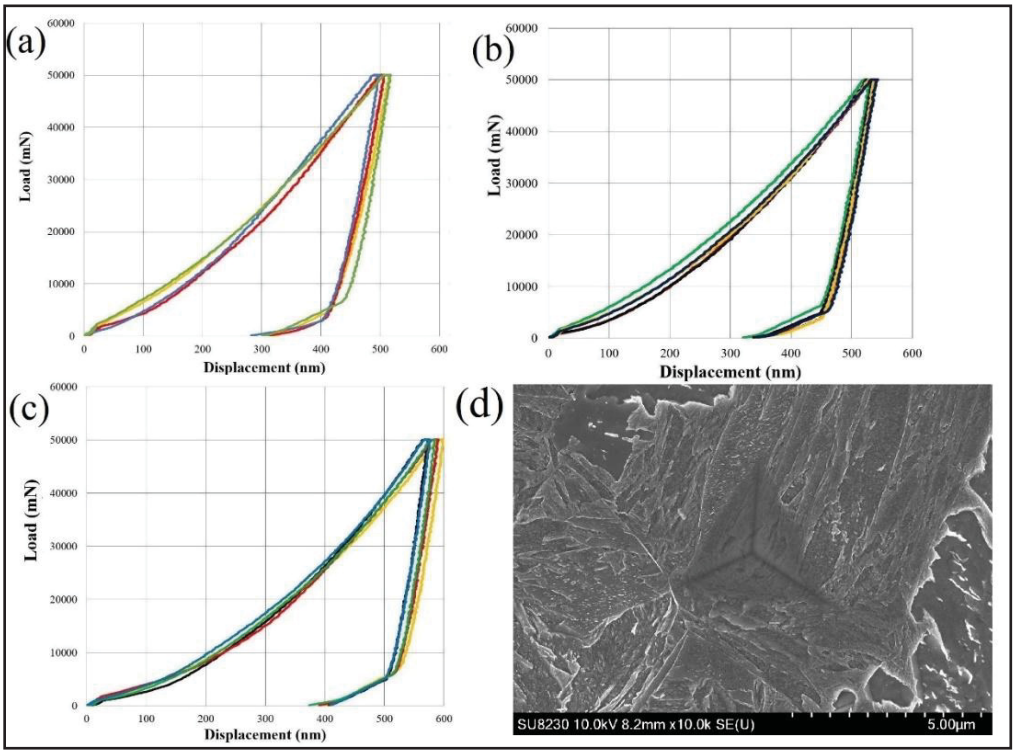

Figure 4-8 Load – displacement curves obtained in a nanoindentation on the martensitic zones at different cycles (a) 400 ˚C, (b) 425 ˚C, and (c) 450 ˚C, and the typical SEM image after indentation on the martensitic zones (d)

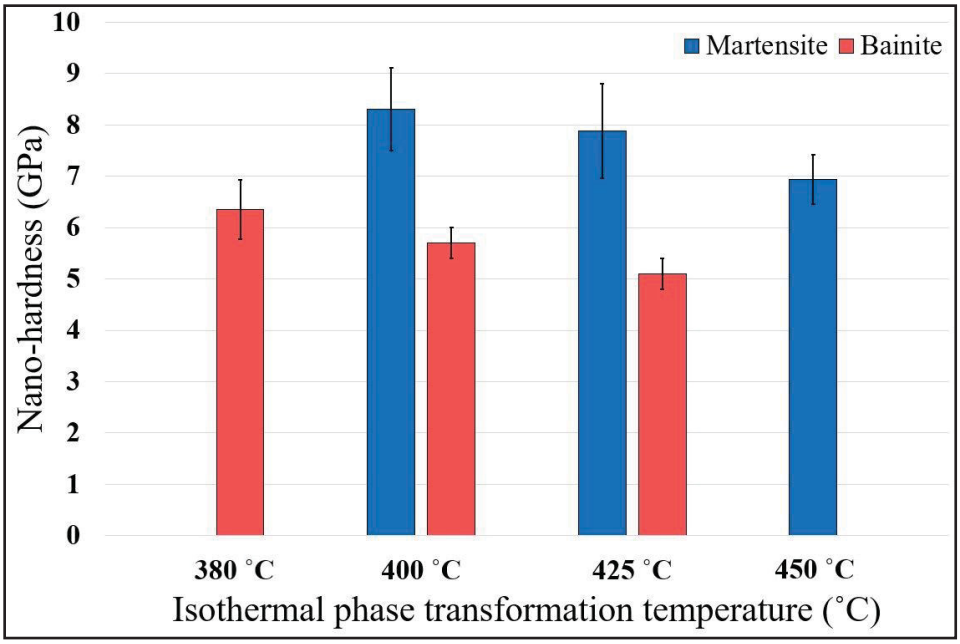

Figure 4-9 Average nanohardness of bainite and martensite at different isothermal holding temperatures

Table 4-2 Hardness measurement results

Isothermal phase transformation temperature (°C)	Vickers hardness (HV)	Nanohardness (bainite)	Nanohardness (martensite)
380	412 ±5.2	6.3 ±0.5	-
400	411 ±9.9	5.7 ±0.3	8.3 ±0.8
425	485 ±14	5.4 ±0.2	7.8 ±0.9
450	500 ±12	-	6.9 ±0.4

4.5 Conclusions

In this research, the influence of austempering temperature on the microstructural evolution of medium-carbon low alloy steel was investigated using high-resolution dilatometry, SEM, and EBSD. The effect of various phase fractions on overall hardness and phase-specific hardness were measured through micro-Vickers and nanoindentation methods, respectively. The following main conclusions can be drawn from this investigation:

1. The block thickness of bainitic ferrite and the carbon content of martensite significantly influence the nanohardness of these phases.
2. The refinement of the bainitic ferrite microstructure resulted from a lower austempering temperature and led to higher nanohardness.
3. Lower austempering temperatures lead to increased carbon rejection into residual austenite, resulting in the formation of martensite with higher carbon content, as confirmed by nanoindentation analysis.
4. The formation of martensite from incomplete phase transformation at higher austempering temperatures lead to greater bulk hardness compared to transformation at lower temperatures.

4.6 Chapter Summary and Outlook

This chapter presents an assessment of a new mold steel manufacturing route based on isothermal holding (austempering). Holding temperatures relevant to industrial practice were investigated, and the associated phase transformation and resulting microstructures were characterized. A temperature of 380 °C was identified as optimal for subsequent industrial testing. This method can be replaced by a continuous cooling process, as investigated in the previous chapter for small blocks. Following phase transformation by either continuous cooling or isothermal processing, tempering constitutes the next step in mold steel manufacturing. Accordingly, the next chapter examines the non-uniformity of the tempering process in this class of steels for large blocks.

CHAPTER 5

Influence of holding times on the tempering mechanisms of bainitic microstructure

Ehsan Tolouei[a], Valentin Hurel[b], Sajad Mirzaei[a], Jean-Benoit Morin [b], and Mohammad Jahazi[a]*

[a] Department of Mechanical Engineering, École de Technologie supérieure (ÉTS), 1100 Notre-Dame St. W, Montreal, QC, H3C 1K3, Canada
[b] Finkl Steel-Sorel, 100 McCarthy, Saint-Joseph-de-Sorel, QC, J3R 3M8, Canada

* Corresponding author. E-mail addresses: mohammad.jahazi@etsmtl.ca (Mohammad Jahazi)

This article was published in Materials Science and Technology, October 2025

5.1 Abstract

In this study, the effect of different tempering time in heat treatment of thick mold steel blocks was investigated. The tempering of bainitic microstructure evolution during short (30 minutes) and long (14 hours) tempering at 620 °C, after austenitization at 900 °C was investigated. High-resolution dilatometry and microscopy revealed that the 10% retained austenite, present before tempering, decomposes directly during tempering and indirectly into fresh martensite during cooling after short tempering. In contrast, prolonged tempering results in the complete decomposition of the retained austenite. Short tempering maintains hardness, due to the formation of fresh martensite. In prolonged tempering, hardness is significantly reduced because of the martensite–austenite constituents tempering, and recovery of low-angle grain boundaries, as confirmed by nanoindentation and electron backscatter diffraction analyses.

Keywords: Low-angle boundaries, Retained austenite, Fresh martensite, Martensite-austenite constituent, Nanoindentation

5.2 Introduction

The demand for large-sized forged steel blocks has been continuously increasing in recent years. These blocks are used as plastic injection molds for producing large automotive components such as bumpers and dashboards. Medium-carbon low-alloy steels, primarily from the AISI P20 family, are commonly employed for these applications. Their production involves ingot casting, open-die forging, and subsequent quenching and tempering (QT) treatments before final machining to produce the molds' cavities (Bouissa et al., 2021; Talebi et al., 2017). These blocks often exceed a meter in thickness, and as a result, substantial non-uniformities in temperature distribution, and hence phase transformation kinetics, could arise during the quenching process. The microstructure of these blocks is composed of bainite, except for a very narrow martensitic region close to the quenched surface. The non-uniform cooling produces different bainitic transformation kinetics that influence the final properties of the block due to its thickness.

The bainitic phase transformation begins with the nucleation and growth of carbon-supersaturated bainitic ferrite plates (H. K. D. H. Bhadeshia, 2001). As these plates form, carbon diffuses into the surrounding austenite, causing subsequent bainitic ferrite plates to nucleate in increasingly carbon-rich austenite (residual austenite). It should be noted that, due to the slow cooling rate, dispersed carbides precipitate simultaneously with the formation of BF plates as a result of carbon supersaturation. As the transformation advances, the remaining austenite becomes progressively enriched with carbon, diminishing the driving force for further transformation (Bhadeshia & Waugh, 1982; Elena Pereloma & V.Edmonds, 2012; Zhao et al., 2019). This process continues until the carbon content in the residual austenite reaches a thermodynamic limit, known as the T_0 condition, beyond which further transformation is no longer possible (H. K. D. H. Bhadeshia, 2001). After the phase transformation, during the final cooling to room temperature, three scenarios are possible: The residual austenite may either remain stable at room temperature as retained austenite (RA), completely transform into martensite depending on its carbon content, or partially transform into martensite, resulting in a martensite–austenite (M/A) constituent. Therefore, the final

microstructure is composed of bainitic ferrite, RA, martensite/austenite (M/A) constituent, and carbides (Tolouei et al., 2024).

The subsequent stage, tempering, is a crucial step in the manufacturing process, as it significantly influences the final microstructure. For example, one of the objectives of the tempering process is to reduce or eliminate undesired phases like RA (Podder, 2011), as stress- or strain-induced martensitic transformation can negatively impact machining properties and compromise the mold's dimensional accuracy (Ruiz-Jimenez et al., 2020; Wu et al., 2017). Therefore, optimizing tempering time and temperature to ensure the complete decomposition of RA during the tempering process is critically important for this class of steels. However, bainite demonstrates resistance to tempering due to the auto-tempering that occurs during its formation (H. K. D. H. Bhadeshia, 2001). The situation is more complex in the case of large steel blocks, because achieving the target tempering temperature at the block core can take over 30 hours in some cases (Mirzaei et al., 2023). During this time, the surface reaches tempering temperature while the center is still heating, resulting in a non-uniform bainite tempering process with negative consequences for the final mechanical properties.

A review of the literature indicates that the heating rate, tempering temperature, and tempering time are key factors influencing the softening mechanism. Talebi et al. (Talebi et al., 2017) studied the effect of different heating rates on bainitic microstructures; however, the softening mechanism and post-tempering hardness of bainite were not explored. The authors also investigated the effect of tempering heating rates in medium-carbon low-alloy steel and observed that bainite exhibited resistance to this factor, with no significant differences in hardness after tempering (Tolouei, Hurel, et al., 2025). Research on the impact of tempering temperature has shown that higher temperatures lead to more RA decomposition, recovery of dislocations, and coarsening of bainitic ferrite plates, all of which contribute to a reduction in hardness (Ruiz-Jimenez et al., 2020; Wang et al., 2022). Ståhlkrantz et al. (Ståhlkrantz et al., 2020) examined the influence of tempering time on the tempering mechanism in a medium-carbon low-alloy steel and observed a reduction in hardness after both 10 minutes and 24 hours of holding at 300°C. They concluded that the primary factor responsible for the decrease in

hardness was dislocation annihilation, as the sizes of carbides and the thickness of bainite plates remained largely unchanged, showing no significant influence on hardness. In high-carbon, high-silicon steel, Garcia-Mateo et al. (Garcia-Mateo et al., 2004) observed minimal coarsening of bainitic plates, attributed to the formation of carbides from carbon-enriched austenite, which inhibits the coarsening process. Additionally, as a softening mechanism during tempering, the decomposition of M/A into ferrite and carbides has been reported by Dixit et al. (Dixit et al., 2020) in low-carbon low-alloy steel.

Although bainite demonstrates greater resistance to the tempering process, most research in the literature focuses on martensite. Limited information is available on the tempering of bainite, especially in large steel blocks exposed to prolonged tempering cycles. It is also worth noting that most of the studies on bainitic microstructures primarily focus on high-silicon steels, owing to the crucial role of silicon in suppressing carbide formation during the bainitic transformation in carbide-free bainite (Bhadeshia & Edmonds, 1979), whose bainitic phases are different from those of medium carbon steels. The difference is in terms of RA volume fraction and dislocation density, which are higher than those in carbide-free bainite (Long et al., 2017). Another aspect concerns the thickness of the bainite plates, which is lower in carbide-free bainite (Branco et al., 2018; Long et al., 2018). Finally, the volume fraction and distribution of carbides differ significantly between steels with high and low silicon content (Gulbay et al., 2023). All of these differences lead to various mechanisms during the tempering processes. As a novel aspect of this work, while most research focuses on short tempering times due to the size of samples, there is a lack of information regarding long tempering durations for large steel blocks in real industrial cases. Therefore, a better understanding of the impact of tempering time on the kinetics of bainitic phase transformation in medium carbon steels is needed. Due to the high demand for ever larger forged steel blocks, such understanding will also have industrial implications in improving the quality of the final products. The present study aims to determine the influence of tempering time on the underlying mechanisms that govern microstructure evolution.

5.3 Material and Methods

The detailed methodology employed in this chapter is described in Chapter Two.

5.4 Results and Discussion

5.4.1 Austenitization and cooling (Dilatometry)

Figure 5-1 illustrates the dilatometry curves of the two bainitic samples. It shows both the austenitization during heating and the bainitic phase transformation during the cooling process. Critical temperatures are identified from the dilatation curves by observing deviations from the tangent line, which is used in dilatometry results, and show good agreement of results (Moravec et al., 2016). The Ac_1 and Ac_3 temperatures are 790 °C and 825 °C, respectively. The B_s and B_f temperatures are 440 °C and 378 °C, respectively. These results indicate that the initial conditions for both samples prior to tempering were similar.

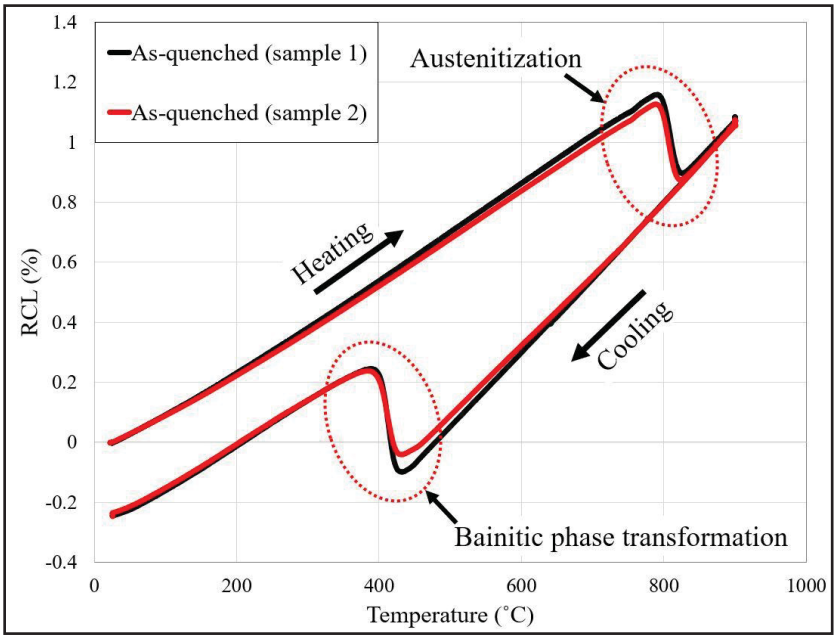

Figure 5-1 Relative change in length (RCL) as a function of temperature during austenitization and cooling of two bainitic samples before tempering

5.4.2 As-quenched bainite (Microstructure)

Figure 5-2a shows the SEM image of the bainitic microstructure after cooling to room temperature, hereafter called as-quenched bainite. The microstructure consists of a matrix of bainitic ferrite, carbides, RA, and M/A zones. Bainitic ferrite is the first phase to form during the phase transformation, as mentioned earlier. The distributed carbides result from the auto-tempering process because, during bainite formation, at high temperatures and slow cooling rates, sufficient time is available for carbon redistribution and formation of carbides (Bhadeshia, 2019). The retention of RA is due to the high concentration of carbon rejected during the transformation, which remains in a film-like and blocky morphology. However, blocky RA, being unstable, partially transforms into martensite during the final cooling from 378 °C to room temperature, forming what are commonly referred to as M/A zones (Tolouei et al., 2024; Zheng et al., 2017).

EBSD scanning was performed, as illustrated in Figure 5-2b, to provide a detailed characterization of the as-quenched microstructure to confirm the RA. In this figure, the red areas represent body-centered cubic (BCC) structures, corresponding to bainitic ferrite. The green regions indicate face-centered cubic (FCC) structures, identified as RA. The dark regions represent non-indexed areas, which are high-stress zones corresponding to M/A constituents in this sample. RA and M/A, as undesirable phases in the bainitic microstructure, can cause significant issues, particularly in mold steels (Zhang et al., 2015). Therefore, tempering is essential to eliminate or modify these phases, as will be discussed in the following sections.

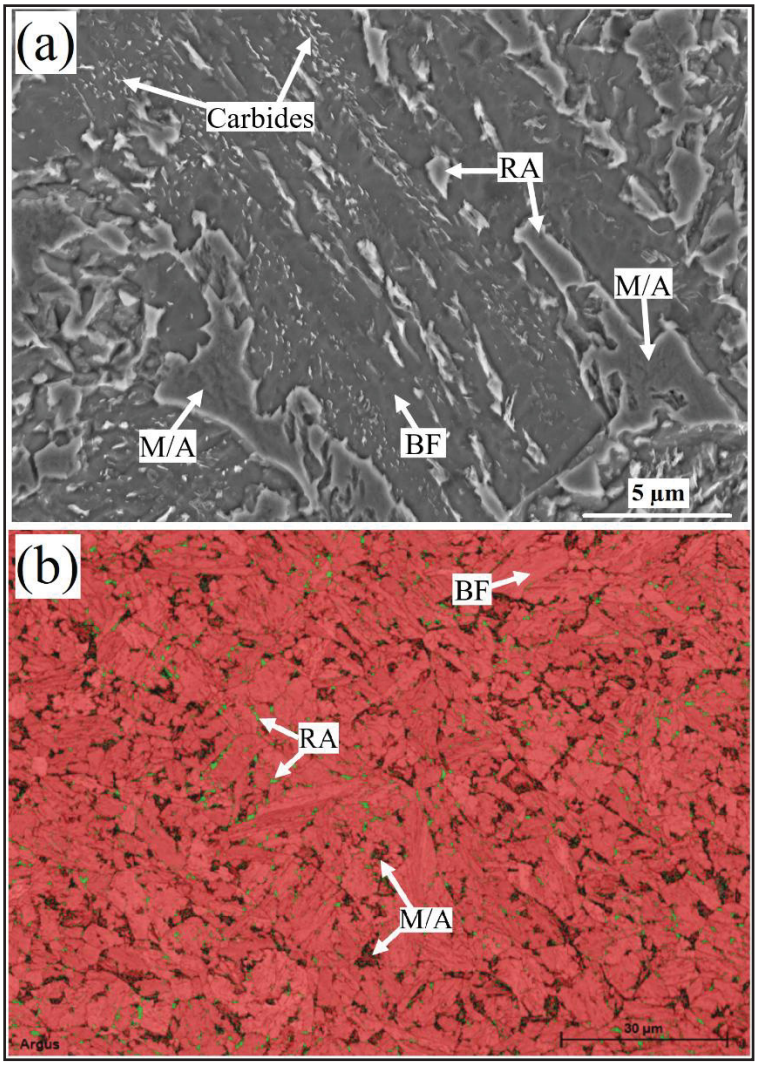

Figure 5-2 Bainitic microstructure in the as-cooled condition, (a) SEM micrograph, and (b) EBSD phase identification and band contrast map

Figure 5-3 presents the XRD pattern of the as-quenched bainitic microstructure, highlighting various peaks. The phase volume fraction analysis indicates that the RA comprises approximately 10% of the volume. By using Bragg's law, the lattice parameter of the austenite phase was calculated, and then, its corresponding carbon content was calculated in accordance with equation (5-1).

$$a(\text{Å}) = 3.57 + 0.033 \times (\text{wt\% Carbon}) \quad (5\text{-}1)$$

The carbon content of the RA in the microstructure, calculated by using the average of the four austenite peaks, was determined to be 1.06%.

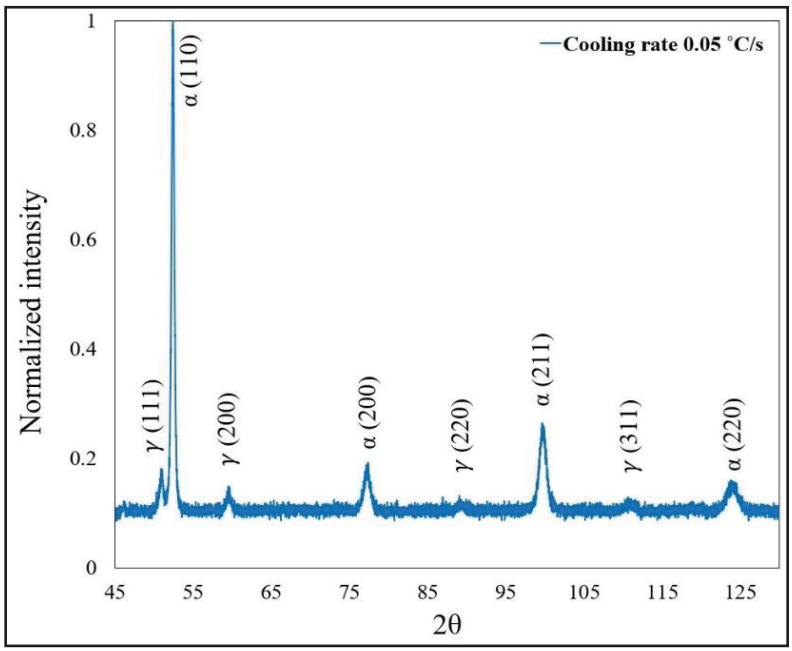

Figure 5-3 XRD patterns of the initial bainitic microstructures

5.4.3 As-tempered (Dilatometry)

Figure 5-4 illustrates the dilatometry results for the tempering process for both samples that takes place during heating to the target tempering temperature (non-isothermal tempering), as well as during isothermal conditions, and the final cooling after tempering.

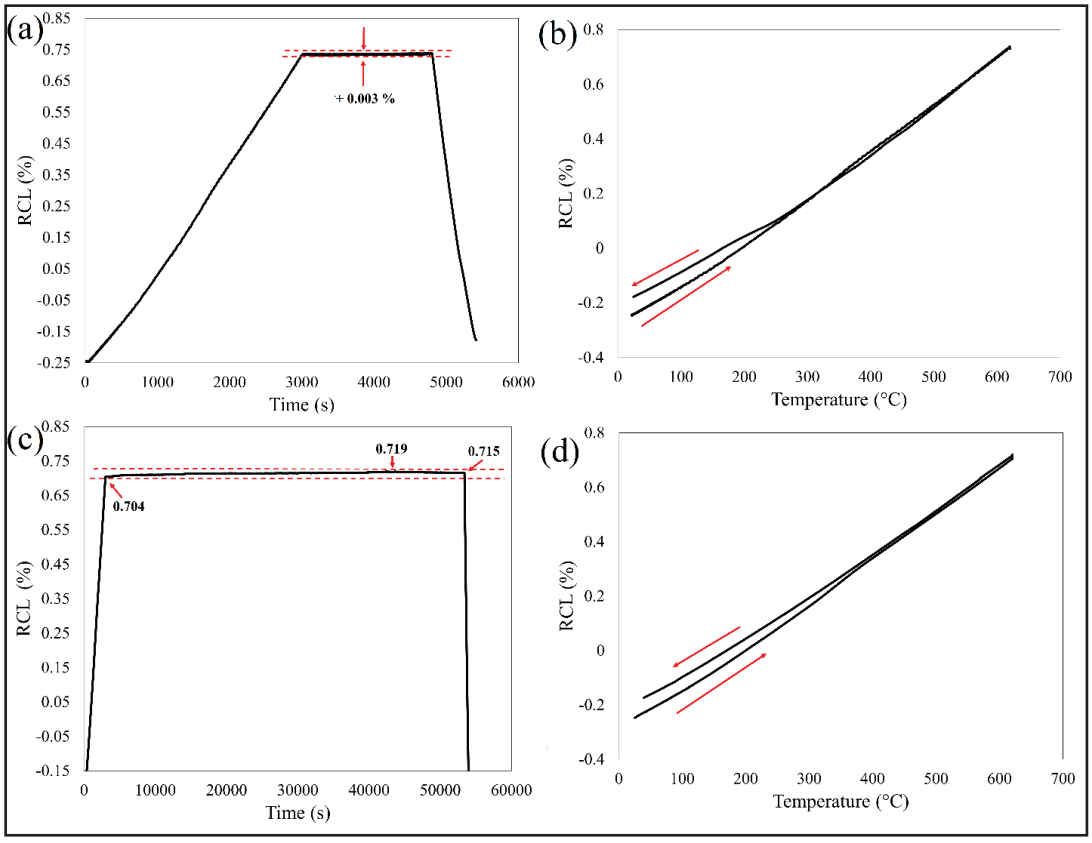

Figure 5-4 Relative change in length (RCL) during tempering: short tempering (30 min) in (a) vs. time and (b) vs. temperature; prolonged tempering (14 h) in (c) vs. time and (d) vs. temperature

Figure 5-4a show the relative change in length (RCL) during tempering for the sample held for 30 minutes, plotted versus time and temperature, respectively. Figure 5-4a indicates that, after reaching the tempering temperature (620 °C), the curve exhibits negligible expansion (ΔRCL = + 0.003 %) up to the end of the isothermal holding period, which is beyond the range of machine error. Figure 5-4c show the RCL plotted versus time and temperature, respectively, during tempering at 620 °C for 14 hours. In the sample tempered for 14 hours, the curve shows expansion up to 11 hours (ΔRCL = + 0.015 %), followed by negligible contraction during the final 3 hours (ΔRCL = - 0.004 %) (Figure 5-4c).

In bainitic microstructures, due to auto-tempering caused by slow cooling rates, some tempering processes such as (a) redistribution of carbon atoms, (b) precipitation of transition carbides, and (c) partial precipitation of cementite have already occurred (H. Bhadeshia, 2001). However, the changes observed in the dilatometric signal are consistent with the following processes that occur during bainite tempering: decomposition of blocky RA, cementite precipitation, spheroidization of rod-shaped cementite, and coarsening.

In both samples, the expansion during tempering can be attributed to RA decomposition. RA decomposition into ferrite and cementite, particularly in its blocky form, is accompanied by an expansion in length, as previously reported (Caballero et al., 2005; Talebi et al., 2018; Yan et al., 2017). In contrast, carbide precipitation results in contraction (Talebi et al., 2018; Yan et al., 2017). A review of the literature reveals that most studies have reported an initial contraction of the sample during the early stage of tempering, followed by an expansion. Ruiz-Jiménez et al. (Ruiz-Jimenez et al., 2020) attributed this initial contraction to the decomposition of film-like RA at the beginning of tempering. Since film-like RA contains a higher carbon content, it decomposes rapidly during tempering. This type of austenite has a greater driving force for carbide precipitation compared to blocky RA, owing to its higher carbon content (H. K. D. H. Bhadeshia, 2001). The subsequent expansion was attributed to the decomposition of the remaining blocky RA. Similar results have been reported by other researchers (Franceschi et al., 2024; Lerchbacher et al., 2013). In contrast, Yan et al. (Yan et al., 2017) observed expansion during the initial stage of bainitic tempering (at 400 °C and 600 °C), followed by a slight contraction in the final stage. They attributed the initial expansion to RA decomposition, and the final contraction to matrix recovery. These two distinct tempering behaviors of bainitic microstructures can be explained by differences in the chemical composition of the steels. In steels that exhibit initial contraction followed by expansion, the silicon content is relatively high. On the other hand, the expansion followed by slight contraction reported by Yan et al. was observed in a medium-carbon low-alloy steel. It can be suggested that in high-silicon steels, the inhibition of carbide precipitation and the higher volume fraction of film-like RA result in a greater rate of carbide precipitation during the early stage of tempering, leading to an initial contraction. However, in medium-carbon low-alloy

steel with lower Si content, a large proportion of RA is present in blocky form; therefore, tempering initially causes expansion.

Figure 5-5 presents the dilatometry results during final cooling to room temperature. In the sample tempered for 30 minutes, a change in the slope of the RCL curves is observed at 250°C; however, the sample tempered for 14 hours did not reveal any change in slope. To enhance clarity, the derivative of the RCL data (DRCL) was also calculated and included in this figure. A peak is observable here, which is attributed to the formation of FM during the final cooling, a process known as indirect decomposition of RA. Sourmail et al. (Sourmail et al., 2021) report that indirect RA decomposition occurs in two situations: during low-temperature tempering or when the tempering time is insufficient to complete direct transformation. In medium-carbon low-alloy steel, Talebi et al. (Talebi et al., 2018) reported that even tempering up to 550 °C results in FM formation during the final cooling after 16 hours. Additionally, Podder et al. (Saha Podder & Bhadeshia, 2010) reported that even 30 minutes of tempering leads to the precipitation of cementite from the RA, which decreases its carbon concentration and ultimately causes its destabilization and transformation into FM during the final cooling. Comparing the carbon content of RA before tempering and the unstable RA transformed into FM confirms similar results. The RA carbon content calculated from XRD results and equation 2 in the previous section showed that the average was 1.06 %. In order to calculate the RA carbon content transformed into FM, the empirical equation reported by Tamura (I, 1970) was found to best match the M_s temperature of the studied steel (350 °C) (Hurel, 2022). By applying (5-1) and an M_s temperature of 250 °C, the carbon content of the austenite was determined to be approximately 0.4%.

$$M_s = 550 - 361X_C - 39X_{Mn} - 20X_{Cr} - 5X_{Mo} - 34X_{Ni} - 30X_{Al} + 15X_{Co} - 10X_{Cu} - 35X_V \qquad (5\text{-}1)$$

The carbon content of RA, calculated from XRD results before tempering, was approximately 1.06%, while the carbon content of FM formed during final cooling to room temperature was

estimated at around 0.4%. This supports the assumption that, carbide precipitation occurs in RA during the early stages of tempering, followed by RA indirect decomposition into FM.

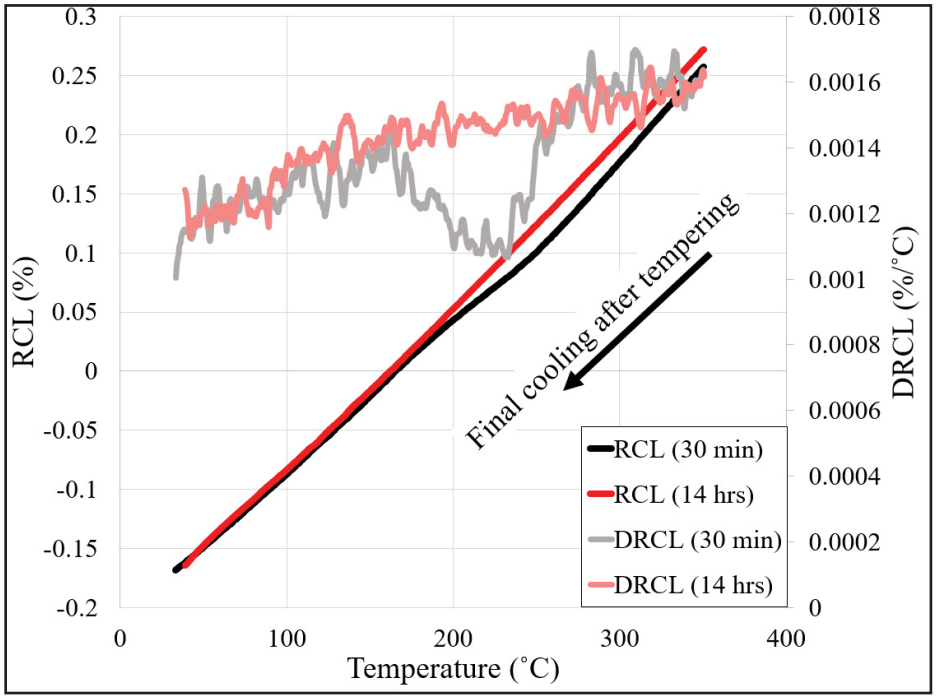

Figure 5-5 Relative change in length (RCL) and the derivative of RCL (DRCL) as a function of temperature after tempering for both holding times (30 minutes and 14 hours)

5.4.4 As-tempered (Microstructure)

Figure 5-6 shows SEM micrographs of the microstructure after 30 minutes tempering. Figure 5-6a illustrates the microstructure following 30 minutes of tempering, characterized by uniformly distributed small carbides within the BF matrix, aggregated carbide zones (AC), FM, and elongated carbides (EC). As seen in Figure 5-6c, block of FM, which aligns with the dilatometry results presented in Figure 5-5. The main difference between the initial microstructure and the one tempered for 30 minutes is the transformation of the M/A zones into AC zones, and the formation of elongated carbides.

The morphology of the carbides formed during the evolution of M/A constituents in tempering consists of randomly oriented rod-like carbides and small spherical carbides (Figure 5-6b). It should be noted that the boundaries of the aggregated carbide zones are visible, as shown in Figure 5-6a and 8b. The formation of aggregated carbide zones as a result of the M/A constituents decomposition during tempering has been reported in the tempering of low-carbon low-alloy steels (Jiang et al., 2021; C. W. Li et al., 2016; B. Wang et al., 2023). The main factor contributing to the formation of a high volume of carbides during the tempering of M/A is the higher carbon content in these zones, as demonstrated by Jian et al. (Jiang et al., 2021) who utilized electron probe microanalysis. During tempering, the M/A constituents decompose, leading to the formation of two types of aggregated carbide zones: string-like carbides and randomly oriented carbides, as reported by Wang et al. (B. Wang et al., 2023). The carbides formed during the decomposition of M/A have been identified as cementite (Jiang et al., 2021; B. Wang et al., 2023).

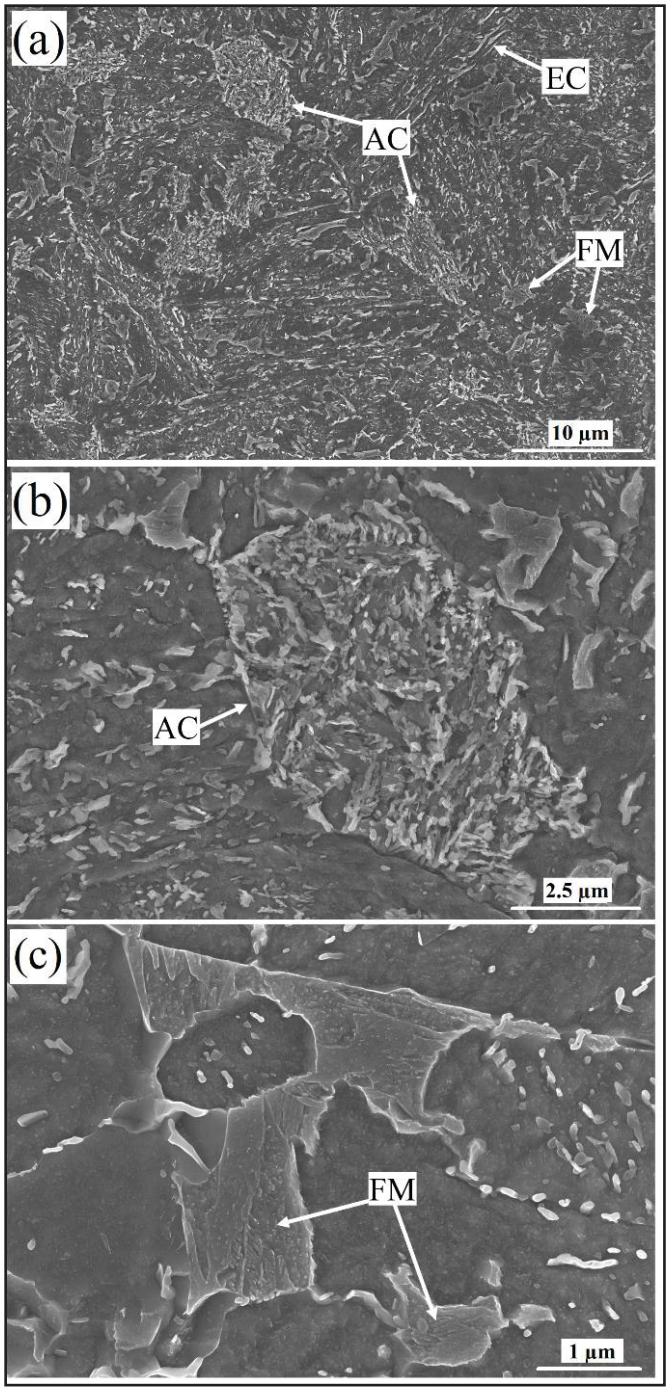

Figure 5-6 SEM images of the sample after 30 minutes of tempering: (a) general microstructure, (b) aggregated carbide zone, and (c) fresh martensite. AC: aggregated carbide, FM: fresh martensite, EC: elongated carbide

Figure 5-7 shows the microstructure after 14 hours tempering. Figure 5-7a and b show that, due to prolonged tempering, the boundaries of the aggregated carbide zones become more

blurred compared to the 30-minute tempering condition. Some locally coarsened carbides are observed in the microstructure, although no significant change in overall carbide size is evident (Figure 5-7b). Additionally, Figure 5-7c shows elongated carbides with lengths of 2–5 μm precipitated at the grain boundaries, and between the bainitic ferrite plates. While the morphology of the carbides has transformed into a spherical form, rod-like carbides are still present. No evidence of RA, M/A zones, or blocky FM is present in this microstructure. This finding corroborates the dilatometry results, which show expansion due to RA decomposition followed by contraction (Figure 5-4), and no indication of FM formation during final cooling (Figure 5-5).

Due to local coarsening at the boundaries of the aggregated carbide zones, the boundaries become more diffuse. As reported by Li et al. (C. W. Li et al., 2016), tempering at higher temperatures leads to blurrier M/A zone boundaries and enhanced carbide accumulation. Negligible spheroidization of carbides was observed during tempering, which may be attributed to a reduction in surface energy. However, in medium-carbon low-alloy steels, it has been reported that spheroidization takes place without a change in the number of carbides per unit area (Bush & Kelly, 1971). Bhadeshia (H. Bhadeshia, 2001) reported a negligible change in cementite size even after prolonged tempering at high temperature in medium-carbon low-alloy steel, due to the high stability of the bainitic microstructure.

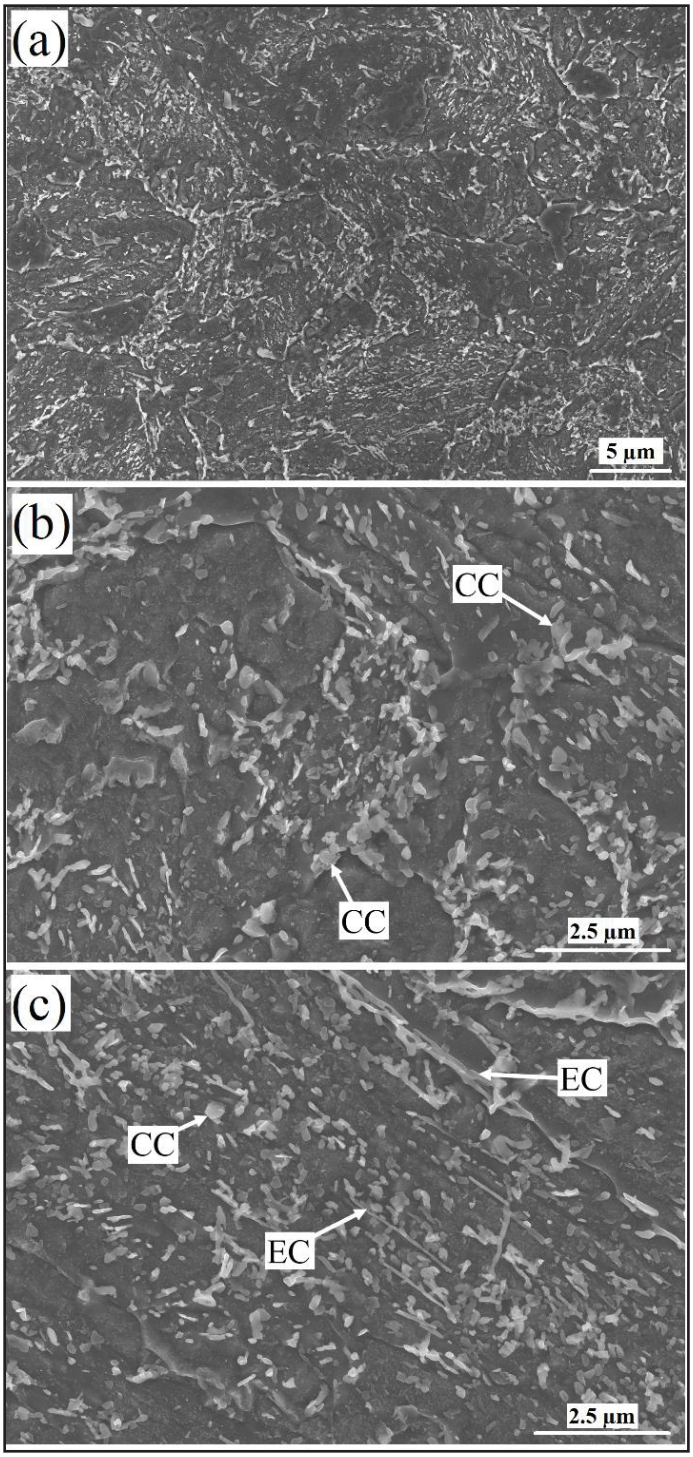

Figure 5-7 SEM images of sample after 14 hours of tempering: (a) general microstructure, (b) locally coarsened carbides, and (c) elongated carbides at the boundaries. CC: coarsened carbide; EC: elongated carbide

To analyze the volume fraction of FM zone, grain boundary density, and bainitic block thickness in detail, EBSD images were captured from the samples after tempering. Figure 5-8(a-b) presents a superimposition of the phase EBSD map and band contrast images for the samples tempered for 30 minutes and 14 hours, respectively. Figure 5-8a shows microstructure, including bainitic ferrite zone (red), RA (green), and martensite (dark regions as non-indexed areas). The volume fraction of RA is negligible (2.5%), although some RA is observable at the boundaries. The non-indexed areas on the EBSD maps have been interpreted as high carbon martensitic regions or aggregated carbide (AC) zones (Knijf et al., 2014; Tolouei et al., 2024). To confirm the nature of the non-indexed zones, the samples were etched after EBSD, and SEM analysis was performed at the same locations. Figure 5-8c shows the selected non-indexed zone in Figure 5-8a. As evident, the SEM shows the fresh martensite block formed, as explained in the previous section (Sourmail et al., 2021). The poor crystallographic intensity indexing in these areas is due to increased noise from internal strains and dislocations (Baek et al., 2020; Knijf et al., 2014). In comparison to RA, the volume fraction of martensitic zones (non-indexed) is significantly high. Based on image analysis using ImageJ software (Schneider et al., 2012), the volume fraction of the martensitic zones after 30 minutes of tempering was determined to be approximately 16%.

Figure 5-8b shows the microstructure after 14 hours of tempering, where a uniform bainitic microstructure with no RA and minimal non-indexed zones was observed. Based on the obtained results, it appears that sufficient tempering time leads to complete RA decomposition, confirming the dilatometry results, and prevents the indirect decomposition of RA into FM during final cooling after tempering, as discussed in the previous section. ImageJ analysis revealed that for this condition, the non-indexed area decreased significantly to less than 2%, compared to 30 minutes tempering (Figure 5-8a). The same method was used to check the microstructure of the selected non-indexed zone in Figure 5-8b. Figure 5-8d shows zones with a high density of carbides. Regions with a high carbide density also exhibit poor band contrast in the EBSD images (Tolouei et al., 2024).

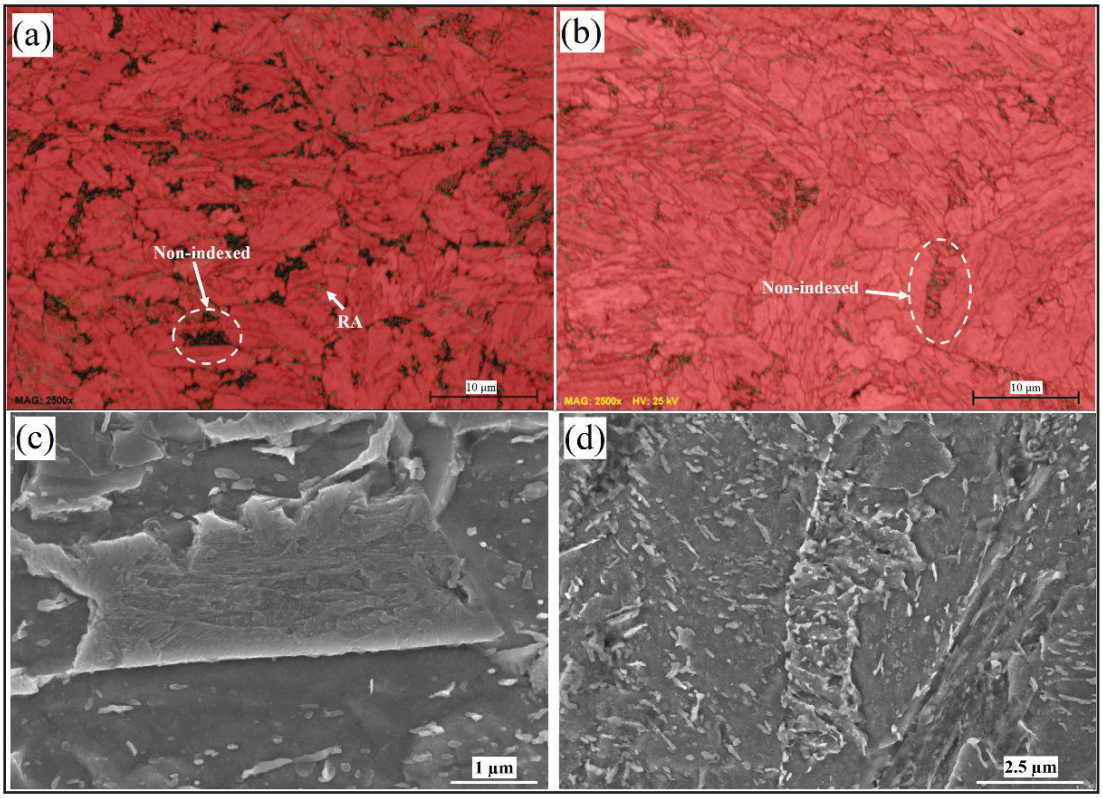

Figure 5-8 Superimposition of phase EBSD map and pattern quality of samples after tempering; 30 minutes (a), and 14 hours (b). SEM images (c) and (d) correspond to the selected non-indexed zones in the EBSD maps shown in (a) and (b), respectively

Figure 5-9 presents EBSD grain boundary maps overlaid on pattern quality images for samples subjected to the two tempering times. It should be noted that, to ensure an accurate comparison, the magnification, resolution, step size, and voltage of the EBSD processes were kept constant for both samples. The calculated volume fractions of different grain boundary types, derived from the EBSD results, are summarized in Table 5-1. Grain boundaries are classified based on the misorientation between adjacent grains: low-angle grain boundaries (LAGBs) with misorientations <15°, and high-angle grain boundaries (HAGBs) with misorientations >15° (Humphreys & Hatherly, 2004). Figure 5-9a and b and the data in Table 5-1 indicate that the LAGBs volume fraction decreases significantly, from 62.9% to 31.7%, as the tempering time increases from 30 minutes to 14 hours, while the number of HAGBs increases. As reported by Ni et al. (Ni et al., 2025), this phenomenon occurs because LAGBs form through dislocation movement during the tempering process and gradually evolve into HAGBs.

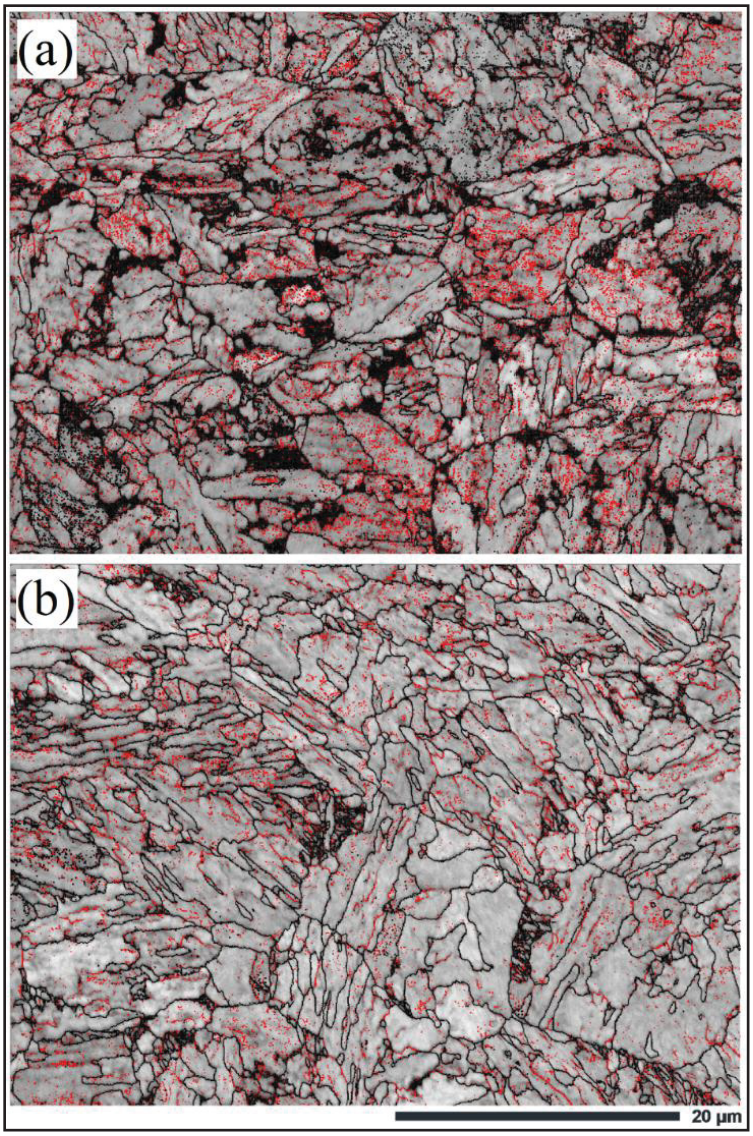

Figure 5-9 EBSD grain boundary maps imposed on the pattern quality maps from Figure 5-8: 30 minutes (a), and 14 hours (b)

Table 5-1 Volume fraction of low-angle and high-angle grain boundaries after different tempering times

Min/Max Ang (°)		**Color**	**30 minutes (%)**	**14 hours (%)**
2	15		62.9	45.2
15	63.5		37.1	54.8

5.4.5 Thermodynamic stability of the carbides

The main carbides in the microstructure were elongated at boundaries and rod-like and spherical inside the BF blocks. There is a correlation between the morphology of the carbides and their type. Figure 5-10 shows the most stable carbides at the tempering temperature of 620 °C based on thermodynamic calculations using Thermo-Calc software. The calculations in Figure 5-10a indicate that, at the tempering temperature, $M_{23}C_6$ and M_7C_3 are the most stable carbides based on the chemical composition of the steel, which is consistent with the findings reported in the literature (Talebi et al., 2018). Masaki et al. (Taneike et al., 2004) reported that $M_{23}C_6$ predominantly precipitates at grain boundaries. By increasing tempering time, the growth of $M_{23}C_6$ carbides leads to the dissolution of adjacent, less stable M_2C and M_7C_3 carbides (Dépinoy et al., 2017). It should be noted that, as observed in the SEM image after 14 hours of tempering (Figure 5-6b), elongated carbides predominantly formed at the grain boundaries. Zheng et al. (Zheng et al., 2019) reported that M_7C_3-type carbides are prone to precipitate in the matrix in the form of round bars. Therefore, the most probable form of elongated carbides at the grain boundaries is $M_{23}C_6$, while the rod-like and spherical carbides inside the bainitic ferrite plate are M_7C_3. However, it must be emphasized that the Thermo-Calc calculation represents the Gibbs free energy of the system under equilibrium conditions, whereas tempering is a non-equilibrium process, due to the short holding time. Therefore, while the experimentally observed carbides correspond well with the thermodynamically predicted ones; their mole fractions may differ (Zheng et al., 2019).

Additionally, transmission electron microscopy of a similar steel tempered for 16 hours at 600 °C confirmed the precipitation of Cr_7C_3 and $Cr_{23}C_6$ (Talebi et al., 2018). Figure 5-10b and c show that Fe and Cr are the primary elements in the $M_{23}C_6$ and M_7C_3 carbides in the range of tempering temperature. The relatively low weight percentage of Cr in this steel may contribute to the stability of Fe. Using transmission electron microscopy and Thermo-Calc calculations on a similar steel, Zhang et al. (Zheng et al., 2019) found Fe to be the predominant element in $M_{23}C_6$. On the other hand, Figure 5-10c illustrates the greater stability of chromium in M7C3. The stoichiometry and chemical composition are likely the key factors influencing the stability of the elements in the carbides. The driving force for the precipitation of M_7C_3 is greater than

that for $M_{23}C_6$ when the chromium content is below 2 wt.% (Zhou et al., 2020). In conclusion, it can be stated that the carbides formed after tempering in this steel may consist of a combination of stable M_7C_3 within the grains and typically elongated $M_{23}C_6$ at the grain boundaries. Fe and Cr are the primary contributing elements, after prolonged tempering.

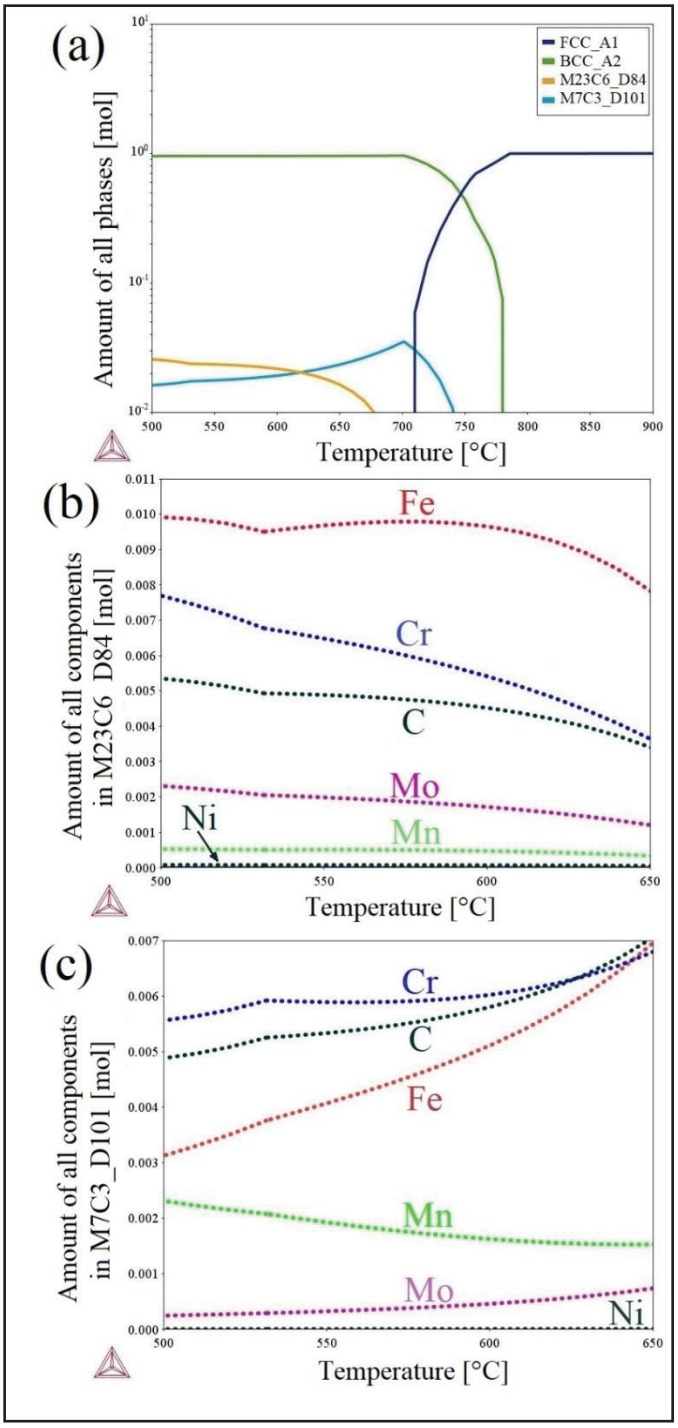

Figure 5-10 Phase stability of steel (a), and the stability of elements within $M_{23}C_6$ (b) and M_7C_3 (c) phases, as determined using Thermo-Calc

5.4.6 Hardness measurements

5.4.6.1 Micro-hardness

Figure 5-11 presents the average micro-hardness measurements of two samples after quenching and following different isothermal holding times at 620 °C. The results indicate that 30 minutes tempering has no affect the microstructural recovery or hardness reduction. However, 14 hours tempering leads to a significantly decreased hardness, from 370 to 300 HV. The FM formation after 30 minutes of tempering led to slight increases in the average hardness. In contrast, with longer tempering times, the hardness decreases by 19% compared to the as-quenched bainite due to lack of FM, complete RA decomposition, and significant decrease of dislocation density, as observed in Figure 5-9. Several factors influence the refinement of the microstructure during the tempering process. However, for bainitic microstructures, changes in plate thickness are minimal, and the most significant factor is the reduction in the dislocation density (Ståhlkrantz et al., 2020).

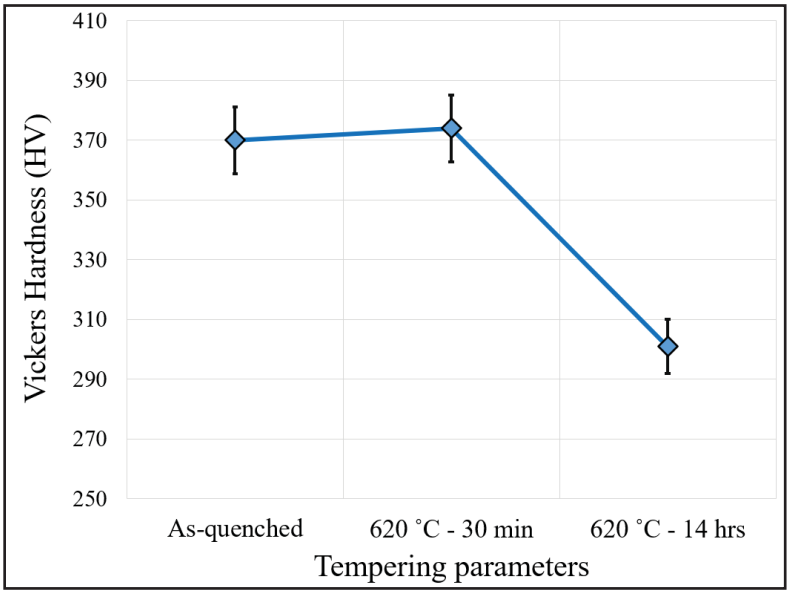

Figure 5-11 Vickers hardness measurements after different tempering times

5.4.6.2 Nanohardness

To compare the hardness of different zones in the sample after 30 minutes of tempering, nanoindentation tests were conducted. Due to the small size of the microstructural features, accurately targeting specific zones for hardness measurements was challenging. Figure 5-12 shows typical SEM images after nanoindentation on the fresh martensitic zone (a), aggregated carbides zone (b), and bainitic zone (c). A total of 30 nanoindentations were performed, from which 9 indentations that were completely located within the targeted zones were selected for analysis. Figure 5-12d displays the load-displacement curves for these nine indentations across the three zones. The average nanohardness values were 5.8 ±0.07 GPa for FM, 4.0 ± 0.8 GPa for bainite, and 3.2 ± 0.5 GPa for AC. As expected, the highest hardness was observed in the FM zone. FM blocks typically exhibit higher carbon content and greater local misorientation, which can contribute to their increased hardness (Knijf et al., 2014; Saha Podder & Bhadeshia, 2010). Based on Figure 5-8, the 16% FM distributed in the entire microstructure (with its high hardness) can be considered as one of the main factors contributing to the increased hardness after tempering.

According to the literature, experimental results indicate that the hardness of metallic carbides can range between 10 and 20 GPa (Gorunov, 2020). Therefore, high hardness was expected in the AC zone due to its carbide content. However, the results showed the opposite trend. This discrepancy may be attributed to the porosity in these regions. As seen in Figure 5-12b, numerous voids exist between the carbide regions. It appears that during etching, the matrix was corroded while the carbides remained intact. Consequently, during nanoindentation, the indenter may have displaced material into these gaps, preventing accurate hardness measurements of the carbides themselves. It is also noteworthy that the hardness values in the BF zone showed significant variation. This could be related to the fact that the nanohardness values for each phase may reflect an inhomogeneous distribution of chemical composition, variations in dislocation density, and/or the influence of underlying microstructural features or interactions between different phases during indentation (Taylor et al., 2014).

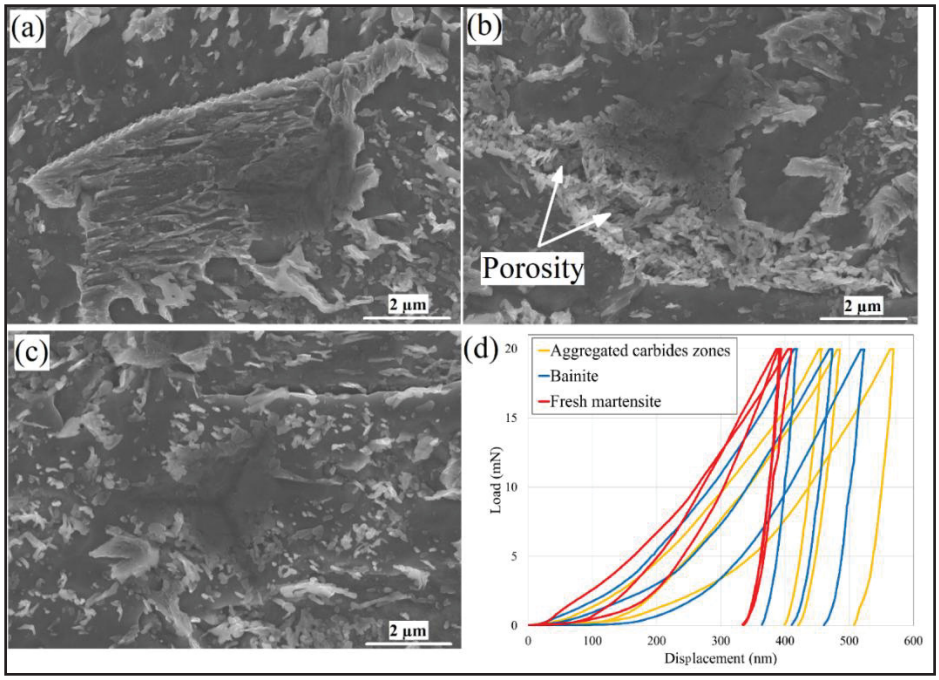

Figure 5-12 Nanoindentation on different zones (a) fresh martensite, (b) aggregated carbides zones, (c) bainite, and (d) load-displacement curves

5.5 Conclusions

This study has examined the effects of short and long tempering times at a specific temperature to compare the resulting microstructure and hardness of bainitic mold steel. The following main conclusions can be drawn from this study:

- Long tempering times in bainitic mold steel result in negligible changes in carbide size and morphology, but a significant reduction in low-angle grain boundaries.
- Nanoindentation results show significant differences in local hardness of bainitic ferrite compared to fresh martensite and aggregated carbide zones. Formation of blocky fresh martensite leads to increased hardness in short tempering times.
- Evolution of martensite-austenite constituent during tempering results in the formation of aggregated carbide zones.

- The results show that, in industrial practice, non-isothermal tempering of large steel blocks produces noticeable differences between the surface and center microstructures, indicating that the starting microstructure for an isothermal tempering process differs significantly across the block.

5.6 Chapter Summary and Outlook

Tempering represents one of the most challenging stages in the heat treatment of mold steels because of the large block thickness. Accordingly, this chapter examines the impact of temperature non-uniformity on microstructure evolution during non-isothermal tempering. These results highlight the complexity and critical importance of heat treatment in this class of steels, demonstrating that it takes more than 10 hours for the block center to reach the target temperature, whereas the surface experiences tempering throughout this time. The results confirm a significant effect of tempering time on microstructure and hardness.

The next chapter is based on the results reported in chapter 4, with slow cooling after isothermal holding. Slow cooling was selected to simulate industrial conditions, as the large thickness of the blocks results in a delayed cooling rate after removal from the bath.

CHAPTER 6

Influence of slow cooling rate following isothermal bainitic transformation on the microstructure and hardness of mold steels

Ehsan Tolouei[a], Jean-Benoit Morin[b], Carlos Garcia-Mateo[c], and Mohammad Jahazi[a]*

[a] Department of Mechanical Engineering, École de Technologie supérieure (ETS), 1100 Notre-Dame St. W, Montreal, QC, H3C 1K3, Canada

[b] Finkl Steel-Sorel, 100 McCarthy, Saint-Joseph-de-Sorel, QC, J3R 3M8, Canada

[c] Department of Physical Metallurgy, National center for metallurgical research (CENIM-CSIC), Materalia Research Group, Avenida Gregorio Del Amo, 8, Madrid, 28040, Spain

* Corresponding author: Mohammad.Jahazi@etsmtl.ca, Tel: +1-514-396-8974, Fax: +1-514-396-8800

6.1 Abstract

This study examines the effects of slow continuous cooling (0.05 °C/s) after 3-hour isothermal bainitic transformation (austempering) at 380–450 °C on the microstructure, phase fractions, kinetics, and hardness of a medium-carbon low-alloy steel, using high-resolution dilatometry, SEM, XRD, and Vickers testing. The steel was austenitized at 900 °C (heating at 5 °C/s), then cooled at 2 °C/s to austempering temperatures. No bainitic transformation occurred during holding at 450 °C; instead, continuous bainite formed during subsequent slow cooling. Higher austempering temperatures (up to 425 °C) reduced the bainite fraction, increased martensite content (up to 56 vol.% confirmed by dilatometry and SEM), and raised hardness to 438 HV (versus ~410 HV at lower temperatures). Compared to fast cooling (10 °C/s) from a prior study, hardness increased significantly only at 425 °C. Lower austempering temperatures accelerated

bainitic kinetics across incubation, peak rate, and sluggish stages. Retained austenite remained <10 vol.% across conditions, unaffected by cooling rate.

Keywords-component; Austempering temperature; retained austenite; slow cooling; kinetic

6.2 Introduction

Modified P20 mold steels have gained recent industrial interest for plastic injection molding applications, such as dashboards and bumpers. Conventional quenching and tempering (Q&T) is time-intensive, yielding predominantly bainitic microstructures in large ingots due to slow cooling; bainite's superior properties have drawn attention (Y. Li et al., 2016). Austempering is increasingly adopted for smaller blocks to cut time and costs (Tolouei, Saadati, et al., 2025), with key parameters including austenitization, prior cooling rate, austempering temperature/time, and final cooling rate dictating microstructure and properties.

Literature extensively covers austempering temperature/time (Liu et al., 2020; Su et al., 2022) and prior cooling (Gao et al., 2022; X. Long et al., 2023; Park et al., 2022), which can form pearlite/ferrite and alter kinetics/properties. Final cooling rate is critical for thick components, where slow rates enable carbon partitioning from bainitic ferrite to austenite (H. Bhadeshia, 2001), stabilizing retained austenite (RA) or forming martensite-austenite (M-A) constituents at lower temperatures (Sourmail et al., 2021). Slow cooling may also promote bainite tempering via carbon diffusion or carbide precipitation (Ruiz-Jimenez et al., 2020).

This study addresses the underexplored impact of slow final cooling (0.05 °C/s versus 10 °C/s in (Tolouei, Saadati, et al., 2025) after austempering, simulating industrial thick-section conditions. It investigates combined effects of austempering temperature and slow cooling on microstructure, kinetics, and hardness.

6.3 Material and Methods

The detailed methodology employed in this chapter is described in Chapter Two (2.2.1.2).

6.4 Results and discussion

6.4.1 Dilatometry results

Figure 6-1 shows the relative change in length (RCL) recorded over the complete heat treatment cycle for all conditions investigated. The Ac1 and Ac3 temperatures, corresponding to the onset and completion of austenitization, were determined as 780 °C and 825 °C, respectively, from the beginning and end of the contraction observed during heating to 900 °C in the dilatometric curves. The subsequent linear contraction on cooling to the austempering temperature, Figure 6-1, confirms that no intermediate diffusional transformations, such as ferrite or pearlite, occurred prior to reaching the isothermal holding temperature.

Upon reaching the austempering temperatures, a dilatometric expansion was detected in all cases except at 450 °C, indicating the occurrence of bainitic transformation. The larger RCL reflects the volume increase associated with the transformation of austenite into bainitic ferrite. In contrast, during isothermal holding at 450 °C, no expansion was observed, showing that the bainitic reaction does not proceed at this temperature within the holding time employed. Consequently, during the subsequent slow cooling to room temperature at 0.05 °C/s, the austenite transforms by continuous-cooling bainite formation, starting at 407 °C and finishing at 350 °C, in agreement with (Hurel, 2022). This interpretation is further supported by the quench experiment in Figure 6-1, where a cooling rate of 5 °C/s produced only martensite, with a martensite start temperature of approximately 348 °C, clearly below the 407 °C transformation start detected in the sample initially held at 450 °C.

It is also evident from Figure 6-1 that, after bainitic transformation, all samples exhibit an additional expansion during the final cooling to room temperature, which is attributed to the transformation of carbon-enriched retained austenite into martensite (Tolouei, Hurel, et al., 2025). To analyse this stage in more detail, Figure 6-2 presents the final cooling segments for each condition.

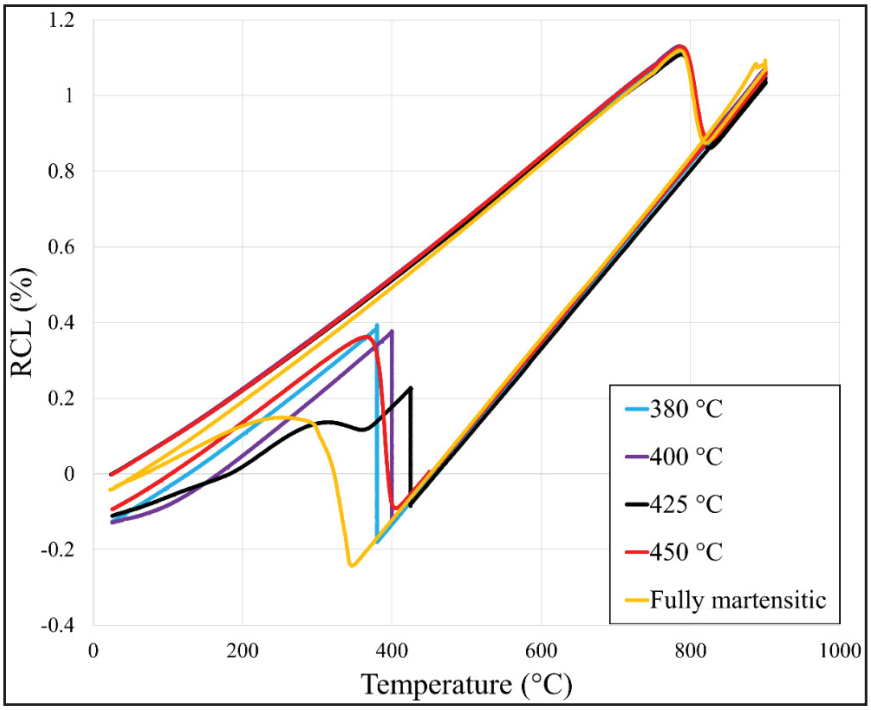

Figure 6-1 Relative length change versus temperature for the entire heat treatment cycle

For the samples isothermally held at 380 °C and 400 °C, the onset of final-stage dilation occurs at 133 °C and 160 °C, respectively (Figure 6-2a,b). As previously reported, a higher bainite fraction formed at lower austempering temperatures promotes more extensive carbon partitioning into the remaining austenite, which increases its carbon content and reduces the martensite start temperature (Franceschi et al., 2021; Tian et al., 2018).

For the sample held at 425 °C, two distinct dilation events are observed during the final cooling: the first begins at 368 °C and ends at 282 °C, followed by a second expansion starting at 182 °C (Figure 6-2c). Owing to the higher austempering temperature, the overall expansion during the isothermal stage is lower than for 380 °C and 400 °C, indicating a reduced bainite fraction and a correspondingly higher fraction of residual austenite. The presence of two separate expansions during final cooling suggests a heterogeneous carbon distribution within the residual austenite. The Ms temperature of the material, for the same austenitization conditions and a cooling rate of 5 °C/s, is 348 °C (Figure 6-3, yellow curve). Therefore, the transformation starting at 368 °C is unlikely to be martensitic and is instead attributed to bainite

formation during continuous cooling, whereas the subsequent transformation at 182 °C is assigned to martensite formation. For the sample held at 450 °C, martensitic transformation occurs at the lowest temperature, around 90 °C, consistent with the high carbon content and associated stability of the retained austenite (Figure 6-2d).

To quantify the martensite fraction formed during the final cooling stage, the method proposed by Morawiec et al. (Morawiec et al., 2022) was applied. In this approach, the dilatometric response of the specimen previously quenched from 900 °C at 5 °C/s, already identified as fully martensitic with an Ms temperature of 348 °C (yellow curve in Figure 6-1 and Figure 6-3), is used as the 100% martensite reference. Although a small amount of retained austenite (up to ≈3 vol.%) may remain, it is below the XRD detection limit and does not affect the calibration. As shown in Figure 6-3, the RCL associated with full martensitic transformation corresponds to the difference between the dashed lines representing the thermal contraction of fully austenitic and fully martensitic states (double arrow). The RCL measured for the other specimens was compared with this reference, and the martensite volume fraction was obtained by scaling to the reference RCL.

The calculations indicate that the maximum martensite fraction formed during final cooling is 45% for the sample held at 425 °C and 11.6% for the one held at 400 °C. The lowest fractions are found for the samples held at 380 °C and 450 °C, with martensite contents of 4% and 5.7%, respectively. These results show that, in terms of martensite formed during final cooling, there is no significant difference between the microstructure generated by isothermal bainitic transformation at 380 °C and that produced by continuous-cooling bainite in the sample held at 450 °C.

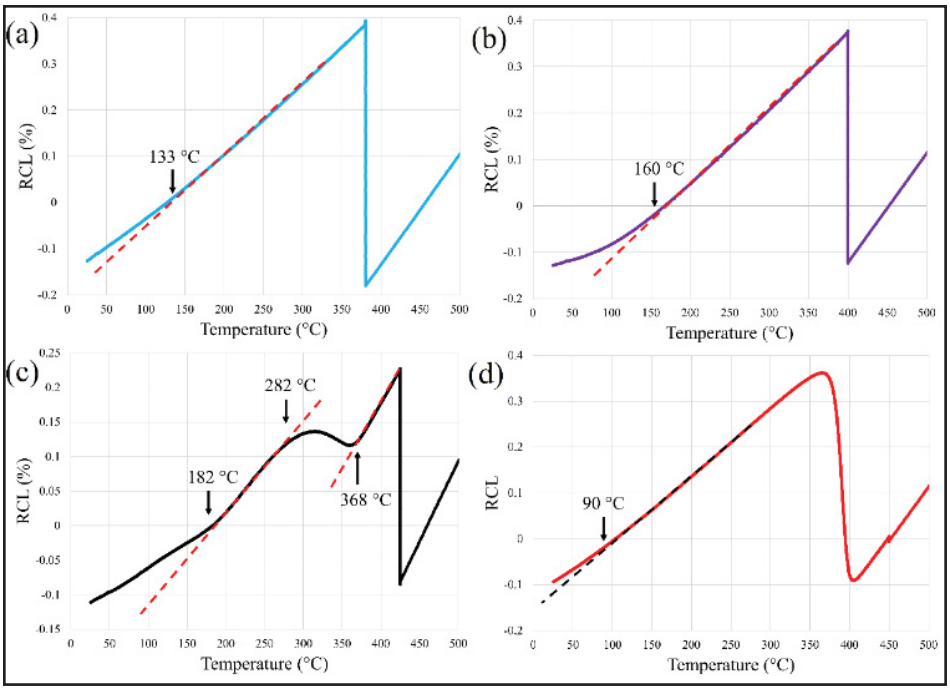

Figure 6-2 Relative change in length as a function of temperature for the dilatometry specimens, including phase transformation and subsequent cooling to room temperature: (a) 380 °C, (b) 400 °C, (c) 425 °C, and (d) 450 °C

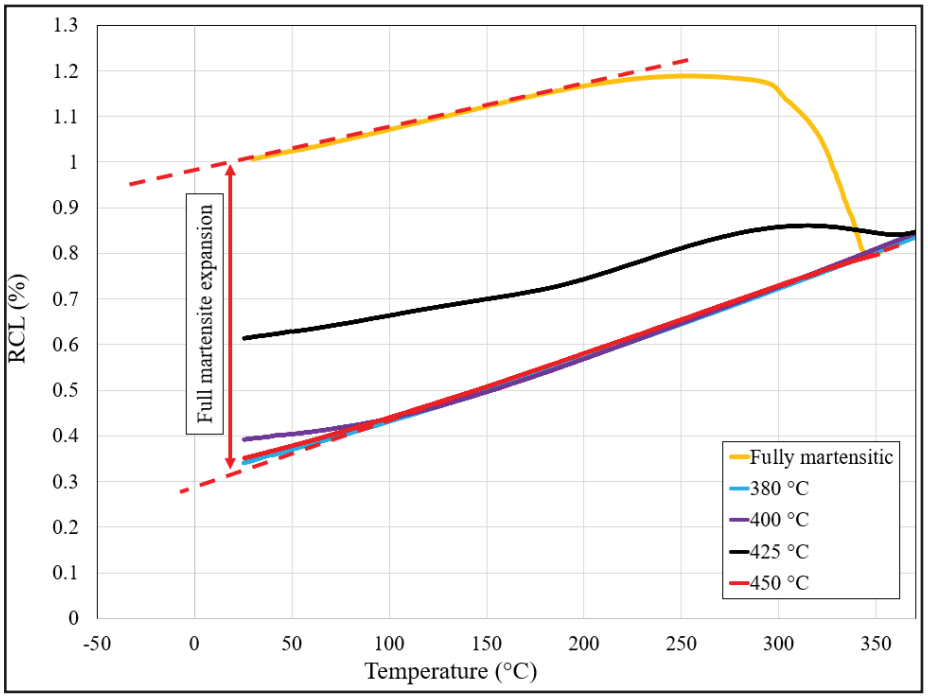

Figure 6-3 Determination of the martensite fraction based on the relationship between relative length change and temperature during cooling to ambient temperature

6.4.2 Phase and microstructure analysis

In order to quantify the phases, present in each heat-treated condition, the retained austenite (RA) volume fraction (VRA) at room temperature was measured by X-ray diffraction (XRD), as described in the corresponding section, with the corresponding values listed in Table 6-1. The bainite volume fraction was then calculated as 100 − (VRA + VM), where VM was determined and presented in the previous section. Figure 6-4 shows the XRD patterns for all thermal treatments, revealing the same phases (ferrite, corresponding to the bainite/martensite matrix, and austenite) with comparable peak intensities for all conditions. Isothermal treatments at 380 °C and 400 °C yield RA fractions of 4.4% and 8.2%, respectively, whereas austempering at 425 °C and 450 °C both result in 6.4% RA; in all cases, the RA content remains below 10 vol.%. The data from Tolouei et al. (Tolouei, Saadati, et al., 2025), obtained for a higher final cooling rate of 10 °C/s after identical austempering treatments, are given in the last column of Table 6-1 and indicate that decreasing the final cooling rate from 10 °C/s to 0.05 °C/s does not noticeably affect the amount of stable RA at room temperature.

Figure 6-5 presents SEM micrographs of the microstructures obtained at the four austempering temperatures. The observed morphologies are consistent with the dilatometric and XRD results, showing a bainitic matrix (dark grey) containing irregularly distributed martensitic islands (light grey). The sample held at 380 °C (Figure 6-5a) exhibits the lowest martensite fraction and a predominantly bainitic microstructure. The microstructures corresponding to 400 °C and 425 °C (Figure 6-5b,c) reveal an increasing martensite fraction with increasing austempering temperature, in agreement with the martensite fractions derived from dilatometry. The continuously cooled sample (450 °C, Figure 6-5d) displays a bainitic morphology similar to that of the 380 °C condition, despite the different transformation path, which is consistent with the similar martensite volume fractions reported in Table 6-1.

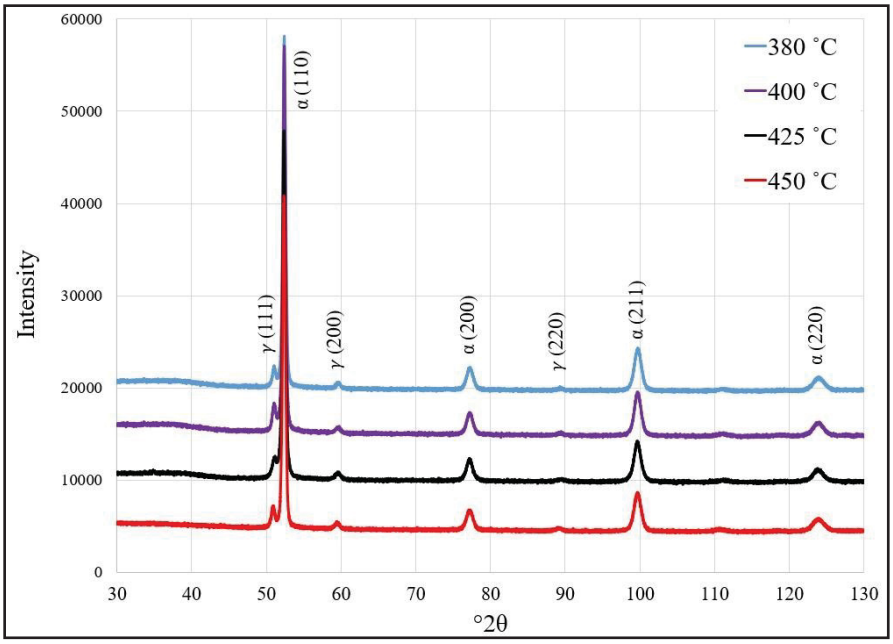

Figure 6-4 XRD results for samples treated at different austempering temperatures

Table 6-1 Volume fraction (%) of phases present at the microstructure after different isothermal holding temperatures (measurement error ±3%)

Isothermal temperature (°C) final cooling rate 0.05 °C/s	V_{RA}	V_M	V_B	V_{RA} *(Tolouei, Saadati, et al., 2025)*
380	4.4	4	91.6	6.4
400	8.2	11.6	80.2	7
425	6.4	45	48.6	4.7
450	6.4	5.7	87.9	0

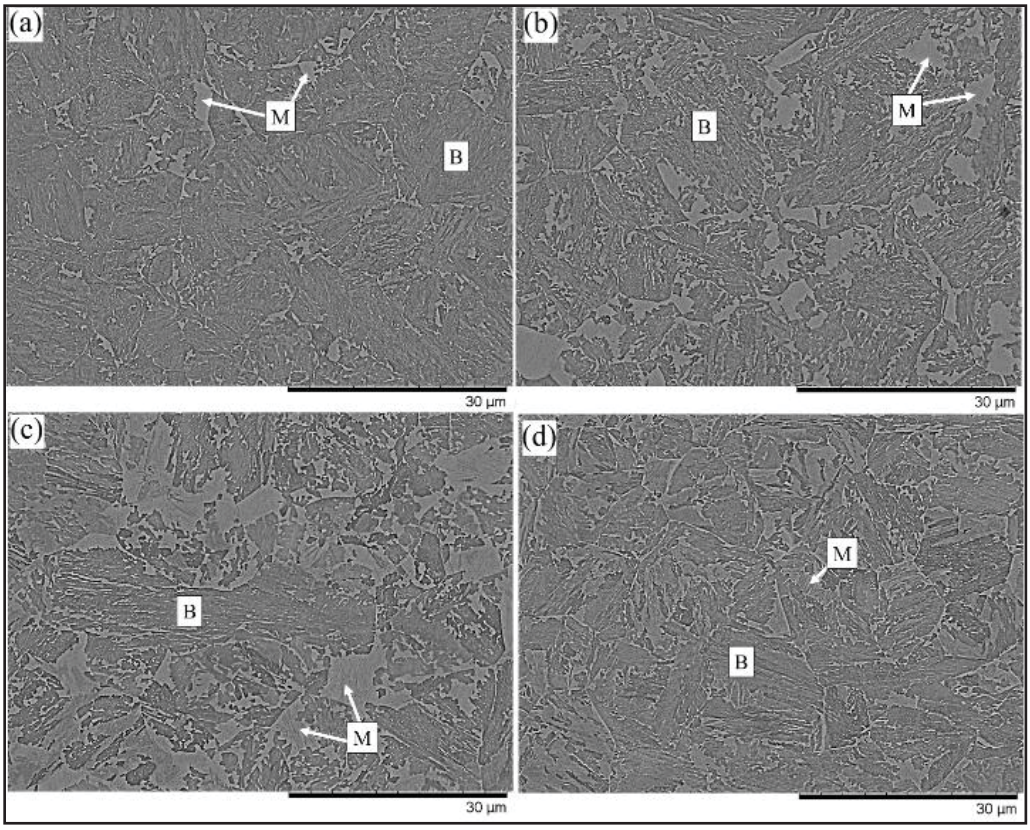

Figure 6-5 SEM images of the steel after isothermal holding at (a) 380 °C, (b) 400 °C, (c) 425 °C, and (d) 450 °C for 3 hours, showing bainite (B), and martensite (M)

6.4.3 Kinetics analysis

Dilatometry measurements during isothermal bainitic transformation at 380, 400, and 425 °C produced characteristic sigmoidal relative change in length (RCL) vs. time curves, as shown in Figure 6-6a, and Figure 6-6b shows the derivative of RCL as a function of time. These curves exhibit three distinct stages: (i) an initial incubation period prior to detectable transformation, (ii) a rapid growth stage marked (red arrow) by maximum dRCL/dt corresponding to the peak transformation rate (Figure 6-6b), and (iii) a final sluggish stage approaching a plateau where transformation stops due to carbon enrichment of the residual austenite.

Quantitative analysis reveals that decreasing the austempering temperature significantly accelerates transformation kinetics across all stages, with shorter incubation times, higher maximum transformation rates, and reduced times to reach the plateau. Notably, this acceleration of bainitic transformation kinetics with decreasing temperature is a typical, as a lower isothermal holding temperature causes a higher driving force, which enhances nucleation propensity, although carbon partitioning limitations ultimately yet decelerate overall kinetics. It could be speculated that microsegregation effects, arising from the relatively high Mn, Cr, and Mo contents of this P20 steel, promote the formation of small amounts of prior martensite at lower isothermal temperatures. Although such martensite might remain undetectable by dilatometry, its presence could autocatalytically stimulate the subsequent bainitic transformation. Additionally, the heterogeneous carbon distribution in the residual austenite evident from the dual dilatometric events during final cooling at 425 °C, may contribute to the accelerated kinetics at lower temperatures by creating local regions of enhanced driving force. The difference between the kinetics results obtained in this study and those reported in the literature (E. Wang et al., 2023), may be attributed to differences in chemical composition, particularly the silicon content. A detailed investigation of these mechanisms, however, lies beyond the scope of the present study.

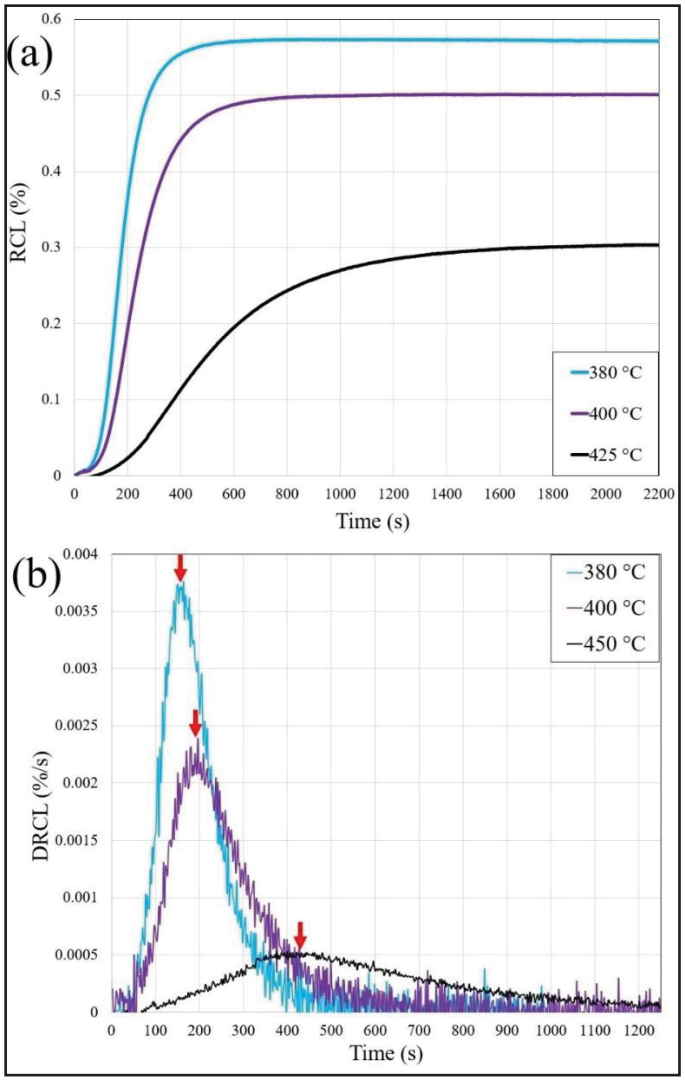

Figure 6-6 RCL as a function of time during isothermal bainitic phase transformation (a), and DRCL as a function of time (b)

6.4.4 Hardness measurement

Figure 6-7 shows Vickers hardness values after austempering at the different temperatures. Given the hardness hierarchy HV (martensite) > HV (bainite) ≫ HV (retained austenite), the phase fractions in Table 6-1 predict the observed trend.

Samples austempered at 380 °C (91.6 VB), 400 °C (80.2 VB), and 450 °C (87.9 VB) exhibit comparable hardness values of 411, 410, and 403 HV, respectively, despite microstructural differences.

The sharp hardness increases to 438 HV at 425 °C correlates directly with the elevated martensite fraction (48.6 vol.%) formed during final cooling, as confirmed by dilatometry (Figure 6-2) and SEM (Figure 6-5c). This enhanced martensite content more than compensates for the reduced bainite fraction, driving the hardness peak observed.

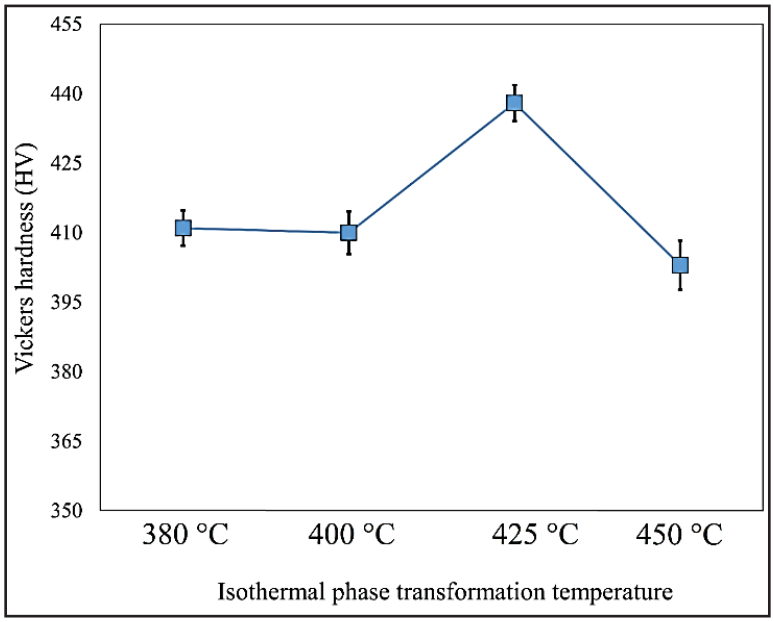

Figure 6-7 Microhardness of samples subjected to different isothermal temperatures

6.5 Conclusions

Slow continuous cooling (0.05 °C/s) to room temperature after 3-hour austempering at 380–450 °C was investigated via dilatometry, XRD, SEM, and hardness testing in a medium-carbon low-alloy steel, revealing key effects on microstructure, phase evolution, kinetics, and properties.

- Lower austempering temperatures produced higher bainite fractions (~92 vol.% at 380 °C), lower martensite during final cooling (4 vol.%), and comparable hardness (~410 HV); at 425 °C, martensite peaked (48.6 vol.%) with maximum hardness (438 HV).
- Martensite from higher-temperature incomplete reactions (425° C) yielded greater hardness than that from lower temperatures, outweighing bainite reduction.
- Retained austenite (<10 vol.%) was insensitive to austempering temperature or cooling rate (versus 10 °C/s (Tolouei, Saadati, et al., 2025)).
- Lower austempering temperatures accelerated bainitic transformation kinetics in all stages: incubation, peak rate, and end of transformation (plateau).

6.6 Chapter Summary and Outlook

This chapter demonstrates that at the industrially proposed isothermal holding temperature of 380 °C, slow cooling following isothermal bainitic transformation does not affect the retained austenite content, hardness, or microstructure of the material. This temperature had already been suggested to the industrial partner for use in the austempering of smaller blocks. In contrast, at higher temperatures, such as 425 °C, the transformation behavior differs significantly, with a multi-step phase transformation being observed.

CONCLUSIONS

This thesis systematically investigated bainitic phase transformation under both continuous cooling and isothermal conditions using processing parameters representative of industrial practice, combining experimental characterization with thermodynamic, kinetic, and mechanical analyses and following tempering. A key original contribution of this work shows that, in the investigated steels with very large prior austenite grain sizes, a multi-stage transformation sequence occurs under slow continuous cooling. In this sequence, granular and plate-like bainite form initially, followed by partial tempering of the bainitic structure and a subsequent martensitic transformation accompanied by auto-tempering. This multi-stage phase transformation in large-grained material can be attributed to the non-uniformity of the austenite.

The findings allowed to conclude that smaller prior austenite grain sizes accelerate transformation kinetics and increase the bainite fraction through enhanced grain boundary nucleation, whereas neither the cooling rate nor austenite grain sizes larger than 100 µm exert a significant influence on the martensite start temperature. Increasing the prior austenite grain size from 100 to 303 µm resulted in a substantial rise in the retained austenite volume fraction from 10% to 24.6%, highlighting the decisive role of austenite grain size in controlling the final microstructure and mechanical properties. This means that, for a large steel block, the tempering cycle time and temperature must be designed to fully decompose the 24.6% retained austenite at the center of the block.

The isothermal bainitic phase transformation in medium-carbon low-alloy steel was systematically investigated under industrially relevant conditions, with particular emphasis on microstructural stability, transformation kinetics, and the effects of subsequent cooling to room temperature. Within the examined austempering temperature range of 380–450 °C, the most homogeneous bainitic microstructure was obtained at 380 °C, making this condition the most suitable for industrial application. The results obtained at the other holding temperatures show a non-uniform distribution of bainite and martensite, leading to uneven hardness distribution, which is not acceptable from an industrial perspective.

Across all investigated conditions, the austempering temperature did not significantly influence the retained austenite volume fraction, which consistently remained below 10%, and variations in cooling rate after isothermal transformation likewise had no measurable effect on retained austenite content. In contrast, the austempering temperature exerted a pronounced effect on bainitic morphology and mechanical response: lower temperatures promoted refinement of bainitic ferrite. The results show that the austempering temperature plays a significant role in the transformation of residual austenite into martensite during final cooling, leading to a substantial increase in martensite content from 0% at 380 °C to 57% at 425 °C.

The tempering behavior of bainitic microstructures in medium-carbon low-alloy steel was systematically examined at different holding times to clarify the effects of thermal gradients and prolonged exposure under industrial-scale conditions. During the tempering of a large steel block, approximately 14 hours were required for the center to reach the target tempering temperature; as a result, the surface underwent substantial tempering before thermal equilibrium was achieved at the core, leading to distinctly different effective heat treatment histories between the surface and the center of the block. Tempering experiments conducted at 620 °C for varying holding times demonstrated that, within the investigated conditions, carbide coarsening did not occur even after 14 hours, emphasizing the inherent resistance of the bainitic microstructure to coarsening. Instead, microstructural softening during tempering was primarily associated with a reduction in the fraction of low-angle grain boundaries. Thermodynamic calculations performed using Thermo-Calc further indicated that $M_{23}C_6$ and M_7C_3 are the most stable carbide phases within the investigated temperature range, with Fe and Cr identified as the dominant constituent elements. In fresh martensitic regions, the tempering response was governed by the formation of aggregated carbide zones, a behavior attributed to the substantially higher carbon content of fresh martensite (~1.06%) compared with the nominal carbon content of the steel (0.26%).

RECOMMENDATIONS AND FUTURE WORK

1. It is recommended that the tempering behavior of bainitic microstructures in large prior austenite grains be investigated. Since both granular and plate-like bainite are formed in large austenite grains, the effect of the tempering process on hardness evolution should be assessed.
2. The effect of cooling rate prior to isothermal bainitic phase transformation should be investigated. In industrial practice, due to the large thickness of steel blocks, different rates at which the surface and the center reach the isothermal target temperature during immersion in the bath can influence the final microstructure and hardness.
3. It is recommended that the tempering process at different times and temperatures, followed by isothermal holding at 380 °C, be investigated, as it can provide valuable information for industrial applications.
4. To complete the thermodynamic calculation study of the carbide in medium-carbon low-alloy steels, it is recommended that the carbides and their morphologies be investigated using transmission electron microscopy (TEM).

These recommendations are based on the results of this research and offer a practical guideline for designing heat treatment cycles for large steel blocks, while improving microstructural uniformity in medium-carbon low-alloy steel applications.

LIST OF REFERENCES

Alsalamah, H. (2020). *The Effect of Prior Austenite Grain Size on Transformation Behaviour as a Function of Cooling Rate in Nuclear Pressure Vessel Steel SA508 G4N* University of Sheffield].

ANSYS Inc. (2020). *ANSYS Fluent Mosaic Technology Automatically Combines Disparate Meshes with Polyhedral Elements for Fast, Accurate Flow Resolution.* ANSYS Inc. Retrieved 8 July 2024 from https://www.ansys.com/content/dam/resource-center/white-paper/ansys-fluent-mosaic-technology-wp.pdf

ANSYS Inc. (2023 R2). *ANSYS Fluent Theory Guide*. In ANSYS, Inc. http://www.ansys.com

Babasafari, Z., Pan, A. V., Pahlevani, F., Hossain, R., Sahajwalla, V., du Toit, M., & Dippenaar, R. (2020). Effects of austenizing temperature, cooling rate and isothermal temperature on overall phase transformation characteristics in high carbon steel. *Journal of Materials Research and Technology*, *9*(6), 15286–15297. https://doi.org/https://doi.org/10.1016/j.jmrt.2020.10.071

Baek, M.-S., Kim, K.-S., Park, T.-W., Ham, J., & Lee, K.-A. (2020). Quantitative phase analysis of martensite-bainite steel using EBSD and its microstructure, tensile and high-cycle fatigue behaviors. *Materials Science and Engineering: A*, *785*, 139375. https://doi.org/https://doi.org/10.1016/j.msea.2020.139375

Bao, X., & Wang, J. a. (2021). Effects of lanthanum on bainite transformation behavior in Mn–Cr–Mo rail steel. *Journal of Materials Research*, *36*(6), 1400–1412. https://doi.org/10.1557/s43578-021-00220-7

Barbier, D. (2014). Extension of the Martensite Transformation Temperature Relation to Larger Alloying Elements and Contents. *Advanced Engineering Materials*, *16*(1), 122–127. https://doi.org/https://doi.org/10.1002/adem.201300116

Benrabah, I.-E., Deboer, A., Geandier, G., Van Landeghem, H., Hutchinson, C., Brechet, Y., & Zurob, H. (2024). Effect of deformation on the bainitic transformation. *Acta Materialia*, *277*, 120195. https://doi.org/https://doi.org/10.1016/j.actamat.2024.120195

Bhadeshia, H. (2001). *Bainite in steels: transformation, microstructure and properties*.

Bhadeshia, H. (2013). About calculating the characteristics of the martensite-austenite constituent. Proceeding of International Seminar on Welding of High Strength Pipeline Steels, CBMM and The Minerals.

Bhadeshia, H., & Honeycombe, R. In *Steels - Microstructure and Properties (4th Edition)*. Elsevier.

Bhadeshia, H., & Honeycombe, R. (2017). In *Steels - Microstructure and Properties (4th Edition)*. Elsevier.

Bhadeshia, H., & Waugh, A. (1982). Bainite: An atom-probe study of the incomplete reaction phenomenon. *Acta Metallurgica*, *30*(4), 775–784.

Bhadeshia, H. K. D. H. (2001). *Bainite in Steels: Transformations, Microstructure and Properties* (Second ed.). IOM Communications.

Bhadeshia, H. K. D. H. (2019). *Bainite in Steels: Theory and Practice, Third Edition*. CRC Press.

Bhadeshia, H. K. D. H., & Christian, J. W. (1990). Bainite in steels. *Metallurgical Transactions A*, *21*(3), 767–797. https://doi.org/10.1007/BF02656561

Bhadeshia, H. K. D. H., & Edmonds, D. V. (1979). The bainite transformation in a silicon steel. *Metall Trans A 10*, 895–907.

Bhadeshia, H. K. D. H., & Edmonds, D. V. (1980). The mechanism of bainite formation in steels. *Acta Metallurgica*, *28*(9), 1265–1273. https://doi.org/https://doi.org/10.1016/0001-6160(80)90082-6

Bhuyan, D., Sastry, G. V. S., Patra, S., Pradhan, S. K., & Manna, R. (2023). Effect of austempering time on bainite plate thickness and variant selection in a high carbon low alloy steel. *Materials Characterization*, *200*, 112923. https://doi.org/https://doi.org/10.1016/j.matchar.2023.112923

Bouissa, Y., Zorgani, M., Shahriari, D., Champliaud, H., Morin, J.-B., & Jahazi, M. (2021). Microstructure-Based FEM Modeling of Phase Transformation During Quenching of Large-Size Steel Forgings. *Metallurgical and Materials Transactions A*, *52*(5), 1883–1900. https://doi.org/10.1007/s11661-021-06199-4

Bragg William Henry, & Lawrence, B. W. (1913). The reflection of X-rays by crystals. *Proc. R. Soc. Lond. A*, *88*, 428–438.

Bramfitt, B. L., & Speer, J. G. (1990). A perspective on the morphology of bainite. *Metallurgical Transactions A*, *21*(3), 817–829. https://doi.org/10.1007/BF02656565

Branco, R., Berto, F., Zhang, F., Long, X., & Costa, J. D. (2018). Comparative Study of the Uniaxial Cyclic Behaviour of Carbide-Bearing and Carbide-Free Bainitic Steels. *Metals*, *8*(6), 422.

Bush, M. E., & Kelly, P. M. (1971). Strengthening mechanisms in bainitic steels. *Acta Metallurgica*, *19*(12), 1363–1371. https://doi.org/https://doi.org/10.1016/0001-6160(71)90074-5

Caballero, F. G., Garc, iacute, a-Mateo, C., Garc, iacute, a de, A., eacute, & s, C. (2005). Dilatometric Study of Reaustenitisation of High Silicon Bainitic Steels: Decomposition of Retained Austenite. *MATERIALS TRANSACTIONS*, *46*(3), 581–586. https://doi.org/10.2320/matertrans.46.581

Caballero, F. G., Roelofs, H., Hasler, S., Capdevila, C., Chao, J., Cornide, J., & Garcia-Mateo, C. (2012). Influence of bainite morphology on impact toughness of continuously cooled cementite free bainitic steels. *Materials Science and Technology*, *28*(1), 95–102. https://doi.org/10.1179/1743284710y.0000000047

Celada-Casero, C., Sietsma, J., & Santofimia, M. J. (2019). The role of the austenite grain size in the martensitic transformation in low carbon steels. *Materials & Design*, *167*, 107625. https://doi.org/https://doi.org/10.1016/j.matdes.2019.107625

Chen, Z., Zhao, X., Qi, J., Zhu, W., Zhao, Y., & Chen, L. (2022). Effect of Austenite Grain Size on the Bainitic Transformation in a 690 MPa Grade High-Strength Multi-Functional Construction Steel. *Metals*, *12*(4), 577.

Cheng, L., Böttger, A., de Keijser, T. H., & Mittemeijer, E. J. (1990). Lattice parameters of iron-carbon and iron-nitrogen martensites and austenites. *Scripta Metallurgica et Materialia*, *24*(3), 509–514. https://doi.org/https://doi.org/10.1016/0956-716X(90)90192-J

Christien, F., Telling, M. T. F., & Knight, K. S. (2013). A comparison of dilatometry and in-situ neutron diffraction in tracking bulk phase transformations in a martensitic stainless steel. *Materials Characterization*, *82*, 50–57. https://doi.org/https://doi.org/10.1016/j.matchar.2013.05.002

Committee, A. (2013). Standard Practice for X-Ray Determination of Retained Austenite in Steel with Near Random Crystallographic Orientation. In (pp. 7). ASTM International, 100 Barr Harbor Drive, PO Box C700, West Conshohocken, PA 19428-2959. United States.

Cornide, J., Garcia-Mateo, C., Capdevila, C., & Caballero, F. G. (2013). An assessment of the contributing factors to the nanoscale structural refinement of advanced bainitic steels. *Journal of Alloys and Compounds*, *577*, S43–S47. https://doi.org/https://doi.org/10.1016/j.jallcom.2011.11.066

Cornide, J., Miyamoto, G., Caballero, F. G., Furuhara, T., Miller, M. K., & Garcia-Mateo, C. (2011). Distribution of Dislocations in Nanostructured Bainite. *Solid State Phenomena*, *172-174*, 117–122. https://doi.org/10.4028/www.scientific.net/SSP.172-174.117

Davis, J. R. (1998). *Metals Handbook Desk Edition*. ASM International. https://doi.org/10.31399/asm.hb.mhde2.9781627081993

De-Castro, D., Eres-Castellanos, A., Vivas, J., Caballero, F. G., San-Martín, D., & Capdevila, C. (2022). Morphological and crystallographic features of granular and lath-like bainite in a low carbon microalloyed steel. *Materials Characterization*, *184*, 111703. https://doi.org/https://doi.org/10.1016/j.matchar.2021.111703

Dépinoy, S., Toffolon-Masclet, C., Urvoy, S., Roubaud, J., Marini, B., Roch, F., Kozeschnik, E., & Gourgues-Lorenzon, A.-F. (2017). Carbide Precipitation in 2.25 Cr-1 Mo Bainitic Steel: Effect of Heating and Isothermal Tempering Conditions. *Metallurgical and Materials Transactions A*, *48*(5), 2164–2178. https://doi.org/10.1007/s11661-017-4045-6

Dhondapure, P., Rajakrishnan, N., Nayak, S., Champliaud, H., Morin, J.-B., & Jahazi, M. (2024). Influence of deformation path on microstructure evolution during the open die forging of large size ingot of high strength steel: experiments and FE analysis. *The International Journal of Advanced Manufacturing Technology*, *134*(7), 3733–3750. https://doi.org/10.1007/s00170-024-14360-7

Dhondapure, P., Tize Mha, P., Nayak, S., Ebacher, L., Dourandish, S., Champliaud, H., Morin, J.-B., & Jahazi, M. (2023). Influence of deformation path on the stress state and damage evolution along the central axis of a large size forged ingot of AISI H13 steel. *Journal of Materials Research and Technology*, *27*, 8244–8257. https://doi.org/https://doi.org/10.1016/j.jmrt.2023.11.206

Dixit, S., Chaudhari, V., & Kulkarni, D. M. (2020). Effect of tempering time on mechanical and fracture behavior of SA 387 Gr.11 pressure vessel steel. *Journal of Materials Processing Technology*, *276*, 116419. https://doi.org/https://doi.org/10.1016/j.jmatprotec.2019.116419

Elena Pereloma, & V.Edmonds, D. (2012). *Phase transformations in steels* (Vol. 2). Woodhead Publishing Limited.

Eres-Castellanos, A., Toda-Caraballo, I., Latz, A., Caballero, F. G., & Garcia-Mateo, C. (2020). An integrated-model for austenite yield strength considering the influence of temperature and strain rate in lean steels. *Materials & Design*, *188*, 108435. https://doi.org/https://doi.org/10.1016/j.matdes.2019.108435

Firrao, D., Matteis, P., Scavino, G., Graziano, U., Ienco, M., Parodi, A., Pinasco, M., Stagno, E., Gerosa, R., Rivolta, B., Silva, G., Silvestri, A., & Ghidini, A. (2006). Heat treatment

and failure risk of large automotive plastic molds: a fracture mechanics approach and property assessment. *Metallurgia Italiana*, *98*, 43–51.

Fisher, J. C. H., J.H.; Turnbull, D. (1949). Kinetics of the Austenite to Martensite Transformation. *Journal of Metals, Transactions AIME*, *185*, 691–700.

Franceschi, M., Bertolini, R., Fabrizi, A., Dabalà, M., & Pezzato, L. (2023). Effect of ausforming temperature on bainite morphology in a 3.2% Si carbide-free bainitic steel. *Materials Science and Engineering: A*, *864*, 144553. https://doi.org/https://doi.org/10.1016/j.msea.2022.144553

Franceschi, M., Morales-Rivas, L., Cordova-Tapia, E., Jimenez, J. A., Dabalà, M., & Garcia-Mateo, C. (2024). Study of bainite and martensite tempering in a medium C high Si steel. microstructural disparities and equilibrium convergence. *Journal of Materials Research and Technology*, *32*, 2931–2944. https://doi.org/https://doi.org/10.1016/j.jmrt.2024.08.141

Franceschi, M., Pezzato, L., Settimi, A. G., Gennari, C., Pigato, M., Polyakova, M., Konstantinov, D., Brunelli, K., & Dabalà, M. (2021). Effect of Different Austempering Heat Treatments on Corrosion Properties of High Silicon Steel. *Materials*, *14*(2), 288.

Gao, B., Tan, Z., Tian, Y., Liu, Y., Wang, R., Gao, G., Wang, J., & Zhang, M. (2022). Accelerated Isothermal Phase Transformation and Enhanced Mechanical Properties of Railway Wheel Steel: The Significant Role of Pre-Existing Bainite. *steel research international*, *93*(2), 2100494. https://doi.org/https://doi.org/10.1002/srin.202100494

Garcia-Mateo, Jimenez, Yen, H. W., Miller, M. K., Morales-Rivas, L., Kuntz, M., Ringer, S. P., Yang, J. R., & Caballero, F. G. (2015). Low temperature bainitic ferrite: Evidence of carbon super-saturation and tetragonality. *Acta Materialia*, *91*, 162–173. https://doi.org/https://doi.org/10.1016/j.actamat.2015.03.018

Garcia-Mateo, C., & Caballero, F. G. (2005). Ultra-high-strength Bainitic Steels. *ISIJ International*, *45*(11), 1736–1740. https://doi.org/10.2355/isijinternational.45.1736

Garcia-Mateo, C., Caballero, F. G., & Bhadeshia, H. K. D. H. (2003). Development of Hard Bainite. *ISIJ International*, *43*(8), 1238–1243. https://doi.org/10.2355/isijinternational.43.1238

Garcia-Mateo, C., Caballero, F. G., Miller, M. K., & Jimenez, J. A. (2012). On measurement of carbon content in retained austenite in a nanostructured bainitic steel. *Journal of Materials Science*, *47*(2), 1004–1010. https://doi.org/10.1007/s10853-011-5880-2

Garcia-Mateo, C., Paul, G., Somani, M. C., Porter, D. A., Bracke, L., Latz, A., Garcia De Andres, C., & Caballero, F. G. (2017). Transferring Nanoscale Bainite Concept to Lower C Contents: A Perspective. *Metals*, *7*(5).

Garcia-Mateo, C., Peet, M., Caballero, F. G., & Bhadeshia, H. K. D. H. (2004). Tempering of hard mixture of bainitic ferrite and austenite. *Materials Science and Technology*, *20*(7), 814–818. https://doi.org/10.1179/026708304225017355

Gorunov, A. I. (2020). Investigation of M7C3, M23C6 and M3C carbides synthesized on austenitic stainless steel and carbon fibers using laser metal deposition. *Surface and Coatings Technology*, *401*, 126294. https://doi.org/https://doi.org/10.1016/j.surfcoat.2020.126294

Grajcar, A., & Krztoń, H. (2011). Effect of isothermal holding temperature on retained austenite fraction in medium-carbon Nb/Ti-microalloyed TRIP steel. *Journal of Achievements in Materials and Manufacturing Engineering*, *49*, 391–399.

Grajcar, A., Skrzypczyk, P., & Kozłowska, A. (2018). Effects of Temperature and Time of Isothermal Holding on Retained Austenite Stability in Medium-Mn Steels. *Applied Sciences*, *8*(11), 2156.

Gulbay, O., Ackermann, M., Gramlich, A., Durmaz, A. R., Steinbach, I., & Krupp, U. (2023). Influence of Transformation Temperature on the High-Cycle Fatigue Performance of Carbide-Bearing and Carbide-Free Bainite. *steel research international*, *94*(12), 2300238. https://doi.org/https://doi.org/10.1002/srin.202300238

Han, Y., Wu, H., Liu, C., & Liu, Y. (2014). Microstructures and Mechanical Characteristics of a Medium Carbon Super-Bainitic Steel After Isothermal Transformation. *Journal of Materials Engineering and Performance*, *23*(12), 4230–4236. https://doi.org/10.1007/s11665-014-1235-x

Han, Y., Xiu, W., Liu, C., & Wu, H. (2017). Isothermal Transformation of a Commercial Super-Bainitic Steel: Part I Microstructural Characterization and Hardness. *Journal of Materials Engineering and Performance*, *26*(2), 472–477. https://doi.org/10.1007/s11665-016-2473-x

Hanamura, T., Torizuka, S., Tamura, S., Enokida, S., & Takechi, H. (2013). Effect of Austenite Grain Size on Transformation Behavior, Microstructure and Mechanical Properties of 0.1C–5Mn Martensitic Steel. *ISIJ International*, *53*(12), 2218–2225. https://doi.org/10.2355/isijinternational.53.2218

Hasan, S. M., Kumar, S., Chakrabarti, D., & Singh, S. B. (2020). Effect of prior austenite grain size on the formation of carbide-free bainite in low-alloy steel. *Philosophical Magazine*, *100*(18), 2320–2334. https://doi.org/10.1080/14786435.2020.1764653

He, S. H., He, B. B., Zhu, K. Y., & Huang, M. X. (2018). Evolution of dislocation density in bainitic steel: Modeling and experiments. *Acta Materialia*, *149*, 46–56. https://doi.org/https://doi.org/10.1016/j.actamat.2018.02.023

Hirth, J. P. (1972). The influence of grain boundaries on mechanical properties. *Metallurgical Transactions*, *3*(12), 3047–3067. https://doi.org/10.1007/BF02661312

Hu, F., Hodgson, P. D., & Wu, K. M. (2014). Acceleration of the super bainite transformation through a coarse austenite grain size. *Materials Letters*, *122*, 240–243. https://doi.org/https://doi.org/10.1016/j.matlet.2014.02.051

Huang, Y., Zhao, A.-m., He, J.-g., Wang, X.-p., Wang, Z.-g., & Qi, L. (2013). Microstructure, crystallography and nucleation mechanism of NANOBAIN steel. *International Journal of Minerals, Metallurgy, and Materials*, *20*(12), 1155–1163. https://doi.org/10.1007/s12613-013-0849-6

Humphreys, F. J., & Hatherly, M. (2004). Chapter 4 - The Structure and Energy of Grain Boundaries. In F. J. Humphreys & M. Hatherly (Eds.), *Recrystallization and Related Annealing Phenomena (Second Edition)* (pp. 91–119). Elsevier. https://doi.org/https://doi.org/10.1016/B978-008044164-1/50008-6

Hurel, V. (2022). *Optimazation of the heat treatment of a steel with high mechanical resistance* Ecole de technology superior].

I, T. (1970). Steel Material Study on the Strength. *Nikkan Kogyo Shinbun Ltd, Tokyo*, *40*.

Isasti, N., Jorge-Badiola, D., Alkorta, J., & Uranga, P. (2016). Analysis of Complex Steel Microstructures by High-Resolution EBSD. *JOM*, *68*(1), 215–223. https://doi.org/10.1007/s11837-015-1677-0

Javed, M. A., Ivanovich, N., Messinese, E., Liu, R., Astorga, S. E., Yeo, Y. P., Idapalapati, S., Lauro, F. M., & Wade, S. A. (2024). The Role of Metallurgical Features in the Microbially Influenced Corrosion of Carbon Steel: A Critical Review. *Microorganisms*, *12*(5), 892.

Jentner, R. M., Tsai, S. P., Welle, A., Scholl, S., Srivastava, K., Best, J. P., Kirchlechner, C., & Dehm, G. (2023). Automated classification of granular bainite and polygonal ferrite by electron backscatter diffraction verified through local structural and mechanical analyses. *Journal of Materials Research*, *38*(18), 4177–4191. https://doi.org/10.1557/s43578-023-01113-7

Jeong, B.-Y., Gauvin, R., & Yue, S. (2002). EBSD Study of Martensite in a Dual Phase Steel. *Microscopy and Microanalysis*, *8*(S02), 700–701. https://doi.org/10.1017/S1431927602106507

Jiang, Z., Li, Y., Yang, Z., Wang, P., Li, D., & Li, Y. (2021). The tempering behavior of martensite/austenite islands on the mechanical properties of a low alloy Mn-Ni-Mo steel with granular bainite. *Materials Today Communications*, *26*, 102166. https://doi.org/https://doi.org/10.1016/j.mtcomm.2021.102166

JMatPro. Retrieved 13.3 from www.https://www.sentesoftware.co.uk/biblio.html

Kim, S. H., Kim, K.-H., Bae, C.-M., Lee, J. S., & Suh, D.-W. (2018). Microstructure and Mechanical Properties of Austempered Medium-Carbon Spring Steel. *Metals and Materials International*, *24*(4), 693–701. https://doi.org/10.1007/s12540-018-0085-8

Knijf, D., Petrov, R., Föjer, C., & Kestens, L. (2014). Effect of fresh martensite on the stability of retained austenite in quenching and partitioning steel. *Materials Science and Engineering: A*, *615*, 107–115. https://doi.org/10.1016/j.msea.2014.07.054

Kozeschnik, E., & Bhadeshia, H. K. D. H. (2008). Influence of silicon on cementite precipitation in steels. *Materials Science and Technology*, *24*(3), 343–347. https://doi.org/10.1179/174328408X275973

Krauss, G. (1999). Martensite in steel: strength and structure. *Materials Science and Engineering: A*, *273-275*, 40–57. https://doi.org/https://doi.org/10.1016/S0921-5093(99)00288-9

Królicka, A., Lesiuk, G., Kuziak, R., Radwański, K., & Janik, A. (2023). The Role of Microstructure Morphology on Fracture Mechanisms of Continuously Cooled Bainitic Steel Designed for Rails Application. *Metallurgical and Materials Transactions A*, *54*(2), 487–504. https://doi.org/10.1007/s11661-022-06886-w

Kwak, K., Mine, Y., Morito, S., Ohmura, T., & Takashima, K. (2022). Correlation between strength and hardness for substructures of lath martensite in low- and medium-carbon steels. *Materials Science and Engineering: A*, *856*, 144007. https://doi.org/https://doi.org/10.1016/j.msea.2022.144007

Lambert-Perlade, A., Gourgues, A. F., Besson, J., Sturel, T., & Pineau, A. (2004). Mechanisms and modeling of cleavage fracture in simulated heat-affected zone microstructures of a high-strength low alloy steel. *Metallurgical and Materials Transactions A*, *35*(13), 1039–1053. https://doi.org/10.1007/s11661-004-1007-6

Lan, H. F., Du, L. X., Li, Q., Qiu, C. L., Li, J. P., & Misra, R. D. K. (2017). Improvement of strength-toughness combination in austempered low carbon bainitic steel: The key role of refining prior austenite grain size. *Journal of Alloys and Compounds*, *710*, 702–710. https://doi.org/https://doi.org/10.1016/j.jallcom.2017.03.024

Lan, L., Chang, Z., & Fan, P. (2018). Exploring the Difference in Bainite Transformation with Varying the Prior Austenite Grain Size in Low Carbon Steel. *Metals*, *8*(12).

Lan, L. Y., Qiu, C. L., Zhao, D. W., Gao, X. H., & Du, L. X. (2011). Effect of austenite grain size on isothermal bainite transformation in low carbon microalloyed steel. *Materials Science and Technology*, *27*(11), 1657–1663. https://doi.org/10.1179/1743284710y.0000000026

Lee, S.-J., Park, J.-S., & Lee, Y.-K. (2008). Effect of austenite grain size on the transformation kinetics of upper and lower bainite in a low-alloy steel. *Scripta Materialia*, *59*(1), 87–90. https://doi.org/https://doi.org/10.1016/j.scriptamat.2008.02.036

Lee, Y. K., Shin, H. C., Jang, Y. C., Kim, S. H., & Choi, C. S. (2002). Effect of isothermal transformation temperature on amount of retained austenite and its thermal stability in a bainitic Fe–3%Si–0.45%C–X steel. *Scripta Materialia*, *47*(12), 805–809. https://doi.org/https://doi.org/10.1016/S1359-6462(02)00303-2

Lei, M., Dang, F.-N., Xue, H., Xing, J., & Ding, W. (2022). Study on the Effect of Nanoindentation Test Method on Micromechanical Properties of Granite Minerals. *Geofluids*, *2022*.

Lerchbacher, C., Zinner, S., & Leitner, H. (2013). Direct or indirect: Influence of type of retained austenite decomposition during tempering on the toughness of a hot-work tool steel. *Materials Science and Engineering: A*, *564*, 163–168. https://doi.org/https://doi.org/10.1016/j.msea.2012.11.105

Li, C. W., Han, L. Z., Luo, X. M., Liu, Q. D., & Gu, J. F. (2016). Effect of tempering temperature on the microstructure and mechanical properties of a reactor pressure vessel steel. *Journal of Nuclear Materials*, *477*, 246–256. https://doi.org/https://doi.org/10.1016/j.jnucmat.2016.05.017

Li, Y., Zhang, F., Chen, C., Lv, B., Yang, Z., & Zheng, C. (2016). Effects of deformation on the microstructures and mechanical properties of carbide–free bainitic steel for railway crossing and its hydrogen embrittlement characteristics. *Materials Science and Engineering: A*, *651*, 945–950. https://doi.org/https://doi.org/10.1016/j.msea.2015.09.117

Li, Z., & Davis, C. (2019). Ironmaking and Steelmaking. *Metals*, *9*(5), 525.

Lin, S., Borgenstam, A., Stark, A., & Hedström, P. (2022). Effect of Si on bainitic transformation kinetics in steels explained by carbon partitioning, carbide formation, dislocation densities, and thermodynamic conditions. *Materials Characterization*, *185*, 111774. https://doi.org/https://doi.org/10.1016/j.matchar.2022.111774

Liu, C., Shi, L., Liu, Y., Li, C., Li, H., & Guo, Q. (2016). Acicular ferrite formation during isothermal holding in HSLA steel. *Journal of Materials Science*, *51*, 3555–3563.

Liu, C., Zhao, Z., Northwood, D. O., & Liu, Y. (2001). A new empirical formula for the calculation of MS temperatures in pure iron and super-low carbon alloy steels. *Journal of Materials Processing Technology*, *113*(1), 556–562. https://doi.org/https://doi.org/10.1016/S0924-0136(01)00625-2

Liu, H., Fu, P., Liu, H., Sun, C., Ma, X., & Li, D. (2018). Microstructure evolution and mechanical properties in 718H pre-hardened mold steel during tempering. *Materials Science and Engineering: A*, *709*, 181–192. https://doi.org/https://doi.org/10.1016/j.msea.2017.10.047

Liu J. H., Binot N., Delagnes D., & Jahazi M. (2021). Influence of the cooling rate below Ms on the martensitic transformation in a low alloy medium-carbon steel. *Journal of Materials Research and Technology*, *12*, 234–242. https://doi.org/https://doi.org/10.1016/j.jmrt.2021.02.075

Liu, M., Xu, G., Tian, J.-y., Yuan, Q., & Chen, X. (2020). Effect of austempering time on microstructure and properties of a low-carbon bainite steel. *International Journal of Minerals, Metallurgy and Materials*, *27*(3), 340–346. https://doi.org/10.1007/s12613-019-1881-y

Liu, M., Xu, G., Tian, J., Yuan, Q., Zhou, M., & Hu, H. (2019). The Effect of Stress on Bainite Transformation, Microstructure, and Properties of a Low-Carbon Bainitic Steel. *steel research international*, *90*(10), 1900159. https://doi.org/https://doi.org/10.1002/srin.201900159

Liu, T., Long, M., Fan, H., Chen, D., Chen, H., Duan, H., Jiang, W., & He, W. (2018). Dilatometric determination of four critical temperatures and phase transition fraction for austenite decomposition in hypo-eutectoid steels using peak separation method. *Journal of Materials Research*, *33*(8), 967–977. https://doi.org/10.1557/jmr.2017.484

Long, X., Yang, R., Sun, D., Liu, W., Zhang, Y., Zhang, F., Yang, Z., & Li, Y. (2023). Roles of cooling rate of undercooled austenite on isothermal transformation kinetics, microstructure, and impact toughness of bainitic steel. *Materials Science and Engineering: A*, *870*, 144821. https://doi.org/https://doi.org/10.1016/j.msea.2023.144821

Long, X., Zhang, F., Yang, Z., & Lv, B. (2018). Study on microstructures and properties of carbide-free and carbide-bearing bainitic steels. *Materials Science and Engineering: A*, *715*, 10–16. https://doi.org/https://doi.org/10.1016/j.msea.2017.12.108

Long, X. Y., Branco, R., Macek, W., Masoudi Nejad, R., Lesiuk, G., Zhu, S. P., & Amaro, A. M. (2023). Effect of austempering temperature on microstructure and cyclic deformation behaviour of multiphase low-carbon steel. *Archives of Civil and Mechanical Engineering*, *23*(3), 201. https://doi.org/10.1007/s43452-023-00735-2

Long, X. Y., C., Z. F., J., K., N., Y. Z., D., W. D., M., W. K., & and Zhang, G. H. (2017). Study on carbide-bearing and carbide-free bainitic steels and their wear resistance. *Materials Science and Technology*, *33*(5), 615–622. https://doi.org/10.1080/02670836.2016.1242205

Long, X. Y., Sun, D. Y., Wang, K., Zhang, F. C., Yang, Z. N., Li, Y. G., & Zheng, C. L. (2022). Effect of carbon distribution range in mixed bainite / martensite / retained austenite microstructure on mechanical properties. *Journal of Materials Research and Technology*, *17*, 898–912. https://doi.org/https://doi.org/10.1016/j.jmrt.2021.12.121

Luo, Q., Mei, H., Kitchen, M., Gao, Y., & Bowen, L. (2021). Effect of Short-Term Low-Temperature Austempering on the Microstructure and Abrasive Wear of Medium-Carbon Low-Alloy Steel. *Metals and Materials International*, *27*(9), 3115–3131. https://doi.org/10.1007/s12540-020-00957-6

M.J. Bibby, & Parr, J. G. (1964). The Martensitic Transformation in Pure Iron. *Journal of the Iron and Steel Institute (JISI)*, *202*, 100.

Mandal, S., Bhowmik, N., Tewary, N. K., Ghosh, P., & Haldar, A. (2022). Austenite grain growth and effect of austenite grain size on bainitic transformation. *Materials Science and Technology*, *38*(7), 409–418. https://doi.org/10.1080/02670836.2022.2045547

Matsuzaki, A., & Bhadeshia, H. K. D. H. (1999). Effect of austenite grain size and bainite morphology on overall kinetics of bainite transformation in steels. *Materials Science and Technology*, *15*(5), 518–522. https://doi.org/10.1179/026708399101506210

Mazaheri, Y., Kermanpur, A., & Najafizadeh, A. (2015). Nanoindentation study of ferrite–martensite dual phase steels developed by a new thermomechanical processing. *Materials Science and Engineering: A*, *639*, 8–14. https://doi.org/https://doi.org/10.1016/j.msea.2015.04.098

Mazancová, E., & Mazanec, K. (1997). Physical metallurgy characteristics of the M/A constituent formation in granular bainite. *Journal of Materials Processing Technology*, *64*(1), 287–292. https://doi.org/https://doi.org/10.1016/S0924-0136(96)02578-2

Mirzaei, S., Arkhazloo, N. B., Morin, J.-B., & Jahazi, M. (2024). Influence of Heating Elements Layout on Temperature Uniformity in a Large Size Heat Treatment Furnace. *Case Studies in Thermal Engineering*, 105062.

Mirzaei, S., Bohlooli Arkhazloo, N., Bazdidi-Tehrani, F., Morin, J.-B., Loucif, A., & Jahazi, M. (2023). Influence of Spacers and Skid Sizes on Heat Treatment of Large Forgings within an Industrial Electric Furnace. *Energies*, *16*(7), 2936.

Mirzaei Sajad, Bohlooli Arkhazloo Nima, Morin Jean-Benoit, & Jahazi Mohammad. (2024). Influence of heating elements layout on temperature uniformity in a large size heat treatment furnace. *Case Studies in Thermal Engineering*, *61*, 105062. https://doi.org/https://doi.org/10.1016/j.csite.2024.105062

Mitchell, D. R. G., & Ball, C. J. (2001). A quantitative X-ray diffraction and analytical electron microscopy study of service-exposed 2.25Cr–1Mo steels. *Materials Characterization*, *47*(1), 17–26. https://doi.org/https://doi.org/10.1016/S1044-5803(01)00147-4

Mohammadijoo, M., Valloton, J., Collins, L., Henein, H., & Ivey, D. G. (2018). Characterization of martensite-austenite constituents and micro-hardness in intercritical reheated and coarse-grained heat affected zones of API X70 HSLA steel. *Materials Characterization*, *142*, 321–331. https://doi.org/https://doi.org/10.1016/j.matchar.2018.05.057

Mondal, J., Das, K., & Das, S. (2021). Isothermal transformation kinetics, microstructure and mechanical properties of a carbide free bainitic steel. *Materials Characterization*, *177*, 111166. https://doi.org/https://doi.org/10.1016/j.matchar.2021.111166

Moravec, J., Dikovits, M., Novakova, I., & Caliskanoglu, O. (2016). Comparison of Dilatometry Results Obtained by Two Different Devices when Generating CCT and In Situ Diagrams. *Key Engineering Materials*, *669*, 477–484. https://doi.org/10.4028/www.scientific.net/KEM.669.477

Morawiec, M., Ruiz-Jimenez, V., Garcia-Mateo, C., & Grajcar, A. (2020). Thermodynamic analysis and isothermal bainitic transformation kinetics in lean medium-Mn steels. *Journal of Thermal Analysis and Calorimetry*, *142*(5), 1709–1719. https://doi.org/10.1007/s10973-020-10259-z

Morawiec, M., Ruiz-Jimenez, V., Garcia-Mateo, C., Jimenez, J. A., & Grajcar, A. (2022). Study of the isothermal bainitic transformation and austenite stability in an advanced Al-rich medium-Mn steel. *Archives of Civil and Mechanical Engineering*, *22*(4), 152. https://doi.org/10.1007/s43452-022-00475-9

Morawiec, M., Skowronek, A., Król, M., & Grajcar, A. (2020). Dilatometric Analysis of the Austenite Decomposition in Undeformed and Deformed Low-Carbon Structural Steel. *Materials*, *13*(23), 5443.

Navarro-López, A., Hidalgo, J., Sietsma, J., & Santofimia, M. J. (2017). Characterization of bainitic/martensitic structures formed in isothermal treatments below the Ms temperature. *Materials Characterization*, *128*, 248–256. https://doi.org/https://doi.org/10.1016/j.matchar.2017.04.007

Ni, P., Shi, W., Lu, H., Zhang, B., & Dong, H. (2025). Effect of tempering temperature on low-temperature impact toughness of 35MnB steel. *Journal of Materials Research and Technology*, *34*, 2463–2476. https://doi.org/https://doi.org/10.1016/j.jmrt.2024.12.246

Oliver, W. C., & Pharr, G. M. (1992). An improved technique for determining hardness and elastic modulus using load and displacement sensing indentation experiments. *Journal of Materials Research*, *7*(6), 1564–1583. https://doi.org/10.1557/JMR.1992.1564

Park, J.-Y., Ko, W.-S., Park, K. B., Kang, G. B., Im, H.-T., Kwon, H. G., Hwang, N.-M., & Park, H.-K. (2022). Effect of Cooling Rate on Phase Transformation Behavior during Isothermal Annealing of SCr420 Steel. *steel research international*, *93*(5), 2100711. https://doi.org/https://doi.org/10.1002/srin.202100711

Pashangeh, S., Karimi Zarchi, H. R., Ghasemi Banadkouki, S. S., & Somani, M. C. (2019). Detection and Estimation of Retained Austenite in a High Strength Si-Bearing Bainite-Martensite-Retained Austenite Micro-Composite Steel after Quenching and Bainitic Holding (Q&B). *Metals*, *9*(5), 492.

Pashangeh, S., Somani, M. C., Ghasemi Banadkouki, S. S., Karimi Zarchi, H. R., Kaikkonen, P., & Porter, D. A. (2020). On the decomposition of austenite in a high-silicon medium-carbon steel during quenching and isothermal holding above and below the Ms temperature. *Materials Characterization*, *162*, 110224. https://doi.org/https://doi.org/10.1016/j.matchar.2020.110224

Pereloma, E., & Edmonds, D. V. (2012). *Diffusionless transformations, high strength steels, modelling and advanced analytical techniques*. Woodhead Pub.

Podder, A. S. (2011). *Tempering of a mixture of bainite and retained austenite* University of Cambridge].

Porter, D. A., & Easterling, K. E. (2009). *Phase Transformations in Metals and Alloys (Revised Reprint)*. CRC Press.

Putatunda, S. K., Martis, C., & Boileau, J. (2011). Influence of austempering temperature on the mechanical properties of a low carbon low alloy steel. *Materials Science and Engineering: A*, *528*(15), 5053–5059. https://doi.org/https://doi.org/10.1016/j.msea.2011.03.038

Qiao, Z. X., Liu, Y. C., Yu, L. M., & Gao, Z. M. (2009). Formation mechanism of granular bainite in a 30CrNi3MoV steel. *Journal of Alloys and Compounds*, *475*(1), 560–564. https://doi.org/https://doi.org/10.1016/j.jallcom.2008.07.110

Rampelberg, C., Allain, S. Y. P., Geandier, G., Teixeira, J., Lebel, F., & Sourmail, T. (2021). Carbide-Free Bainite Transformations Above and Below Martensite Start Temperature Investigated by In-Situ High-Energy X-Ray Diffraction. *JOM*, *73*(11), 3181–3194. https://doi.org/10.1007/s11837-021-04903-8

Ravi, A. M., Sietsma, J., & Santofimia, M. J. (2016). Exploring bainite formation kinetics distinguishing grain-boundary and autocatalytic nucleation in high and low-Si steels. *Acta Materialia*, *105*, 155–164. https://doi.org/https://doi.org/10.1016/j.actamat.2015.11.044

Reed-Hill, R. E., Abbaschian, R., & Abbaschian, R. (1973). *Physical metallurgy principles* (Vol. 17). Van Nostrand New York.

Ren, J., Li, C., Tu, X., & Shao, Z. (2022). Microstructure of Ultrafine Acicular Bainite and Mechanical Properties of 3Cr2MnNiMo Mold Steel during Austempering. *steel research international*, *93*(9), 2200151. https://doi.org/https://doi.org/10.1002/srin.202200151

Ruiz-Jimenez, Victor Kuntz, Matthias Sourmail, Thomas Caballero, G., F., Jimenez, J. A., & Carlos, G.-M. (2020). Retained Austenite Destabilization during Tempering of Low-Temperature Bainite. *Applied Sciences*, *10*(24), 1–20.

Saha Podder, A., & Bhadeshia, H. K. D. H. (2010). Thermal stability of austenite retained in bainitic steels. *Materials Science and Engineering: A*, *527*(7), 2121–2128. https://doi.org/https://doi.org/10.1016/j.msea.2009.11.063

Schneider, C. A., Rasband, W. S., & Eliceiri, K. W. (2012). NIH Image to ImageJ: 25 years of image analysis. *Nature Methods*, *9*(7), 671–675. https://doi.org/10.1038/nmeth.2089

Singh, R. (2011). *Applied welding engineering : processes, codes, and standards* (1st ed.). Elsevier/Butterworth-Heinemann.

Skowronek, A., Cordova-Tapia, E., Tobajas-Balsera, P., Garcia-Mateo, C., Jiménez, J. A., Petrov, R., & Grajcar, A. (2022). Bainite plate thickness reduction and microstructure tailoring by double austempering of Al-rich 3Mn steel. *Materials Science and Engineering: A*, *853*, 143743. https://doi.org/https://doi.org/10.1016/j.msea.2022.143743

Smallman, R. E., & Ngan, A. H. W. (2011). In *Physical Metallurgy and Advanced Materials (7th Edition)*. Elsevier.

Sourmail, T., Otter, L., Collin, S., Billet, M., Philippot, A., Cristofari, F., & Secordel, P. (2021). Direct and indirect decomposition of retained austenite in continuously cooled bainitic steels: Influence of vanadium. *Materials Characterization*, *173*, 1–10.

Souza, S., Moreira, P., & Faria, G. (2020). Austenitizing Temperature and Cooling Rate Effects on the Martensitic Transformation in a Microalloyed-Steel. *Materials Research*, *23*. https://doi.org/10.1590/1980-5373-mr-2019-0570

Ståhlkrantz, A., Hedström, P., Sarius, N., Sundberg, H.-Å., Kahl, S., Thuvander, M., & Borgenstam, A. (2020). Effect of Tempering on the Bainitic Microstructure Evolution Correlated with the Hardness in a Low-Alloy Medium-Carbon Steel. *Metallurgical and Materials Transactions A*, *51*(12), 6470–6481. https://doi.org/10.1007/s11661-020-06030-6

Su, Y., Yang, S., Yu, X. F., Zhou, C. B., Liu, Y. B., Feng, X. C., Zhao, Q., & Wu, J. D. (2022). Effect of Austempering Temperature on Microstructure and Mechanical Properties of M50 Bearing Steel. *Journal of Materials Research and Technology*, *20*, 4576–4584. https://doi.org/https://doi.org/10.1016/j.jmrt.2022.09.002

Sun, J., Wang, Y., Guo, S., & Liu, Y. (2020). Effect of prior austenite grain size on isothermal bainite transformation in 65Cr steel. *Materials Letters*, *266*, 127495. https://doi.org/https://doi.org/10.1016/j.matlet.2020.127495

Talebi, S. H., Ghasemi-Nanesa, H., Jahazi, M., & Melkonyan, H. (2017). In Situ Study of Phase Transformations during Non-Isothermal Tempering of Bainitic and Martensitic Microstructures. *Metals*, *7*(9), 346.

Talebi, S. H., Jahazi, M., & Melkonyan, H. (2018). Retained Austenite Decomposition and Carbide Precipitation during Isothermal Tempering of a Medium-Carbon Low-Alloy Bainitic Steel. *Materials*, *11*(8), 1441.

Taneike, M., Sawada, K., & Abe, F. (2004). Effect of carbon concentration on precipitation behavior of M23C6 carbides and MX carbonitrides in martensitic 9Cr steel during heat treatment. *Metallurgical and Materials Transactions A*, *35*(4), 1255–1262. https://doi.org/10.1007/s11661-004-0299-x

Taylor, M. D., Choi, K. S., Sun, X., Matlock, D. K., Packard, C. E., Xu, L., & Barlat, F. (2014). Correlations between nanoindentation hardness and macroscopic mechanical properties in DP980 steels. *Materials Science and Engineering: A*, *597*, 431–439. https://doi.org/https://doi.org/10.1016/j.msea.2013.12.084

Thomas, B. G. (2009). Modeling of Hot Tearing and Other Defects in Casting Processes. In D. U. Furrer & S. L. Semiatin (Eds.), *Fundamentals of Modeling for Metals Processing* (Vol. 22A, pp. 0). ASM International. https://doi.org/10.31399/asm.hb.v22a.a0005420

Tian, J., Xu, G., Zhou, M., & Hu, H. (2018). Refined Bainite Microstructure and Mechanical Properties of a High-Strength Low-Carbon Bainitic Steel Treated by Austempering

Below and Above MS. *steel research international*, *89*(4), 1700469. https://doi.org/https://doi.org/10.1002/srin.201700469

Tolouei, E., Hurel, V., Loucif, A., Morin, J.-B., & Jahazi, M. (2024). Influence of the as quenched state and tempering temperature on the final microstructure and hardness of a high strength medium carbon steel. *Materials Chemistry and Physics*, *325*, 1–13. https://doi.org/https://doi.org/10.1016/j.matchemphys.2024.129765

Tolouei, E., Hurel, V., Loucif, A., Morin, J.-B., & Jahazi, M. (2025). Influence of the As-quenched State and Tempering Heating Rate on Microstructural Characteristics of a High-Strength Steel. *Metallurgical and Materials Transactions A*. https://doi.org/10.1007/s11661-025-07778-5

Tolouei, E., Saadati, M., Morin, J.-B., Garcia-Mateo, C., & Jahazi, M. (2025). Influence of bainitic transformation temperature on microstructure evolution during isothermal holding and subsequent cooling. *Materials Chemistry and Physics*, *345*, 131248. https://doi.org/https://doi.org/10.1016/j.matchemphys.2025.131248

Ueji, R., Kimura, Y., Ushioda, K., Ohmura, T., & Inoue, T. (2021). Bainite Transformation and Resultant Tensile Properties of 0.6%C Low Alloyed Steels with Different Prior Austenite Grain Sizes. *ISIJ International*, *61*(2), 582–590. https://doi.org/10.2355/isijinternational.ISIJINT-2020-389

van Bohemen, S. M. C., & Morsdorf, L. (2017). Predicting the Ms temperature of steels with a thermodynamic based model including the effect of the prior austenite grain size. *Acta Materialia*, *125*, 401–415. https://doi.org/https://doi.org/10.1016/j.actamat.2016.12.029

Vander Voort, G. F. (1999). *Metallography, principles and practice*. ASM international.

Verdeja González, J. I., Fernández-González, D., & Verdeja, L. F. (2023). *Physical metallurgy and heat treatment of steel*. Springer. https://doi.org/10.1007/978-3-031-05702-1

Wang, B., Zhang, H.-L., Xu, B., Jiang, H.-Y., Sun, M.-Y., & Li, D.-Z. (2023). Sensitivity of the Impact Toughness and Microstructure of 15CrNi3MoV Steel Under Different Quenching Rates. *Acta Metallurgica Sinica (English Letters)*, *36*(10), 1735–1748. https://doi.org/10.1007/s40195-023-01583-y

Wang, E., He, Q., Gu, C., Wang, Y., Chen, H., Che, Y., Misra, R. D. K., Gong, N., Wu, H., & Niu, G. (2023). Effect of austempering temperature on microstructure evolution, mechanical properties and wear resistance of carbon-free nano-bainite steel. *Journal of Materials Research and Technology*, *26*, 6703–6718. https://doi.org/https://doi.org/10.1016/j.jmrt.2023.09.059

Wang, X., Liu, C., Qin, Y., Li, Y., Yang, Z., Long, X., Wang, M., & Zhang, F. (2022). Effect of tempering temperature on microstructure and mechanical properties of

nanostructured bainitic steel. *Materials Science and Engineering: A*, *832*, 142357. https://doi.org/https://doi.org/10.1016/j.msea.2021.142357

Wang, X., Xu, Y., Gao, Y., Wang, Y., & Misra, R. D. K. (2023). Enhancing strength-ductility combination in a novel Cu–Ni bearing Q&P steel by tailoring the characteristics of fresh martensite. *Journal of Materials Research and Technology*, *24*, 9015–9029. https://doi.org/https://doi.org/10.1016/j.jmrt.2023.05.153

Watanabe, M., Miyamoto, G., Zhang, Y., Morooka, S., Harjo, S., Kobayashi, Y., & Furuhara, T. (2024). Thermal Stability of Retained Austenite with Heterogeneous Composition and Size in Austempered Fe-2Mn-1.5Si-0.4C Alloy. *ISIJ International*, *64*(9), 1464–1476. https://doi.org/10.2355/isijinternational.ISIJINT-2024-044

Wu, B., Zhou, T., Wang, Z., Wang, X., Shang, C., Yu, Y., Elhefnawey, M., & Li, L. (2024). Effects of carbon concentration and transformation temperature on incomplete transformation and crystallography of low-carbon bainitic steel. *Journal of Materials Research and Technology*, *32*, 827–840. https://doi.org/https://doi.org/10.1016/j.jmrt.2024.07.186

Wu, R., Li, J., Su, Y., Liu, S., & Yu, Z. (2017). Improved uniformity of hardness by continuous low temperature bainitic transformation in prehardened mold steel with large section. *Materials Science and Engineering: A*, *706*, 15–21. https://doi.org/https://doi.org/10.1016/j.msea.2017.08.104

Xie, Y., Cheng, X., Wei, J., & Luo, R. (2022). Characterization of Carbide Precipitation during Tempering for Quenched Dievar Steel. *Materials*, *15*(18), 6448.

Yamamoto, S., Yokoyama, H., Yamada, K., & Niikura, M. (1995). Effects of the Austenite Grain Size and Deformation in the Unrecrystallized Austenite Region on Bainite Transformation Behavior and Microstructure. *ISIJ International*, *35*(8), 1020–1026. https://doi.org/10.2355/isijinternational.35.1020

Yan, G., Han, L., Li, C., Luo, X., & Gu, J. (2017). Characteristic of retained austenite decomposition during tempering and its effect on impact toughness in SA508 Gr.3 steel. *Journal of Nuclear Materials*, *483*, 167–175. https://doi.org/https://doi.org/10.1016/j.jnucmat.2016.11.011

Yang, Z., Chu, C., Jiang, F., Qin, Y., Long, X., Wang, S., Chen, D., & Zhang, F. (2019). Accelerating nano-bainite transformation based on a new constructed microstructural predicting model. *Materials Science and Engineering: A*, *748*, 16–20. https://doi.org/https://doi.org/10.1016/j.msea.2019.01.061

Yao, C., Lan, H., Tao, Z., Misra, R. D. K., & Du, L. (2021). Enhanced Strength and Toughness of Low-Carbon Bainitic Steel by Refining Prior Austenite Grains and Austempering Below Ms. *steel research international*, *92*(11), 2100263. https://doi.org/https://doi.org/10.1002/srin.202100263

Young, R. A. (1993). *The rietveld method* (Vol. 5). International union of crystallography.

Zajac, S., Schwinn, V., & Tacke, K. H. (2005). Characterisation and Quantification of Complex Bainitic Microstructures in High and Ultra-High Strength Linepipe Steels. *Materials Science Forum*, *500-501*, 387–394. https://doi.org/10.4028/www.scientific.net/MSF.500-501.387

Zhang, Y., Zhang, X., Sheng, G., Li, C., Han, L., & Gu, J. (2021). Effect of ultra-fine martensite and retained austenite induced by slow quenching on the mechanical properties of 9Cr 1.5Mo1Co(FB2) steel. *Materials Characterization*, *181*, 111452. https://doi.org/https://doi.org/10.1016/j.matchar.2021.111452

Zhang, Z., Wu, X. C., Li, N., & Min, Y. A. (2015). Alloy optimisation of bainitic steel for large plastic mould. *Materials Science and Technology*, *31*(14), 1706–1714. https://doi.org/10.1179/1743284714Y.0000000744

Zhao, H., Wynne, B. P., & Palmiere, E. J. (2017). Effect of austenite grain size on the bainitic ferrite morphology and grain refinement of a pipeline steel after continuous cooling. *Materials Characterization*, *123*, 128–136. https://doi.org/https://doi.org/10.1016/j.matchar.2016.11.025

Zhao, J.-C., & Notis, M. R. (1995). Continuous cooling transformation kinetics versus isothermal transformation kinetics of steels: a phenomenological rationalization of experimental observations. *Materials Science and Engineering: R: Reports*, *15*(4), 135–207. https://doi.org/https://doi.org/10.1016/0927-796X(95)00183-2

Zhao, J., Lv, B., Zhang, F., Yang, Z., Qian, L., Chen, C., & Long, X. (2019). Effects of austempering temperature on bainitic microstructure and mechanical properties of a high-C high-Si steel. *Materials Science and Engineering: A*, *742*, 179–189. https://doi.org/https://doi.org/10.1016/j.msea.2018.11.004

Zheng, Y., Wang, F., Li, C., Lin, Y., & Cao, R. (2019). Effect of Martensite Structure and Carbide Precipitates on Mechanical Properties of Cr-Mo Alloy Steel with Different Cooling Rate. *High Temperature Materials and Processes*, *38*(2019), 113–124. https://doi.org/doi:10.1515/htmp-2018-0018

Zheng, Y. F., Wu, R. M., Li, X. C., & Wu, X. C. (2017). Continuous cooling transformation behaviour and bainite formation kinetics of new bainitic steel. *Materials Science and Technology*, *33*(4), 454–463. https://doi.org/10.1080/02670836.2016.1224608

Zhou, T., Babu, R. P., Hou, Z., Odqvist, J., & Hedström, P. (2020). Precipitation of multiple carbides in martensitic CrMoV steels - experimental analysis and exploration of alloying strategy through thermodynamic calculations. *Materialia*, *9*, 100630. https://doi.org/https://doi.org/10.1016/j.mtla.2020.100630

Zhu, K., Chen, H., Masse, J.-P., Bouaziz, O., & Gachet, G. (2013). The effect of prior ferrite formation on bainite and martensite transformation kinetics in advanced high-strength steels. *Acta Materialia*, *61*(16), 6025–6036. https://doi.org/https://doi.org/10.1016/j.actamat.2013.06.043